EPFL

Thèse n° 9582

Mode interference and UV-induced mode conversion in few-mode fibers

Présentée le 20 août 2020

à la Faculté des sciences et techniques de l'ingénieur
Programme doctoral en photonique

pour l'obtention du grade de Docteur ès Sciences

par

Soham BASU

Acceptée sur proposition du jury

Prof. C. Moser, président du jury
Dr H. G. Limberger, directeur de thèse
Prof. R. Kashyap , rapporteur
Prof. B. Schmauss, rapporteur
Prof. L. Thévenaz, rapporteur

École
polytechnique
fédérale
de Lausanne

2020

Abstract

The major objective of this thesis was to find hitherto unknown general and simple solutions for fabrication of broadband high-extinction mode converters using local perturbations. This objective was successfully reached by generating two experimental algorithms which are appropriate for different cases-

- For large coupling constant, a direct experimental algorithm to fabricate broadband high-extinction mode converter using a single phase-shifted grating, without the need to have the knowledge of how the writing of the grating with local perturbations affects the fiber properties.

- For small coupling constant, a method to measure the effect of local perturbations on the intermodal dispersion experienced by the two interacting modes, using separate measurements of changes in corresponding two-mode interference (TMI) under such perturbations. Once the modified intermodal dispersion is known, coupling constant can be explicitly fitted using the spectra, and thereafter the optimal placement of phase shifts to generate broadband spectra can be calculated in a direct way.

Experimental verification was provided for these solutions for the LP_{01}-LP_{02} mode pair. The key enabling method of the second solution was the ability to measure the phase shift between the modes introduced by each local perturbation, using changes in TMI spectra. A host of other parameters were also estimated using measurements of the shift in TMI spectra, namely

- TMI fringe shift was used for measuring effect of changes in temperature and strain on intermodal dispersion. For exposure of the fiber with a scanning laser spot of constant velocity, the change in intermodal dispersion due to such particular exposure was also measured using TMI fringes.

- With carefully controlled experiments, the group-velocity equalization (GVE) wavelength of the TMI fringes was measured to have linear dependency on temperature and strain. This dependency was used for straightforward sensing of temperature and strain, without suffering from any dependency on the fiber length like TMI fringes. Using the shift of GVE wavelength during exposure of the full fiber with a scanning laser spot, the change in core index was estimated with high resolution using a simple model. Such estimation also allowed measurement of small index

changes due to irradiation, which is not possible with fiber Bragg gratings (FBGs) due to imperceptible strength of FBGs for small index changes, and also due to the lower sensitivity of wavelength shift of FBG compared to GVE.

- Capability of differentiating strain and temperature by combining GVE and FBG resonance wavelengths in the same fiber was explored. The GVE wavelength had an approximately three times higher temperature sensitivity compared to FBG resonance at similar wavelengths. The strain sensitivity of GVE and FBG resonance wavelengths were of similar magnitude but of opposite sign. The temperature and strain sensitivities of GVE was explained using a simple model consisting of only material parameters.

New understanding of different modalities of few-mode fibers has been generated by finding simple mathematical models linking different parameters to the intermodal phase of the TMI, including a model linking the disparate fields of resonant mode conversion and non-resonant TMI. Such models have been verified with precision experiments. The thesis concluded with practical solutions to the important technical problem of broadband high-extinction mode conversion in few-mode fibers.

Contents

List of figures ix

List of tables xvii

1 Introduction 1
- 1.1 Summary of the chapters . . . 3

2 Mathematical background 7
- 2.1 Mathematical description of modes . . . 7
  - 2.1.1 Cylindrically symmetric waveguides . . . 9
  - 2.1.2 TE, TM and hybrid mode approximation . . . 10
  - 2.1.3 Weakly guiding approximation and LP modes . . . 12
  - 2.1.4 Finite element method . . . 15
  - 2.1.5 Scalar wave equation . . . 16
  - 2.1.6 Mode conversion theory . . . 18
  - 2.1.7 Simulation of discrete segment . . . 20
- 2.2 Conclusions . . . 22

3 Sample details, preparation and general experimental methods 23
- 3.1 Few-mode fiber . . . 23
- 3.2 Lasers . . . 26
- 3.3 Fiber-Bragg grating fabrication . . . 27
- 3.4 Mode converter fabrication using laser irradiation . . . 30
- 3.5 Selective coupling of LP_{01} mode . . . 31
- 3.6 Spectroscopy apparatus . . . 32

4 Determination of intermodal dispersion in a few-mode fiber 33
- 4.1 Mathematical description . . . 34
- 4.2 Identification of TMI modes . . . 35
- 4.3 Estimating higher order dispersion coefficients . . . 37
- 4.4 Determination of offset . . . 39
  - 4.4.1 Limitations . . . 41
- 4.5 Sensitivity of MC resonance wavelength with respect to pitch . . . 43
- 4.6 Sensitivity of MC resonance wavelength with respect to offset . . . 45

4.7 Conclusion 45

5 Effect of perturbations on two-mode interference **47**
5.1 Introduction 47
5.2 Effect of perturbation on fringes 48
5.2.1 Temperature response of TMI 51
5.2.2 Strain response of TMI 56
5.2.3 Scanning laser exposure response of TMI 59
5.3 Effect of perturbations on GVE 62
5.3.1 Effect of temperature on GVE wavelength 63
5.3.2 Effect of strain on GVE wavelength 64
5.3.3 Effect of laser exposure on GVE wavelength 65
5.4 Temperature and strain differentiation 68
5.4.1 Working principle 69
5.4.2 Experiment parameters 71
5.4.3 Measurements and analysis 71
5.5 Conclusion 74

6 Effect of irradiation of marks on intermodal dispersion **75**
6.1 Theory: Connection between intermodal dispersion and TMI 75
6.2 Experimental setup 77
6.2.1 Femtosecond laser setup with spherical lens 77
6.2.2 Excimer laser setup from Optec 80
6.3 Experimental results 81
6.3.1 Phase unwrapping from TMI and MC fabrication 81
6.3.2 Model verification using large duty cycle 87
6.3.3 Model verification using small duty cycle 89
6.3.4 MC fabrication using medium duty cycle 92
6.3.5 Summary of fabricated MCs 95
6.3.6 Summary of different estimates of $\delta\beta(\lambda)$ at a fixed wavelength . . 96
6.4 Conclusions 97

7 Broadband mode converters **99**
7.1 Introduction 99
7.2 Partial-core irradiation 100
7.2.1 Motivation 100
7.2.2 Simulation method 101
7.2.3 Simulation results 104
7.3 Phase-shifted MC 108
7.3.1 Modelling of phase-shifted MC 109
7.3.2 Experimental verification for phase-shifted grating with three segments 111
7.4 Broadband mode conversion with only two segments 117

7.4.1 Experimental verification for phase-shifted grating with two segments 117
7.5 Conclusions 119

8 Summary and conclusions **121**

9 Acknowledgement **123**

10 Glossary of terms **125**
10.1 List of symbols and operators 126
10.2 List of abbreviations 128

A Appendix **129**
A.1 Material constants 129

Bibliography **131**

Curriculum Vitae **143**

List of Figures

2.1 Two-dimensional refractive index profile for a step-index fiber. The colorbar represents refractive index at 1.55 μm wavelength 11

2.2 LP modes for the step-index fiber profile in figure 2.1. The size of the plot boxes are 10 μm × 10 μm. 14

2.3 $V-b$ diagram of step-index fiber, calculated for LP_{01}, LP_{11}, LP_{21} and LP_{02}, calculated using equation 2.13 for the range $V \in (0.6, 5.1)$. 14

2.4 Two-dimensional refractive index profile for an arbitrary index bump . . 15

2.5 Discrete segment model for simulating a periodic laser exposure, where Λ'_{MC} represents the mark length and Λ_M is defined as $\Lambda_M = \Lambda_{MC} - \Lambda'_M$. The duty cycle is given by $\frac{\Lambda'_M}{\Lambda_{MC}}$ 21

3.1 Diametric refractive index profile of the FMF, offset by the cladding index, as obtained from Interfiber Analysis LLC 23

3.2 Phase matching of an FBG: Matching of the difference in axial wavevectors of a forward ($\beta_1(\lambda)$) and backward propagating mode, ($-\beta_2(\lambda)$) 27

3.3 Phase mask side-illumination for fabricating FBG [1] 27

3.4 Illustration of an FBG represented by equation 3.3 , with $\Lambda_{FBG} = 0.5$ μm, Gaussian $\Delta n_{dc}(z) = 0.006\ e^{(\frac{z-600}{25})^2}$ with z in μm, $n_0(z) = 1.463$ and $v(z) = 0.85$. An FBG fabricated with this refractive index profile along the fiber axis would have resonance wavelengths 1.4690 μm, 0.7345 μm and 0.4897 μm for the first ($M = 1$), second ($M = 2$) and third order ($M = 3$) reflection peaks respectively 29

3.5 Phase matching of an MC: Matching of the difference in axial wavevector of two different co-propagating modes, $\beta_1(\lambda)$ and $\beta_2(\lambda)$ 30

3.6 Illustration of MC irradiation using a translation stage and shutter [2] . 31

3.7 Fiber loops for getting rid of higher order modes in MC samples 32

4.1 General schematic for exciting modes in a cleaved FMF (containing FBG) using scanning of a cleaved SMF with spectroscopic set up attached on the other end. In general, the strengths of the reflection peaks depend on the mode coupling at the beginning of the few-mode fiber, and therefore has more prominence when (1) an SMF with suitable mode field diameter is spliced, or (2) appropriate gap is put between the neighboring SMF and FMF ends such that diffracted output of the SMF couples into higher-order modes of the FMF 36

4.2 Bragg resonance peaks due to intramodal and intermodal coupling of LP modes from an FBG of pitch 530 nm written inside the FMF, when excited with the scheme in figure 4.1 using an SM1500 SMF. The wavelength of resonance between LP_x and LP_y mode is denominated by λ_{x-y}. The spectrum on top shows the reflection peaks through the SMF, when the end of the SMF was put in contact with the end of the particular FMF sample at a slight offset, such that maximum number of peaks were observed. The spectrum at bottom shows reflection peaks through the SMF when the offset was minimized. After splicing the SMF to the particular FMF sample, three reflection peaks similar to the no-offset condition were observed 37

4.3 Schematic of TMI sample. The SMF are SM1500, and spliced to FMF on both ends without offset 38

4.4 Phase unwrapping of TMI signal 38

4.5 Simulated effective indices for step-index fiber with radius 5.0 μm and 14 % GeO_2 concentration in the core (Solid curves). The dashed gray line represents $\frac{\lambda}{2\Lambda_{FBG}}$. The intersection of the dashed line with the solid curves give the values of the resonance wavelengths for an FBG of pitch $\Lambda_{FBG} = 530.15$ nm 41

4.6 Simulated difference in propagation constants of LP_{01} and LP_{02} modes for a step-index fiber of radius 5.0 μm and 14 % GeO_2 concentration in the core. According to the simulation, the exact value of $\delta\beta(1.5422\ \mu m) = 0.0508\ \mu m^{-1}$ 42

4.7 Effective index difference of LP_{01} and LP_{02} for the simulated step-index fiber in figure 4.5 43

4.8 The calculated sensitivity of LP_{01}-LP_{02} MC resonance wavelength with change in the MC pitch for the FMF, as a function of the resonance wavelength. $|\frac{d\lambda_{MC}}{d\Lambda_{MC}}| > 0.05$ in the whole wavelength range of 1.5 μm to 1.7 μm, and becomes bigger as the resonance wavelength gets closer to the GVE wavelength 44

5.1 Calculated $\gamma(\lambda)$ based on the estimate of $\delta\beta(\lambda)$ in chapter 4 50

5.2 (a) Cooldown setup and (b) temperature decay of the bath with time, measured from two different thermocouples; one placed at the center of FMF coils, another placed right next to the FMF by concentric coiling. The two thermocouples showed slightly different temperatures, and the thermocouple right next to the FMF was used to get the temperature experienced by the FMF 52
5.3 3D plot of measured spectral evolution of TMI with temperature, where the spectral intensity (a.u.) is represented by color 52
5.4 Measured relative wavelength shifts of spectral maxima in figure 5.3 with temperature, which indicate linear shift for each measured maxima wavelength 53
5.5 Extracted linear slopes of relative wavelength shift of the extrema. These represent the left-hand side of the equation 5.3, for temperature 54
5.6 Measured relative change of $\delta\beta(\lambda)$ with temperature (coinciding blue and red colored solid curves corresponding to 4^{th} and 5^{th} order 2-dimensional polynomial fitting of extracted phase with respect to wavelength), obtained using equation 5.4, exhibiting a strong change compared to the relative change in refractive index with temperature for fused silica (dashed gray curve) and 14 % GeO_2-doped silica (dashed green curve) in the wavelength range 1.5 μm-1.7 μm 54
5.7 Measured relative wavelength shift with temperature change for GVE, FBG, nearest fringe of TMI, MC and farthest fringe of TMI 55
5.8 Measured MC and FBG spectrum for the lowest temperature of the cooldown experiment 56
5.9 Strain setup for TMI samples 57
5.10 Measured TMI transmission intensity spectrum (a.u.) for a 325 ± 0.5 mm long few-mode fiber sample, for different applied strains 57
5.11 Measured relative wavelength shifts of spectral maxima in figure 5.10. The apparent nonlinearity of the curves with extreme slopes come from the technical difficulty in precise determination of the two maxima wavelengths close to the GVE wavelength, to which these particular curves correspond 58
5.12 Extracted linear slopes of relative wavelength shifts of extrema with applied strain. 58
5.13 Extracted relative shift of LP_{01}-LP_{02} intermodal dispersion with strain (blue curve), obtained using equation 5.5, indicating a strong change in the wavelength range 1.5 μm-1.7 μm compared to that obtained by simply using the strain-optic coefficient of fused silica (dashed gray curve)[3; 4; 5] 59
5.14 Measured TMI fringe shift with exposure for four scans with translation speed v =20 μms^{-1} over the whole length of the FMF in the TMI sample. The red lines delineate the start of a new scan 61
5.15 Timing diagram of figure 5.14 62

5.16 Change of intermodal dispersion with scanning laser spot, obtained using equation 5.6 on the extracted phase of the TMI in figure 5.14, for the first (3 s exposure per point on the FMF) and second scan (6 s total exposure per point on the FMF from 2 consecutive scans of the laser spot) 62
5.17 Measured temperature response of GVE wavelength 64
5.18 Measured strain response of GVE wavelength 65
5.19 Measured TMI spectrum for FMF length 37 mm. Due to small number of fringes, phase unwrapping using zero wavelengths like chapter 4 was unreliable. Therefore smoothing spline was fitted to the first frame with a smoothing factor=0.9999 as defined in Matlab curve fitting toolbox to obtain a smooth fit, on which the extrema could be detected with certainty and thereby the phase could be estimated by cosine fitting of the normalized TMI spectrum. For further frames, the fitted intensity envelope and phase for the previous frame was used as guess for directly fitting equation 4.2 66
5.20 Measured shift of GVE wavelength with laser exposure 67
5.21 Change of core index with exposure time, t_0=1 s 68
5.22 Measured reflection spectrum from an FBG written in the FMF, at 22.9 °C and 55.0 °C 72
5.23 Measured temperature and strain dependence of λ_e and λ_{FBG}, with corresponding linear fits 73

6.1 Schematic of mark irradiation with fs laser for MC and TMI. Z is the fiber axis. The figure on the left shows the view from the X direction, while the one on the right shows the view from the Z direction 78
6.2 The monochrome image shows a far field fringe behind the FMF after focusing the femtosecond laser spot. The green inset on top shows a line scan of the fringe along the red line, which is placed along the horizontal axis of symmetry of the fringe. The fiber is aligned using the buttons of GUI on the bottom right, till the line scan of the fringe becomes symmetric, as is presented in the inset line scan (green box on top right) 79
6.3 Axial alignment at Z=-27.5 mm. The black arrow points the reference dot drawn on the camera screen 80
6.4 Schematic of mark irradiation with Optec LSV3 excimer laser for MC and TMI. The figure on the left shows the view from the X direction, while the one on the right shows the view from the Z direction 81
6.5 FMF viewed at the focus of the imaging and beam-delivery objective of the Optec LSV3 Excimer setup, showing cross-arrows for the center of the focus. The white lines showing coordinates has been added laser for showing the actual coordinates aligned with fiber axis 81

6.6 3D plot of measured evolution of TMI spectrum with mark number N. The pitch was chosen to be 105 μm such that no mode conversion happens between LP_{01} to higher order LP modes within the measured range of wavelength. At each wavelength, phase was added linearly per mark. The mark length was 95 μm. Colorbar shows transmission in arbitrary units. The fringes appear smudged around 1.52 μm after writing sufficient number of marks, which is due to the appearance of a cladding mode . . 83
6.7 Estimated average phase added per mark (Equation 6.4), showing convergence after writing sufficient number of marks 83
6.8 In a measurement *without* mode conversion, comparison between different degrees of fitting polynomial for the average phase added per mark estimated using equation 6.4. once is has stabilized for 200 marks. The results for different fitting degrees are overlapping, deeming this measurement suitable for making estimations 84
6.9 In a measurement *with* mode conversion, comparison between different degrees of fitting polynomial for the average phase added per mark, once the estimate using equation 6.4 has stabilized after writing 200 marks. The inconsistency between different fitting degrees deems this measurement unsuitable for making estimations 85
6.10 Example of MC fabrication with stable resonance wavelength. 86
6.11 Measured evolution of LP_{01} transmission intensity at λ_{MC} (red curve) and far away from λ_{MC} (blue curve), from the spectra presented in figure 6.10a. The lack of noticeable decay in transmission at the far wavelength showed that the particular irradiation condition induced low loss 87
6.12 Spectra of the MCs in figure 6.14 for two different exposure conditions (table 6.1), during the maximum conversion for each individual MC . . . 88
6.13 Estimates of extra phase added per mark from 200 marks, using equation 6.4, for total exposure times 5 s (blue curve) and 10 s (red curve) per mark. Exposure conditions are detailed in table 6.1 88
6.14 For the case of large duty cycle, the experimental comparison of fabricated MCs for two irradiation conditions with the predicted intermodal dispersion from equation 6.2. Exposure conditions are detailed in table 6.1 89
6.15 Spectra of two MCs with same exposure conditions and mark size of 25 μm, but different pitch (Exposure details in table 6.1) 90
6.16 For small duty cycle, estimates of extra phase added per mark from 200 marks, using equation 6.4, for total exposure times 5 s (blue curve). Exposure conditions are detailed in table 6.1 90
6.17 For small duty cycle, the experimental comparison of fabricated MCs with same irradiation conditions but for two different pitches, with the predicted intermodal dispersion (Equation 6.2). The predicted resonance wavelength is only off by 3 nm even while being close to the GVE wavelength. Exposure conditions are detailed in table 6.1 91

6.18 Evolution of measured LP_{01} transmission spectrum while writing resonant marks with 0.51 duty cycle for the LP_{01}-LP_{02} mode pair. The normalized transmission intensity is represented by color. The resonance wavelength was stable within ± 1 nm, implying stability of the alignment and laser parameters. A core-cladding mode resonance [6] was visible at $\lambda \approx 1.49$ μm, which was carefully separated from the LP_{01}-LP_{02} resonance peak by choosing the appropriate combination of pitch, intensity and fluence, through iterations 92

6.19 Comparison of measured strongest conversion spectra of two MCs fabricated using the Optec Excimer setup, with same irradiation condition and pitch. Fabrication 1 (blue curve) corresponds to the spectra in figure 6.18. The 20 dB bandwidths are 7 nm and 8 nm for fabrication 1 and 2 respectively. Exposure conditions are detailed in table 6.1 93

6.20 Average phase added per mark between LP_{01} and LP_{02} during mark writing with the Optec Excimer laser, as extracted from experimental data. Exposure conditions are detailed in table 6.1 94

6.21 Applying equation 6.2 to the estimated $\Delta\phi(\lambda, I, F)$, shape of $\delta\beta(\lambda)$ from chapter 4, and measured $\delta\beta_{MC}(1.56\ \mu m)$ from an MC made with 0.51 duty cycle (table 6.1), the value of $\delta\beta(1.56\ \mu m)$ was estimated, thereby estimating $\delta\beta(\lambda)$ along with offset. The interpolated value $\delta\beta(\lambda = 1.5422\ \mu m)$ is compared with the estimates from other methods in table 6.2 95

7.1 Free-space phase plates for increasing the coupling from LP_{01} to higher order $LP_{m,l}$ modes in a four-mode fiber 100

7.2 Schematic for writing $0-\pi$ phase segment inside a few-mode fiber using laser irradiation 101

7.3 Core-cladding refractive index difference for different GeO_2 doping represented by lines of different colors. These calculations were done using Sellmeier coefficients for SiO_2 and GeO_2 (table 3.1) and equation 3.1 . . 102

7.4 Simplified model for simulation of in-fiber phase segment, consisting of two semi-circular regions (D1 and D2) in the cross-section of the core with different refractive indices. The colorbar represents refractive indices at 1.55 μm wavelength 103

7.5 Simulated LP mode profiles for a 1.5 GeO_2 doping ratio between the two halves of the core. The GeO_2 concentration was 13.7 % in the lower half of the cross-section of the fiber core (D2 in figure 7.4). These simulations were performed using finite element method, with the help of PDETool package in Matlab 104

7.6 Simulated intermodal dispersion for different mode pairs of homogeneous semicircular phase segment waveguides, plotted as a function of GeO_2 doping ratio between the two halves of the core. The dotted black line in the top left panel represents the shift of GVE wavelength with varying GeO_2 doping ratio 105
7.7 Simulated $\delta\beta_{MC}(\lambda) = \delta\beta_{MC}(\lambda) + f\Delta\delta\beta_{MC}(\lambda)$, for different mode pairs for a duty cycle $f = 0.5$, and 1.5 GeO_2 doping ratio between the two halves of the core 106
7.8 Simulated overlap integrals of LP_{01} of pristine fiber to $LP_{m,l}$ modes of the irradiated segment (denoted by *) as function of GeO_2 doping ratio between the two halves of the core 107
7.9 Simulated transmission of LP_{01} at 1.55 μm wavelength during writing of marks with 0.5 duty cycle, pitch $\Lambda_{MC} = \frac{2\pi}{0.02645}$ μm, corresponding to the irradiation conditions of figure 7.7. Similar high loss is simulated in the whole wavelength range of 1.46 μm-1.62 μm 108
7.10 Schematic of phase shifted gratings with three segments 109
7.11 Schematic of phase shifted gratings with two segments 109
7.12 Evolution of LP_{01} transmission intensity spectrum during writing of periodic marks at the first segment 112
7.13 Evolution of LP_{01} transmission intensity at 1.56 μm during writing of periodic marks at the first segment 113
7.14 Measured normalized LP_{01} transmission intensity spectrum after writing 118 marks, with a gap of 58.6 μm after 49 marks (first segment) 114
7.15 Measured normalized LP_{01} transmission spectrum after writing 337 marks, with gaps of 58.6 μm introduced after 49 and 118 marks in the previous segments 114
7.16 Misalignment of translation stage during displacement 115
7.17 Simulated spectrum of broadband MC, in absence of translation stage misalignment 116
7.18 Measured spectrum of broadband MC, fabricated with compensation of translation stage misalignment 116
7.19 Measured evolution of the normalized LP_{01} transmission spectra with writing of marks without any phase shift, for segment 2 which contains standard periodic marks. The maximum achievable extinction ratio was 20 dB at 76 marks, after which the depth of the spectrum started to revert with writing of more marks due to overcoupling of the grating. 118
7.20 Measured evolution of the normalized LP_{01} transmission spectra after adding segment 1, containing 37 extra marks separated with a phase shift of π at 1.55 μm, *before* segment 2. Further marks were written on the other side of segment 2 without any extra phase gap, and the spectra were recorded 119

List of Tables

2.1 Mode classification of cylindrically symmetric waveguides 10

2.2 Link between the LP and vector modes for first four LP modes in a step-index fiber 13

3.1 Sellmeier coefficients of fused SiO_2 [7] and GeO_2 [8] 24

3.2 Specific wavelengths corresponding to the measurement setups and the step-index modeling of the few-mode fiber, together with the corresponding V-number, core refractive index and cladding refractive index 25

3.3 Lasers used during the thesis. Values indicated with * are measured, while the others are specified by the corresponding manufacturing companies. The Coherent excimer laser had rectangular beam shape, whereas the other lasers had elliptical beam shape. ** For the commercial Optec Excimer laser setup, the beam diameter was not available, whereas only the spot size was measured from fluorescence of the fiber core as seen under a microscope. Average power for a periodically sequenced pulses is defined over the sequence period, which was the quantity measured by power meters 26

4.1 Higher order LP_{01}-LP_{02} intermodal dispersion coefficients from TMI phase unwrapping of FMF with length 869±0.5 mm, with unknown offset . . . 39

4.2 Effective index estimates of LP_{01} and LP_{02} modes, at the intermodal resonance wavelength of an FBG with pitch 530 nm. The nomenclature $\lambda_{FBG,x}$ corresponds to equations 4.4-4.5 and the nomenclature λ_{x-y} corresponds to figure 4.2 40

6.1 List of fabricated MCs with corresponding parameters. $\Delta\phi$ represents the value of $\Delta\phi(\lambda, I, F)$ at the resonance wavelength. Table 3.3 lists the properties of the lasers 96

6.2 Comparison of $\delta\beta(\lambda)$ estimates for the pristine fiber at $\overline{\lambda} = 1.5422$ μm using different measurement conditions and methods. The estimate for duty cycle ≈ 0.22 (highlighted in orange) was chosen as the best candidate, since it predicted resonance wavelength accurately even in close vicinity of the GVE wavelength (Figure 6.17). I_{peak} refers to peak intensity of the laser. Fluence is the product of average intensity and exposure time. Table 3.3 lists the properties of the lasers 97

A.1 Material constants for fused silica and 14 % GeO_2-doped silica 129

1 Introduction

Optical fibers are the key component of the internet revolution. Other than the ubiquity of optical fibers, the scientific impact is evident form the 2009 Physics Nobel prize of Charles Kuen Kao,"for ground breaking achievements concerning the transmission of light in fibers for optical communication." [9; 10]. An optical fiber is effectively a cylindrical waveguide. The most common embodiment is a glass cylinder which is uniform along an axis, along with a different doping material (e.g. germanium) or structures (air holes) at and around the central region across the axis [11], called "core". In absence of nonlinear interactions, Maxwell's equations can be solved to obtain solutions of finite energy along the transverse plane, which are described as a travelling wave along the fiber axis and as a standing wave transverse to the axis. Such solutions are called "modes" of the fiber. The speciality of the modes is that the mode shape and size do not change over propagation, thus obtaining diffraction free transmission which is theoretically impossible with unguided optical wavefronts (unguided diffraction free beams should have infinite energy [12; 13], which is physically impossible). Due to lack of diffraction (change of beam shape during propagation due to loss of spatial frequencies), the modes of an ideal lossless waveguide should maintain its power over any distance. However there are multiple sources of loss from material effects, for example absorption losses, scattering losses (Scattering from Rayleigh, Raman, Brillouin effects, phonon, defects etc) and nonlinear losses. Breakthroughs of Charles Kao made silica fibers have low absorption loss in the mid-infrared wavelength range, almost to the low level of the fundamental limit of Rayleigh scattering. This made possible long-haul fiber optic communication in the so-called telecommunication wavelengths. It is now common to transmit pulsed light signals for typically 80 km without any amplification through optical fibers.

Multiple data channels can be created in the same single mode fiber in the temporal domain, by combination of non-overlapping modulated ultrashort pulse trains. This is known as time division multiplexing (TDM). The standard optical fiber communication is based on wavelength division multiplexing (WDM) and polarization division multiplexing (PDM) in fibers with a single mode at any of the used wavelengths. Closely placed

sharp wavelength lines can be chosen as channels in the available wavelength range of the amplification modules. Using WDM, any one of these distinct wavelength lines are individually added or taken out using add-drop multiplexers, which consist of couplers/isolators and filters of small bandwidth (generally thin-film filters, arrayed waveguide gratings etc). The spacing of these wavelength lines is limited by the wavelength broadening of the pulses during propagation through the fiber as well as the bandwidth of the add-drop filter. For the most common erbium-doped fiber amplifier (EDFA) modules operating in the $1535-1560$ nm wavelength range, typically 50 distinct wavelengths are used, along with two polarization channels for each wavelength. The total number of communication channels is thus typically $2*50=100$. Polarization resolved detection is used to differentiate the polarization modes [14]. This is called polarization division multiplexing (PDM).

Due to the boom of the internet, explosive demand of information channels has almost saturated the capacity of the long-haul communication networks [15]. Using multiple spatial modes for the same wavelength as independent information channels is one sought-after upgrade in the channel capacity of the upcoming fiber installations [16]. This technology is called mode division multiplexing (MDM) [17; 18; 19; 20; 21; 22; 23]. The technology used to differentiate the spatial modes is called multi-input-multi-output (MIMO) processing [24; 25], which is based on encoding. MDM is still ridden with many technological questions. For example, for both equal amplification and adding/dropping of such modes at a fixed wavelength, a promising solution is to have a device fabricated *inside* the fiber, which is capable of converting power from one chosen mode to another and vice-versa. Although such mode converters (MC) can be made using a variety of techniques, physically based on periodic perturbations along the fiber axis (grating) causing mixing of modes [2], the bandwidth of such a conversion is very narrow, far from the bandwidth of the EDFA based communication window [26; 27]. The capability of exchanging powers between modes at desired locations in the fiber also enables the usage of a host of waveguide and material effects. For example, higher order modes in a fiber can be used to compress pulses which have been temporally broadened after some propagation in the fundamental mode [28; 29]. In certain conditions MCs are also highly affected by environmental parameters in deterministic ways, hence, making them suitable candidates for sensing applications [30].

There are multiple open problems regarding mode converters in few-mode fibers (FMF)-

- The very limited available technology for making high-extinction (>99 % conversion) broadband grating based mode converters works for specific wavelength ranges particular to the mode pair and fiber [31], or using chirped gratings [32] with demanding fabrication specifications.
- Even for grating based MCs of narrow bandwidth, the resonance (maximum conversion) wavelength is highly dependent on the way the fiber is being perturbed

during the MC fabrication [33; 34]. There is no technique to directly predict this dependence.

Although the theoretical possibility of increasing the bandwidth of mode converters by optimal placement of phase shifts is established [35], the unknown change of fiber properties during any perturbation to make mode converters makes direct fabrication of such devices very complicated and iterative for every new FMF. A direct and general experimental algorithm to deterministically fabricate broadband high-extinction mode converters in any FMF is coveted, as evident from multiple recent research attempting to develop similar capabilities using various methods [36; 37; 38; 39; 40; 41].

This thesis culminates to a novel experimental algorithm for optimal and deterministic placement of phase gaps in phase-shifted gratings for achieving broadband high-extinction mode conversion in an FMF. The key to this algorithm is an invented technique for estimating the change in the intermodal dispersion of an FMF due to perturbations, from measurements of non-resonant two-mode interference of corresponding modes. Knowledge of the coupling constant, and intermodal dispersion experienced by the modes while they exchange energy in the region of the mode converter, enables direct design of broadband high-extinction mode converters.

Two-mode interference (TMI), which is observed when two particular modes are selectively in- and out-coupled from an FMF, provides a wrapped estimate of the differential phase acquired by two modes after traversing through the FMF. Measurement capability of this intermodal phase enables the measurement of the effects of a plethora of global (e.g. temperature, strain, uniform irradiation, global bending) and local (e.g. local irradiation with laser spot, local heating, local bending) perturbations to the FMF. In addition to the novel application of two-mode interference in deterministic fabrication of mode converters at desired wavelengths and with desired bandwidths, various other manifestations of the TMI have been studied from the perspective of both scientific and technical questions during the course of this thesis.

1.1 Summary of the chapters

- **Chapter 2:** This review chapter presents mathematical description of modes from variational perspective, methods to solve the partial differential equation describing the modes under different approximations, and mathematical modeling of mode converters. Among semi-analytical solutions of optical fibers consisting of annular regions of constant refractive index, the prototypical case of step-index fiber is discussed in detail. Dispersion equations of TE and TM mode approximations are presented. Further approximation of LP modes with the same dispersion equation as TE mode is illustrated, which is used in the rest of the thesis. Finite element method for simulating modes in general 2-dimensional waveguides is briefly

mentioned. Without establishing the smoothness of the solutions, only existence of solutions of the scalar wave equation is shown for a broad class of 2-dimensional waveguides. These descriptions present the mathematical tools to model all the experiments conducted during this thesis.

- **Chapter 3:** The common experimental tools used in the thesis are presented, namely description of the few-mode fiber, description of used lasers and laser irradiation techniques for fabricating gratings, and selective excitation and out-coupling of LP_{01} mode among other modes in the few-mode fiber. As for grating fabrication, the used methods of Bragg grating fabrication using phase mask technique, and grating mode converter fabrication using point-by-point laser irradiation, are described. The used spectroscopic tools are also listed.

- **Chapter 4:** Description of a novel method to (a) identify LP_{01} and LP_{02} intramodal reflection peak and intermodal reflection peaks from a fiber Bragg grating (FBG) written in a 4-mode fiber, and (b) consequently estimate the offset of intermodal dispersion of LP_{01}-LP_{02} using the resonance wavelengths of the FBG, in addition to higher order intermodal dispersion terms estimated from TMI phase unwrapping. Presence of only LP_{01} and LP_{02} during centrosymmetric excitation confirms that only LP_{01}-LP_{02} two-mode interference is generated in that condition.

- **Chapter 5:** Description of a method to measure the effect of temperature, strain and laser exposure (for scanning laser spot with constant velocity) on LP_{01}-LP_{02} intermodal dispersion. Shift of LP_{01}-LP_{02} group-velocity equalization (GVE) wavelength for temperature, strain and scanning laser exposure is measured. Assuming small change in the shape of the transverse refractive index profile under the effect of these parameters, simple models are presented which explain the temperature and strain shift. For scanning laser exposure which causes small refractive index perturbation along the transverse axes such that the shape of the refractive index profile does not undergo significant change, the model gives accurate estimate of change in photosensitive core index. Using the independently measured temperature and strain sensitivities of the GVE wavelength and FBG resonance wavelength, temperature and strain differentiation capability of the combination of these are explored.

- **Chapter 6:** Description of a new method which connects resonant (mode conversion) and non-resonant (TMI) effects in a few-mode fiber. The extra phase change due to each mark written consistently with laser irradiation, which is added to the accumulated phase difference over the FMF between LP_{01} and LP_{02} modes, is measured using TMI. This information is used to predict the change in intermodal dispersion under periodic irradiation along the fiber axis. The prediction method is verified by making MCs with precisely controlled irradiation conditions.

- **Chapter 7:** Evaluation of different methods for making broadband MC. New ideas were evaluated by simulations: (a) irradiation of part of the core along the transverse

axes to increase the coupling constants of different mode pairs and (b) MCs with multiple phase shifts. Simulations indicated that for the first case, losses might be too high due to poor mode overlaps, while for the second, indeed broadband mode conversion with high extinction ratio is possible. However simulations show that this method is highly sensitive to the change of alignment and irradiation parameters.

- **Chapter 8:** Summary of the new measurements and methods conducted during the course of this thesis, in light of future technical applications.

2 Mathematical background

This chapter reviews the mathematical tools used in this thesis.The background theory of modes in cylindrical waveguides from the variational perspective [42; 43] is presented, which enables reformulation of the eigenvalue partial differential equation describing the modes into a numerically tractable finite element problem. Particular cases which allow semi-analytic mode solving are discussed. For fixed profile shapes the waveguiding equation can be normalized to be independent of the material parameter, the solution of which is known as the V-b diagram [44]. For step-index fibers the V-b diagram is fixed, which allows for simple solution of dispersion equation and mode profiles. In addition the modes are described well with LP-mode approximation when the core-cladding index contrast is small [45]. Conversion of power between the orthogonal modes due to mixing of modes under periodic perturbations is modeled using linear algebra. For understanding complex irradiation profiles, a simple model is used which consists of uniform irradiated segments along the fiber axis and arbitrary modified transverse profile which is consistent over the axial length of the segment [46]. Modes are solved in the modified transverse profile using finite element method, and mode propagation at the boundaries of the perturbed segments is defined by the power coupling between the modes of the unperturbed and perturbed segments via mode overlap.

2.1 Mathematical description of modes

Fibers are ideally described by cylindrical waveguides. Modes of ideally lossless waveguides are defined as lossless and diffractionless solutions to Maxwell's equations satisfying the material and boundary conditions of the fiber. In an optical fiber the modes are propagating waves along the z direction which can be represented by the general stationary form $\vec{A}(x,y,\lambda)e^{i(\omega t-\beta(\lambda)z)}$. In the transverse direction (x,y) the solutions of the electric/magnetic field $\vec{A}(x,y,\lambda)$ are standing waves, with finite energy solutions which are square integrable along the transverse $x-y$ plane and satisfying smoothness conditions for Maxwell's equations to be well defined. The existence proof for such solutions are

described in [47] and [48].

Electromagnetic fields without any source or sink for a particular (vacuum) wavelength λ are described by Maxwell's equations [49]:

$$\begin{aligned}
\nabla.\vec{E}(x,y,z,\lambda,t) &= 0 \\
\nabla\times\vec{E}(x,y,z,\lambda,t) &= -\mu(x,y,z,\lambda)\frac{\partial\vec{H}(x,y,z,\lambda,t)}{\partial t} \\
\nabla.\vec{H}(x,y,z,\lambda,t) &= 0 \\
\nabla\times\vec{H}(x,y,z,\lambda,t) &= \epsilon_0(\lambda)n^2(x,y,z,\lambda)\frac{\partial\vec{E}(x,y,z,\lambda,t)}{\partial t}
\end{aligned} \tag{2.1}$$

where $\vec{E}(x,y,z,\lambda,t)$ or $\vec{H}(x,y,z,\lambda,t)$ is the vector electric or magnetic field. For dielectric materials, $\mu(x,y,z,\lambda)=\mu_0$, which is the permeability of free space. $\epsilon_0(\lambda)$ is the permittivity of free space and $n(x,y,z,\lambda)$is the refractive index of the medium. For general waveguides, the structure and optical composition is given by $n(x,y,z,\lambda)$. In the particular case of an ideal unperturbed optical fiber with its axis aligned along z, the structure and optical composition is given by $n(x,y,\lambda)$. For such a structure, at fixed λ, the stationary form of equation 2.1 is given by the following set of equations:

$$\nabla_\beta\times(\nabla_\beta\times\vec{E}(x,y,\lambda)) = k_0^2n^2(x,y,\lambda)\vec{E}(x,y,\lambda) \tag{2.2}$$

$$\nabla_\beta.(n^2(x,y,\lambda)\vec{E}(x,y,\lambda)) = 0 \tag{2.3}$$

$$\nabla_\beta\times(n^{-2}\nabla_\beta\times\vec{H}(x,y,\lambda)) = k_0^2\vec{H}(x,y,\lambda) \tag{2.4}$$

$$\nabla_\beta.(\vec{H}(x,y,\lambda)) = 0 \tag{2.5}$$

where $k_0(\lambda)$ is the free-space wave-vector, and the operators $\nabla_\beta\times$ and $\nabla_\beta.$ operating on $\vec{A}(x,y,\lambda)=A_x(x,y,\lambda)\hat{x}+A_y(x,y,\lambda)\hat{y}+A_z(x,y,\lambda)\hat{z}$ are defined in the following way, $A_x(x,y,\lambda)$, $A_y(x,y,\lambda)$ and $A_z(x,y,\lambda)$ being scalar and $\hat{x},\hat{y},\hat{z}$ being unit vectors in x,y,z directions respectively:

$$\nabla_\beta\times\vec{A}=\begin{bmatrix}\frac{\partial A_z}{\partial y}+i\beta A_y\\ i\beta A_x+\frac{\partial A_z}{\partial x}\\ \frac{\partial A_y}{\partial x}-\frac{\partial A_x}{\partial y}\end{bmatrix} \qquad \nabla_\beta.\vec{A}=\frac{\partial A_x}{\partial x}+\frac{\partial A_y}{\partial y}-i\beta A_z \qquad k_0=\frac{2\pi}{\lambda} \tag{2.6}$$

If $n(x,y,\lambda)$ is discontinuous in the $x-y$ plane, $\vec{E}(x,y,\lambda)$ is not differentiable in $x-y$ plane, from equation 2.3. Thus it is easier to formulate the existence question of the eigenvalue problem in terms of $\vec{H}(x,y,\lambda)$, which is differentiable for any $n(x,y,\lambda)$ as long as the magnetic permeability is constant, if an eigenvalue exists. Instead of brute force method to find an eigenvalue, the problem can be reformulated in a variational form which is easier to handle. The eigenvalue problems 2.4 and 2.5 can be reformulated to the

question of existence of $\vec{H}(x,y,\lambda)$ which is square integrable in $x-y$ plane and smooth up to differentiation in x and y coordinates[48]. For fixed λ, given any $\vec{H'}(x,y,\lambda)$ in the field of square integrable functions with *weak* derivatives, $\vec{H}(x,y,\lambda)$ also belongs to this field and satisfies [48]:

$$\int_{\mathbb{R}^2}\left[\frac{1}{n^2}\nabla_\beta\times\vec{H}\ \overline{\nabla_\beta\times\vec{H'}}+\frac{1}{n_0^2}\nabla_\beta.\vec{H}\ \overline{\nabla_\beta.\vec{H'}}\right]dxdy = \quad k_0^2\int_{\mathbb{R}^2} n^2(x,y,\lambda)\vec{H}\overline{\vec{H'}}\ dxdy \tag{2.7}$$

where $n_0(\lambda)$ is the refractive index of the cladding. In [47] it is shown using complex analysis method of Riemann manifold that only finite number of real $\beta(\lambda)$ can satisfy equation 2.7 for any λ. For cylindrically symmetric waveguides consisting of uniform annular segments, the basis functions of the modes is known in each segment. The specific conditions to be satisfied at the boundaries of the annular segments are : (a) continuous $E_z(x,y,\lambda)$ or $H_z(x,y,\lambda)$, and (b) curl-free (in $x-y$ plane) $\vec{H}(x,y,\lambda)$. This provides a semi-analytic method to find eigenvalues.

2.1.1 Cylindrically symmetric waveguides

For cylindrically symmetric waveguides, the z component for both the electric and magnetic fields completely describe the possible solutions of equations 2.2- 2.5. Of particular importance is the fact that the method of separation of variables can be applied on both of these. Denoting a general expression $A_z(x,y,\lambda)$ for the z component of both the electric and magnetic fields, Helmhotz equations are derived for the modes:

$$\begin{aligned}&\Delta A_z(x,y,\lambda)+k^2(r,\lambda)A_z(x,y,\lambda)=\beta^2(\lambda)A_z(x,y,\lambda)\\ \implies&\Delta A_z(r,\theta,\lambda)+k^2(r,\lambda)A_z(r,\theta,\lambda)=\beta^2(\lambda)A_z(r,\theta,\lambda)\end{aligned} \tag{2.8}$$

where $r=\sqrt{x^2+y^2}$ and θ is the angle defined by (x,y) with the x-axis. Cylindrical symmetry further allows using the separation of variables $A_z(r,\theta,\lambda)=R(r)\Theta(\theta)$

$$\begin{aligned}&\Delta=\frac{\partial^2}{\partial r^2}+\frac{1}{r}\frac{\partial}{\partial r}+\frac{1}{r^2}\frac{\partial^2}{\partial\theta^2},\quad k^2(x,y,\lambda):=k_0^2(\lambda)\ n^2(r,\lambda)\\ \implies&\left[\frac{\partial^2}{\partial r^2}+\frac{1}{r}\frac{\partial}{\partial r}+\frac{1}{r^2}\frac{\partial^2}{\partial^2\theta}+k^2(r,\lambda)\right]A_z(r,\theta,\lambda)=\beta^2(\lambda)A_z(r,\theta,,\lambda)\\ \implies&\Theta(\theta,\lambda)\left[\frac{\partial^2}{\partial r^2}+\frac{1}{r}\frac{\partial}{\partial r}+k^2(r,\lambda)\right]R(r,\lambda)+R(r,\lambda)\frac{1}{r^2}\frac{\partial^2}{\partial\theta^2}\Theta(\theta,\lambda)=\beta^2(\lambda)R(r,\lambda)\Theta(\theta)\end{aligned} \tag{2.9}$$

Equation 2.9 can be separated into two eigenvalue problems

$$\frac{\partial^2}{\partial\theta^2}\Theta(\theta,\lambda)+m^2\Theta(\theta,\lambda)=0 \tag{2.10}$$

$$\left[\frac{\partial^2}{\partial r^2}+\frac{1}{r}\frac{\partial}{\partial r}+k^2(r,\lambda)-\frac{m^2}{r^2}\right]R(r,\lambda)=\beta^2R(r,\lambda) \tag{2.11}$$

Integer eigenvalues $m^2 \geq 0$ are taken for the differential equation 2.10 with respect to angle, since any other real eigenvalue m^2 gives a solution which do not have a period of 2π. Other than having a mathematical discontinuity in such cases, physically the electromagnetic field defined by such a solution will destructively interfere with itself due to random phases, thus inhibiting the existence of standing modes. The solution to the angular part are equations $cos(m\theta)$ and $sin(m\theta)$, for integer m, for any λ. Since it is known that the general eigenvalue problem in 2-dimension has finite solutions [47], the only point needed to be checked is if equation 2.11 has valid solutions for some discrete set of of $\lim_{r\to\infty} inf(k(r,\lambda)) \leq \beta(\lambda) \leq \lim_{r\to\infty} sup(k(r,\lambda))$. The function $k(r,\lambda)$ attains its extrema in r since it is bounded in value in a bounded domain of $x-y$ plane by the definition of a waveguide. Every mode also has two orthogonal local distributions of polarization. In this thesis, such polarization modes have been assumed to be degenerate.

2.1.2 TE, TM and hybrid mode approximation

For simplifying the mode solving using equation 2.10 and 2.11, the solution space can also be categorized by putting either $E_z(r,\lambda) = 0$ and $m = 0$ (TE modes), or $H_z(r,\lambda) = 0$ and $m = 0$ (TM modes), and the the rest of the possible conditions (hybrid modes). Table 2.1 lists the individual conditions to be satisfied for TE, TM or hybrid modes [50]:

Modes	Zero quantities	Continuous quantities
TE	$E_z(r,\lambda),\ E_r(r,\lambda),\ H_\theta(r,\lambda)$	$E_\theta(r,\lambda) = \frac{i\omega\mu_0}{k_0^2 n^2(r,\lambda) - \beta^2(\lambda)} \frac{\partial H_z(r,\lambda)}{\partial r}$ and $H_z(r,\lambda)$
TM	$E_\theta(r,\lambda),\ H_r(r,\lambda),\ H_z(r,\lambda)$	$E_z(r,\lambda)$ and $H_\theta(r,\lambda) = -\frac{i\omega\epsilon_0 n^2(r,\lambda)}{k_0^2 n^2(r,\lambda) - \beta^2(\lambda)} \frac{\partial E_z(r,\lambda)}{\partial r}$
Hybrid	–	$E_\theta(r,\lambda),\ H_\theta(r,\lambda),\ E_z(r,\lambda)$ and $H_z(r,\lambda)$

Table 2.1 – Mode classification of cylindrically symmetric waveguides

This formalism becomes especially convenient for fibers composed of annular layers of different compositions, since the solutions $R(r,\lambda)$ inside each annulus can be represented as a linear combination of Bessel functions and modified Bessel function, whereas for the outermost layer (Assumed to be infinite for mathematical convenience) $R(r,\lambda)$ is only represented by a modified Bessel function to have finite energy solutions. Matching these for linear combination of Bessel functions and modified Bessel functions with unknown coefficients at the boundaries give a set of simultaneous equations, which can be written as an associated matrix equation which equates to zero [51]. Since it is known from [47] that non-trivial solutions corresponding to finite number of real nonnegative eigenvalue(s) $\beta(\lambda)$ exist, the determinant of the associated matrix must be zero for such $\beta(\lambda)$. Thus finding real $\beta(\lambda)$ which make the associated matrix singular provides an algorithm to find the eigenvalues. This method can be illustrated with the simple example of prototypical

cylindrically symmetric step-index fiber, which can approximately model various real fiber samples. An illustration of the refractive index profile at 1.55 μm wavelength for a fused silica step-index fiber with core radius 5.0 μm and and 14 % GeO_2 concentration in the core is shown in figure 2.1.

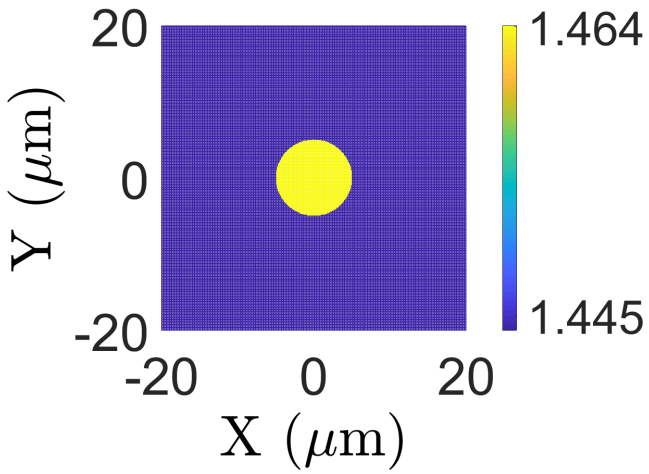

Figure 2.1 – Two-dimensional refractive index profile for a step-index fiber. The colorbar represents refractive index at 1.55 μm wavelength

The TE and TM modes equations for a step-index fiber can be normalized using unitless normalized frequency V and normalized propagation constant b:

$$\begin{aligned} &\textbf{V}\text{-number:} && V(\lambda) = \frac{2\pi a}{\lambda}\sqrt{n_1^2(\lambda) - n_0^2(\lambda)} = k_0(\lambda)\ a\sqrt{n_1^2(\lambda) - n_0^2(\lambda)} \\ &\textbf{b}\text{-number:} && b(\lambda) = \frac{n_e^2(\lambda) - n_0^2(\lambda)}{n_1^2(\lambda) - n_0^2(\lambda)} \end{aligned} \tag{2.12}$$

where the effective index $n_e(\lambda) = \frac{\lambda}{2\pi}\beta(\lambda)$, a is the radius of the core, and $n_0(\lambda)$ and $n_1(\lambda)$ are respectively the cladding and core refractive index at wavelength λ. Then equation 2.11 gets reduced to a waveguide-only equation free of any material parameters:

$$\begin{aligned} &\frac{\partial^2}{\partial r^2}R(r,\lambda) + \frac{1}{r}\frac{\partial}{\partial r}R(r,\lambda) - \frac{m^2}{r^2}R(r,\lambda) = \frac{1}{a^2}V^2(\lambda)b(\lambda)R(r,\lambda) && \forall r > a \\ &\frac{\partial^2}{\partial r^2}R(r,\lambda) + \frac{1}{r}\frac{\partial}{\partial r}R(r,\lambda) - \frac{m^2}{r^2}R(r,\lambda) = -\frac{1}{a^2}V^2(\lambda)\big(1 - b(\lambda)\big)R(r,\lambda) && \forall r \le a \end{aligned} \tag{2.13}$$

Matching the boundary conditions at $r = a$ then give the following dispersion equations

for the normalized parameters $u(n_1(\lambda), n_0(\lambda), a) = V\sqrt{1-b}$ and $w(n_1(\lambda), n_0(\lambda), a) = V\sqrt{b}$:

$$\frac{J_1(u)}{uJ_0(u)} = -\frac{K_1(w)}{wK_0(w)} \qquad \text{:TE mode} \qquad (2.14)$$

$$\frac{J_1(u)}{uJ_0(u)} = -\frac{n_0^2(\lambda)}{n_1^2(\lambda)}\frac{K_1(w)}{wK_0(w)} \qquad \text{:TM mode} \qquad (2.15)$$

$$\left[\frac{J'_m(u)}{uJ_m(u)} + \frac{K'_m(w)}{wK_m(w)}\right]\left[\frac{J'_m(u)}{uJ_m(u)} + \left(\frac{n_0(\lambda)}{n_1(\lambda)}\right)^2\frac{K'_m(w)}{wK_m(w)}\right] \qquad (2.16)$$

$$= m^2\left[\frac{1}{u^2} + \frac{1}{w^2}\right]\left[\frac{1}{u^2} + \left(\frac{n_0(\lambda)}{n_1(\lambda)}\right)^2\frac{1}{w^2}\right] \qquad \text{:Hybrid mode} \qquad (2.17)$$

where J_m and K_m are Bessel functions and modified Bessel functions, respectively. (The indices m and $\hat{m}$ have been used for the angular indices of hybrid modes and LP modes respectively, in contrast to usage of n and m in [44]. This is to avoid possible confusion between the azimuthal number for hybrid modes and transverse refractive index $n(x, y)$.) The plot of b as a function of V for TE modes of step-index fibers is independent of material parameters [44]. Given the waveguide parameters and the wavelength, this makes is simple to look up the solutions of eigenvalues of TE, TM and hybrid modes by referring to the $V - b$ diagram using 2.12. Solving the dispersion equation for b number for a certain V number which incorporates material parameters, geometry and wavelength, all parameters of the step-index fiber modes can be explicitly calculated.

2.1.3 Weakly guiding approximation and LP modes

For small index contrast, the factor $\left(\frac{n_0(\lambda)}{n_1(\lambda)}\right)^2$ can be ignored in the dispersion equation. For $m = 0$, TE and TM modes then have the same dispersion equation (equation 2.14). For $m > 0$, the solutions are categorized using the convention of HE and EH modes [50]:

$$\frac{J_{m+1}(u)}{uJ_m(u)} = -\frac{K_{m+1}(w)}{wK_m(w)} \qquad \text{:EH mode} \qquad (2.18)$$

$$\frac{J_{m-1}(u)}{uJ_m(u)} = \frac{K_{m-1}(w)}{wK_m(w)} \qquad \text{:HE mode} \qquad (2.19)$$

Under the approximation $\left(\frac{n_0(\lambda)}{n_1(\lambda)}\right)^2 \approx 1$, collecting the same dispersion equations of TE, TM, EH and HE modes to categorize the modes is called the LP mode approximation, which is the approximate model for the fiber used in this thesis [45]. The dispersion

equations are:

$$\frac{J_0(u)}{uJ_1(u)} = \frac{K_0(w)}{wK_1(w)} \qquad :\mathrm{LP}_{0l} \text{ mode, } \hat{m} = 0$$
$$\frac{J_{\hat{m}}(u)}{uJ_{\hat{m}-1}(u)} = -\frac{K_{\hat{m}}(w)}{wK_{\hat{m}-1}(w)} \qquad :\mathrm{LP}_{\hat{m}l} \text{ mode, } \hat{m} > 0 \tag{2.20}$$

where non-negative integer-valued $\hat{m}$ corresponds to different angular eigenvalues of TE, TM and hybrid modes

$$LP_{\hat{m}l} = \left\{ \begin{array}{ll} TE_{0l} \text{ or } TM_{0l} & \text{for } \hat{m} = 1 \\ EH_{\hat{m}-1\ l} & \text{for EH mode} \\ HE_{\hat{m}+1\ l} & \text{for HE mode} \end{array} \right\}$$

The vector modes corresponding to LP_{01}, LP_{11}, LP_{21} and LP_{02} modes are listed in table 2.2.

$\mathrm{LP}_{\hat{m}l}$ mode designation	l	Vector mode designation
LP_{01}, $\hat{m} = 0$	1	HE_{11}
LP_{11}, $\hat{m} = 1$	1	TE_{01} TM_{01} HE_{21}
LP_{21}, $\hat{m} = 2$	1	EH_{11} HE_{31}
LP_{02}, $\hat{m} = 0$	2	HE_{12}

Table 2.2 – Link between the LP and vector modes for first four LP modes in a step-index fiber

Figure 2.2 illustrates LP modes at 1.55 μm wavelength for the fiber profile in figure 2.1. The angular part can be represented by one of the two orthogonal solutions $cos(\hat{m}\theta)$ or $sin(\hat{m}\theta)$, which give the two degenerate modes for the same $\hat{m} \geq 0$ in cylindrically symmetric fibers.

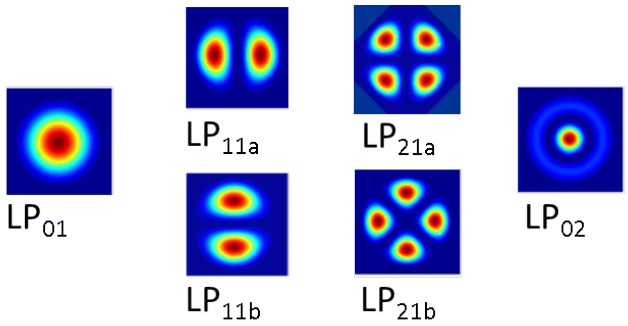

Figure 2.2 – LP modes for the step-index fiber profile in figure 2.1. The size of the plot boxes are 10 μm × 10 μm.

Figure 2.3 shows the $V-b$ diagram of a step-index fiber in the range $V \in (0.6, 5.1)$, obtained by numerically solving equation 2.13 for different values of V. Given the refractive indices of core and cladding at some wavelength, and core size, the effective index of a guided mode can be calculated by applying equation 2.12 on the corresponding b number.The b number can be obtained from interpolation from a library of $V-b$ values, or by solving the normalized equation 2.13 for the given V number. The cut-off V numbers of an LP mode in a step-index fiber, denominated as V_c, is such that the particular mode is not guided for smaller V numbers, and is given by $J_m(V_c) = 0$ [45]. The cut-off V for the first 5 supported modes with increasing V are $V_c(\mathrm{LP}_{01})$=0, $V_c(\mathrm{LP}_{11})$=2.405, $V_c(\mathrm{LP}_{21})$=$V_c(\mathrm{LP}_{02})$=3.832, $V_c(\mathrm{LP}_{31})$=5.136. Therefore in fibers where the $V(\lambda)$ is a decreasing function of wavelength, the fiber starts guiding a new LP mode when the wavelength is made smaller than the cut-off wavelength of that mode λ_c defined by $V(\lambda_c) = V_c$.

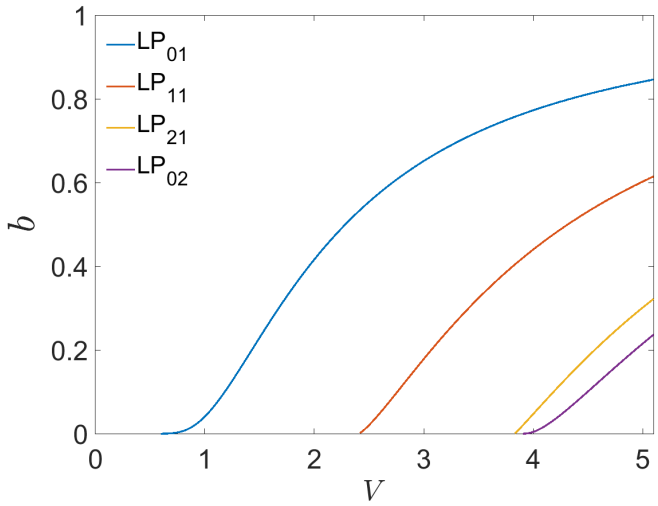

Figure 2.3 – $V-b$ diagram of step-index fiber, calculated for LP_{01}, LP_{11}, LP_{21} and LP_{02}, calculated using equation 2.13 for the range $V \in (0.6, 5.1)$.

2.1.4 Finite element method

For more complicated index profiles (Figure 2.4), it is almost always impossible to find an analytical solution to the set of equations 2.3, 2.2, 2.5 and 2.4. Fortunately methods from functional analysis can be used to establish the existence of *weak* solutions [52] to the equivalent variational problem 2.7. The weak solutions belong to the class of weakly differentiable square integrable functions in 2-dimension, referred as $W^{1,2}(\mathbb{R}^2)$ in the terminology of Sobolev space theory [52]: The eigenvalues are given by [48]:

$$\lambda_m(\beta) = sup_m\, inf_{H \in H_m^{\perp}} \frac{\int_{\mathbb{R}^2} \left[\frac{1}{n^2} \nabla_\beta \times \vec{H}\ \overline{\nabla_\beta \times \vec{H}} + \frac{1}{n^2_{Cladding}} \nabla_\beta . \vec{H}\ \overline{\nabla_\beta . \vec{H}} \right] dxdy}{\int_{\mathbb{R}^2} \vec{H}\ \overline{\vec{H}}\ dxdy} \tag{2.21}$$

where $H_1^{\perp} = W^{1,2}(\mathbb{R}^2)$, and $H_m^{\perp} := H \in W^{1,2}(\mathbb{R}^2) : (H, H^{(j)}) = 0\ \forall\, j = 1, ..., m-1$. The method of finite element [42; 43] consists of discretization of the physical space, then approximating the solution with the basis of piecewise polynomials in the discrete mesh. The minimization problem 2.21 then becomes equivalent to equating the partial derivatives of the functional in 2.21 to zero, with respect to the coefficients of the basis polynomials. This provides an associated matrix equation (generally very large) equating to zero whose eigenvectors are the coefficients of the solution basis. To have a non-trivial solutions at any particular λ, real $\beta(\lambda)$ are found which make the determinant of the associated matrix zero.

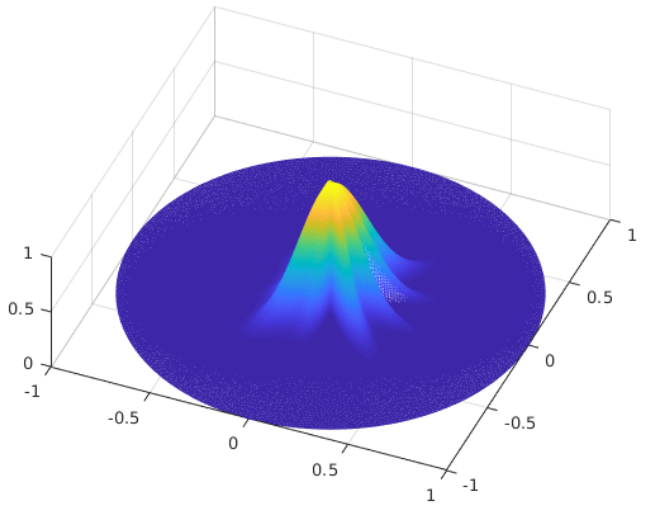

Figure 2.4 – Two-dimensional refractive index profile for an arbitrary index bump

2.1.5 Scalar wave equation

Although solutions to equation 2.21 give exact solutions to 2.3, 2.2, 2.5 and 2.4, for most practical applications solving the scalar wave equation for $E(x,y,\lambda)$ using finite element method and ignoring the boundary conditions is sufficient to approximately describe the solutions of equations 2.3, 2.2, 2.5 and 2.4 [53].

$$\Delta E(x,y,\lambda) + k_0^2 n^2(x,y,\lambda) E(x,y,\lambda) = \beta^2(\lambda) E(x,y,\lambda) \tag{2.22}$$

The variational formulation is especially simple with respect to finding the eigenvalue

$$\beta_m^2(\lambda) = sup_m inf_{\psi \in \psi_m^\perp} \frac{\int_{\mathbb{R}^2} -(|\nabla\psi(x,y,\lambda)|^2 + k_0^2 n^2(x,y,\lambda)|\psi(x,y,\lambda)|^2) dxdy}{\int_{\mathbb{R}^2} |\psi(x,y,\lambda)|^2 dxdy} \tag{2.23}$$

$$\implies \beta_m^2(\lambda) \leq \sup_{\mathbb{R}^2} \left(k_0^2(\lambda) n^2(x,y,\lambda) \right) \tag{2.24}$$

where $\psi_1^\perp = W^{1,2}(\mathbb{R}^2)$, and $\psi_m^\perp := \psi \in W^{1,2}(\mathbb{R}^2) : (\psi, \psi^{(j)}) = 0 \ \forall j = 1, ..., m-1$

As for the existence of such eigenvalues, if $n(x,y,\lambda)$ is bounded, the absolute value of possible eigenvalues are bounded above due to equation 2.24. This holds true for optical fibers with standard guiding. If there is even one $\psi_{min}(x,y,\lambda)$ such that the functional in 2.23 is positive, then the mathematical set consisting of the possible values of the functional is non-empty and bounded above. In that case, by the *least upper bound property* of real number sets, the functional has a supremum, or least upper bound. Under the weak sense of derivatives, the Sobolev space $W^{1,2}(\mathbb{R}^2)$ also turns out to be *complete*, implying that the limit of any sequence of functions also lies in $W^{1,2}(\mathbb{R}^2)$. Thus the minimizer(s) $\psi_{min}(x,y,\lambda)$ is(are) weakly differentiable square-integrable functions satisfying 2.22.

The only thing left to prove is that there exists some $\psi(x,y,\lambda)$ for which the functional in 2.23 is positive. This is easy for optical fibers due to two reasons [48]:

- Fibers with standard guiding mechanism have the structure that the average of the index bump is positive, implying $0 < \int_{\mathbb{R}^2} \left(n^2(x,y,\lambda) - n_0^2(\lambda) \right) dxdy = \int_{\Omega \subset \mathbb{R}^2} \left(n^2(x,y,\lambda) - n_0^2(\lambda) \right) dxdy < \infty$, where Ω is the domain where the value of the bump is different from the value of $n(\lambda)_0^2$. Since Ω is bounded, the average is always well-defined.

- Under the previous condition, for the special case of two-dimensions, a sequence of explicit trial functions $\psi_N(x,y,\lambda)$ can be created for natural number N such that

the functional in 2.23 can be made positive for sufficiently large N.

$$\psi_N(x,y,\lambda) = \begin{cases} 1 & if\ \sqrt{(x^2+y^2)} < N \\ \frac{ln(2N)-ln(\sqrt{(x^2+y^2)})}{ln(N)}, dx & if\ N < \sqrt{(x^2+y^2)} < 2N \\ 0 & if\ 2N < \sqrt{(x^2+y^2)} \end{cases} \tag{2.25}$$

where $ln(x)$ is the natural logarithm of x. For any N, $\lim_{\sqrt{x^2+y^2}\to\infty} \psi_N(x,y,\lambda) = 0$, implying square-integrability. For the particular choice of trial functions in equation 2.25, the integral in $x-y$ plane for both $|\psi_N(x,y,\lambda)|^2$ and $|\nabla\psi_N(x,y,\lambda)|^2$ are explicit functions of N. From these, explicit bounds for parts of the the functional in 2.23 can be obtained as functions of N:

$$\int_{\mathbb{R}^2} |\psi_N(x,y,\lambda)|^2 dxdy = 2\pi \int_{\mathbb{R}} |\psi_N(r)|^2 r dr \geq 2\pi \int_0^N r dr = \frac{N^2}{2} \tag{2.26}$$

$$\int_{\mathbb{R}^2} (|\nabla\psi_N(x,y,\lambda)|^2 dxdy = \frac{\pi}{2} \int_N^{2N} |\frac{x\hat{i}+y\hat{j}}{ln(N)(x^2+y^2)}|^2 r dr$$

$$= \frac{\pi}{2} \int_N^{2N} \frac{1}{ln^2(N)(x^2+y^2)} r dr = \frac{\pi}{2ln^2(N)} \int_N^{2N} \frac{dr}{r} = \frac{\pi}{2ln(N)} \tag{2.27}$$

Thus the functional in 2.23 can be bounded above using this sequence of functions

$$sup_m inf_{\psi\in\psi_m^\perp} \frac{\int_{\mathbb{R}^2} -(|\nabla\psi(x,y,\lambda)|^2 + k_0^2(\lambda)n^2(x,y,\lambda)|\psi(x,y,\lambda)|^2) dxdy}{\int_{\mathbb{R}^2} |\psi(x,y,\lambda)|^2 dxdy} \tag{2.28}$$

$$\geq -\frac{\pi}{N^2 ln(N)} + \frac{\int_{\mathbb{R}^2} k_0^2(\lambda)n^2(x,y,\lambda)|\psi(x,y,\lambda)|^2) dxdy}{\int_{\mathbb{R}^2} |\psi(x,y,\lambda)|^2 dxdy} \tag{2.29}$$

$$\geq -\frac{\pi}{N^2 ln(N)} + \int_{\mathbb{R}^2} \left[k_0^2(\lambda)n^2(x,y,\lambda) - n_0^2(\lambda)\right] dxdy + n_0^2(\lambda) \tag{2.30}$$

For sufficiently large N, the condition $\frac{\pi}{N^2 ln(N)} < \int_{\mathbb{R}^2} \left[k_0^2(\lambda)n^2(x,y,\lambda) - n_0^2(\lambda)\right] dxdy$ can be fulfilled, thus providing a candidate $\psi_N(x,y,\lambda)$ to make the functional in equation 2.23 positive. this establishes the existence of *weak* solutions of the scalar wave equation in two dimensions. Consequently finite element method can be applied to equation 2.23.

When multiple eigenvalues exist for linear eigenvalue differential equations, the eigenmodes are orthogonal. For an optical fiber this means that the different spatial modes for a particular wavelength do not intermix, as long as they exist and as long as there is no irregularity in the waveguide. Thus power conversion between such modes have to be induced by modifying the structure of the fiber locally.

2.1.6 Mode conversion theory

Only the scalar wave equation 2.22 has been used to study mode conversion in this thesis. The overlap of two eigenmodes $E_m(x,y,\lambda)e^{i\beta_m(\lambda)z}$ and $E_n(x,y,\lambda)e^{i\beta_n(\lambda)z}$ is defined as

$$< E_m(x,y,\lambda)e^{i\beta_m(\lambda)z}, E_n(x,y,\lambda)e^{i\beta_n(\lambda)z} >$$
$$< A(x,y), B(x,y) >= \frac{\int_{\mathbb{R}^2} A(x,y)\overline{B(x,y)}dxdy}{\sqrt{\int_{\mathbb{R}^2} A(x,y)\overline{A(x,y)}dxdy \quad \int_{\mathbb{R}^2} A(x,y)\overline{B(x,y)}dxdy}} \tag{2.31}$$

Modes corresponding to distinct eigenvalues $\beta_m(\lambda)$ and $\beta_n(\lambda)$ of equation 2.22 have zero overlap: $< E_m(x,y,\lambda)e^{i\beta_m(\lambda)z}, E_n(x,y,\lambda)e^{i\beta_n(\lambda)z} > \quad = 0 \quad \forall m \neq n$. The modes locally interact when the orthogonality of the waveguide is broken e.g. by non-adiabatic perturbation of the fiber using physical deformation, local heating, acousto-optic effect [54], laser exposure [31] etc. For example, at an ideal sudden discrete jump in the core refractive index at the location Z along the fiber axis:

$$\lim_{\Delta z \to 0, \Delta z > 0} < E_m(x,y,\lambda)e^{i\beta_m(\lambda)Z-\Delta z}, E'_n(x,y,\lambda)e^{i\beta'_n(\lambda)Z+\Delta z} > \quad \neq 0 \tag{2.32}$$

where $E_m(x,y,\lambda)e^{i\beta_m(\lambda)z}$ and $E'_n(x,y,\lambda)e^{i\beta'_n(\lambda)z}$ are the fields for the pristine fiber and the modified field for $z < Z$ and $z > Z$, respectively. However, the modes still interact very weakly when the intermodal dispersion $\delta\beta(\lambda) = \beta_m(\lambda) - \beta'_n(\lambda)$ has large magnitude for $m \neq n$. The normalized average value of the overlap integral over a beat length $T = \frac{2\pi}{\delta\beta(\lambda)}$ of the two modes can be very small:

$$\delta\beta(\lambda) \int_T \int_{\mathbb{R}^2} < E_m(x,y,\lambda)e^{i\beta_m(\lambda)z}, E'_n(x,y,\lambda)e^{i\beta'_n(\lambda)z} > dz << 1 \quad \forall |\delta\beta(\lambda)| \neq 0 \tag{2.33}$$

Only when a perturbation of the refractive index along the z direction, $n(x,y,z,\lambda) = \sqrt{\frac{\epsilon(x,y,z,\lambda)}{\epsilon_0(\lambda)}}$ has a periodic component of periodicity T, strong mode conversion is achieved near the resonance wavelength(s) λ_{MC} satisfying $|\delta\beta(\lambda_{MC})| = \frac{2\pi}{T}$.

$$\delta\beta(\lambda) \int_T \int_{\mathbb{R}^2} < E_m(x,y,\lambda)e^{i\beta_m(\lambda)z}, E'_n(x,y,\lambda)e^{i\beta'_n(\lambda)z} > dz \neq 0 \tag{2.34}$$

Such perturbations often have a finite length along z, especially when induced with a focused laser spot, which is hereafter referred to as a "mark". For periodic and repeatable exposure of marks, the mode coupling over a period of length Λ_{MC} can be simplified to a single parameter $\kappa(\lambda)$. This is a measurable quantity for N marks with the ratio of the mark length along z to the period length (duty cycle[1]) less than 1, due to the following

[1] Duty cycle of a periodic perturbation, such that the marks are non-overlapping, is defined as the ratio of the effective mark length L_{mark} along the fiber axis z to the period length Λ_{MC}. The effective mark length along z is obtained by fitting a rectangle function over z to the refractive index perturbation describing the mark, together with a baseline of value equal to the refractive index of the unperturbed core.

equation describing the power conversion $I_1(\lambda) \rightarrow I_2(\lambda)$ at wavelength λ from mode 1 to mode 2 [55; 56] :

$$\frac{I_2(\lambda)}{I_1(\lambda)} = \frac{\kappa^2(\lambda)}{\xi^2(\lambda)} sin^2(\xi(\lambda) N\Lambda_{MC}) \tag{2.35}$$

where the following parameters completely describe lossless mode conversion

$$\xi(\lambda) = \sqrt{\kappa^2(\lambda) + \delta^2(\lambda)} \tag{2.36}$$

Detuning parameter $$\delta(\lambda) = \frac{1}{2}\delta\beta_{MC}(\lambda) - \frac{\pi}{\Lambda_{MC}} \tag{2.37}$$

Average intermodal dispersion over Λ_{MC} $$\delta\beta_{MC}(\lambda) = \frac{1}{\Lambda_{MC}} \int_z^{z+\Lambda_{MC}} \delta\beta(\lambda, z')\ dz'$$

(2.38)

where a new MC period is starting at z. Since the the relevant parameters for mode conversion are the coupling and phase accumulation over a period length, describing mode conversion in terms of local values $\delta\beta_{MC}(\lambda, z)$ and $\kappa(\lambda, z)$ [55] of these quantities is avoided. Also, the local values are hard to measure without microscopy whereas chapters 6 and 7 describe methods for measuring the coupling and phase accumulation over a period length only using the spectra of the modes. The full complex amplitude over N full periods $z = N\Lambda_{MC}$, which represents the length of a standard MC grating with N periods, is described by [55; 56]:

$$\begin{bmatrix} E_1(\lambda, N\Lambda_{MC}) \\ E_2(\lambda, N\Lambda_{MC}) \end{bmatrix} = M(\lambda, N) \begin{bmatrix} E_1(\lambda, 0) \\ E_2(\lambda, 0) \end{bmatrix} \tag{2.39}$$

where the transfer matrix $M(\lambda, N)$ is a function of $\kappa(\lambda)$, $\delta(\lambda)$ and N in the following way:

$$M(\lambda, N) = \begin{bmatrix} cos(\xi(\lambda)N\Lambda_{MC}) + i\frac{\delta(\lambda)}{\xi(\lambda)} sin(\xi(\lambda)N\Lambda_{MC}) & i\frac{\kappa(\lambda)}{\xi(\lambda)} sin(\xi(\lambda)N\Lambda_{MC}) \\ i\frac{\kappa(\lambda)}{\xi(\lambda)} sin(\xi(\lambda)N\Lambda_{MC}) & cos(\xi(\lambda)N\Lambda_{MC}) - i\frac{\delta(\lambda)}{\xi(\lambda)} sin(\xi(\lambda)N\Lambda_{MC}) \end{bmatrix}$$

$$\implies M(\lambda, N) = M(\lambda, 1)^N \tag{2.40}$$

The transfer matrix $M(\lambda, N)$ in equation 2.40 should also be able to represent the phase $\delta\beta(\lambda)z$ added between the two modes over a length $z = N\Lambda_{MC}$ in the pristine fiber, which is represented by $\kappa(\lambda) = 0$. Indeed for $\kappa(\lambda) = 0$, $\xi(\lambda) = \frac{\delta\beta(\lambda)}{2} - \frac{\pi}{\Lambda_{MC}}$, thereby reducing

$M(\lambda, N)$ to the following matrix:

$$M(\lambda,N)|_{\kappa=0,\Lambda_{MC}=\infty} = \begin{bmatrix} cos(\phi(\lambda)) + i\ sin(\phi(\lambda)) & 0 \\ 0 & cos(\phi(\lambda)) - i\ sin(\phi(\lambda)) \end{bmatrix} = \begin{bmatrix} e^{i\phi(\lambda)} & 0 \\ 0 & e^{-i\phi(\lambda)} \end{bmatrix} \tag{2.41}$$

where $\phi(\lambda) = \frac{\delta\beta(\lambda)N\Lambda_{MC}}{2} - N\pi$. The matrix in equation 2.41 indeed represents a phase shift of $2\phi(\lambda) = \delta\beta(\lambda)N\Lambda_{MC}$ between the two modes for a length $N\Lambda_{MC}$ of the pristine fiber. Following similar convention for representing phase shift over a length of the pristine fiber, extra phase shift corresponding to gap of length Λ_s can be represented by [57]:

$$P(\lambda,\Lambda_s,\delta\beta(\lambda)) = \begin{bmatrix} e^{i\frac{\delta\beta(\lambda)\Lambda_s}{2}} & 0 \\ 0 & e^{-i\frac{\delta\beta(\lambda)\Lambda_s}{2}} \end{bmatrix} \tag{2.42}$$

Thus an MC of M segments with constant pitch Λ_{MC} and mark shape, along with phase shift between every segment can be represented as

$$\begin{bmatrix} E_1(\lambda, \sum_j (N_j\Lambda_{MC} + \Lambda_{s,j})) \\ E_2(\lambda, \sum_j (N_j\Lambda_{MC} + \Lambda_{s,j})) \end{bmatrix} = \left[\Pi_{j=0}^{N} P(\lambda,\Lambda_{s,j})M(\lambda,N_j)\right] \begin{bmatrix} E_1(\lambda,0) \\ E_2(\lambda,0) \end{bmatrix} \tag{2.43}$$

where N_j is the number of marks in the j^{th} segment and $\Lambda_{s,j}$ is the length of the (possible) gap after the j^{th} segment. When estimates of $\delta\beta(\lambda)$, $\delta\beta_{MC}(\lambda)$ and $\kappa(\lambda)$ are available, this representation can be used to simulate both phase-shifted and chirped MCs.

2.1.7 Simulation of discrete segment

Mode-solving of complicated irradiation profiles across the transverse directions of a step-index fiber can be done using finite element method. One model for simulating irradiation of distinct and repeatable laser marks is to consider the modified waveguide at the irradiated zones along the transverse axes of the fiber, which is uniform along the fiber axis for the effective length of the irradiation [46]. Figure 2.5 shows a simple example, where the index change still has a step-index profile due to uniform irradiation: $n_1'(\lambda)$, $\delta\beta'(\lambda)$, Λ_M' represent the core index, intermodal dispersion between two modes described by fields $E_1(\lambda, z)$ and $E_2(\lambda, z)$ and the length of the irradiated segment equivalent

to mark length, respectively. $n_1(\lambda)$, $\delta\beta(\lambda)$, Λ_M represent same for an unirradiated segment, the length of which is defined as $\Lambda_M = \Lambda_{MC} - \Lambda'_M$ where Λ_{MC} is a full period of the axial profile with periodic perturbation. Figure 2.5 describes the scheme for such a periodic perturbation. Symbols with ' sign belong to the modified segment.

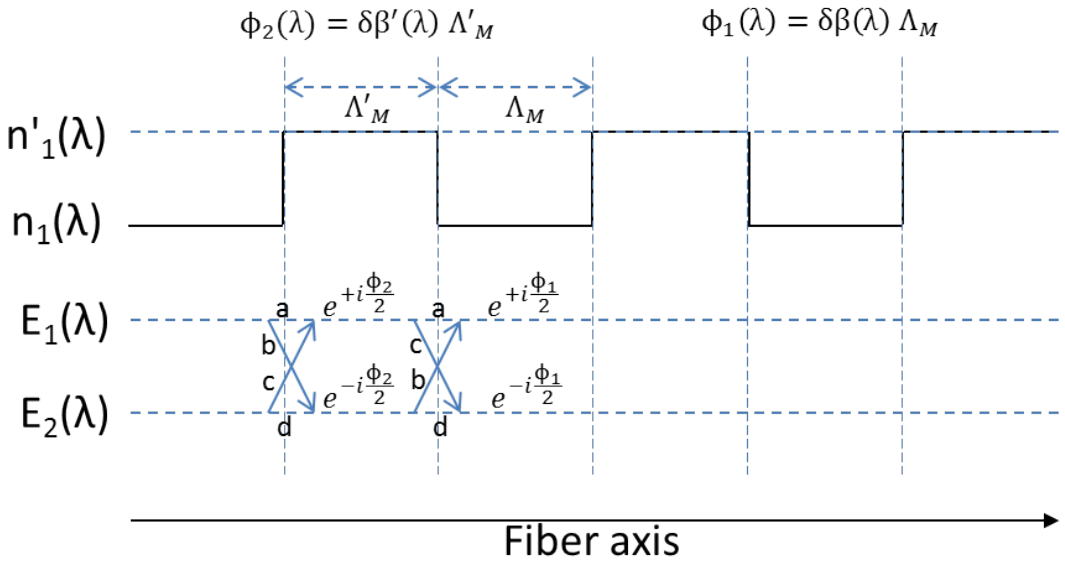

Figure 2.5 – Discrete segment model for simulating a periodic laser exposure, where Λ'_{MC} represents the mark length and Λ_M is defined as $\Lambda_M = \Lambda_{MC} - \Lambda'_M$. The duty cycle is given by $\frac{\Lambda'_M}{\Lambda_{MC}}$

Assuming the mode travelling from negative to positive z, the coupling at the starting boundary of irradiated segment is defined by the matrix of overlap integrals. For $\Delta z > 0$ this is given by

$$\lim_{\Delta z \to 0} \begin{bmatrix} E_1(z+\Delta z, \lambda) \\ E_2(z+\Delta z, \lambda) \end{bmatrix} = C(\lambda) \lim_{\Delta z \to 0} \begin{bmatrix} E_1(z-\Delta z, \lambda) \\ E_2(z-\Delta z, \lambda) \end{bmatrix} \tag{2.44}$$

$$C(\lambda) = \lim_{\Delta z \to 0} \begin{bmatrix} < E_1(z-\Delta z, \lambda), E'_1(z+\Delta z, \lambda) > & < E_1(z-\Delta z, \lambda), E'_2(z+\Delta z, \lambda) > \\ < E_2(z-\Delta z, \lambda), E'_1(z+\Delta z, \lambda) > & < E_2(z-\Delta z, \lambda), E'_2(z+\Delta z, \lambda) > \end{bmatrix} \tag{2.45}$$

where $E_k(z, \lambda)$ and $E'_k(z, \lambda)$ represent the transverse mode amplitudes of the k^{th} mode in the unirradiated and irradiated segments, respectively. At the ending boundary of an irradiated segment, the coupling is given by the matrix $C^T(\lambda)$, which is the transpose of $C(\lambda)$. For repeated exposures of length $\Lambda_{MC} = \Lambda'_M + \Lambda_M$ with possible extra gaps of

length $\Lambda_{s,j}$ after the j^{th} segment , complex mode amplitudes are given by:

$$\begin{bmatrix} E_1(\lambda, \sum_j \left(N_j \Lambda_{MC} + \Lambda_{s,j}\right)) \\ E_2(\lambda, \sum_j \left(N_j \Lambda_{MC} + \Lambda_{s,j}\right)) \end{bmatrix} = \begin{bmatrix} \Pi_{j=0}^{N} P(\lambda, \Lambda_M + \Lambda_{s,j}) & C^T(\lambda) & P'(\lambda, \Lambda'_{M,j}) & C(\lambda) \end{bmatrix} \begin{bmatrix} E_1(\lambda, 0) \\ E_2(\lambda, 0) \end{bmatrix} \tag{2.46}$$

$P'(\lambda, \Lambda'_{M,j}) = P(\lambda, \Lambda'_{M,j}, \delta\beta'(\lambda))$ is the phase matrix in the modified region. This model is useful for simulating complex transverse inverse profiles of the irradiated segments, especially when the simulation algorithm cannot compute the effect of continuous change of the index profile over z in the modified segment.

2.2 Conclusions

This chapter discusses the existence of modes for two-dimensional waveguides in $x-y$ plane with an refractive index bump inside a constant cladding index, which satisfies (a) the bump equals cladding index outside a finite region in the $x-y$ plane (defined as core), (b) the index is bounded, and (b) the average of the core-cladding index difference is positive and finite. Existence of weak solutions can be found from the variational formulation of stationary Maxwell's equation. Such a formulation also allows the use of finite element method for arbitrary two-dimensional waveguides. The particular case of annular index regions is solvable semi-analytically, which gives a method for comparing the accuracy of finite element method. Classification of the modes of prototypical step-index fibers are discussed, under different assumptions. The approximation of LP modes is used for the rest of this thesis.

Periodic local modifications of the fiber can lead to coupling of modes under certain conditions, namely (a) breaking the orthogonality of the modes locally and (b) matching the intermodal dispersion of the interacting modes with the wavevector of the periodic modification. Two general models for simulating MCs are discussed:

- Model based on coupling theory, which is useful for simulating standard, phase-shifted and chirped MCs when experimental estimates of $\delta\beta(\lambda)$, $\delta\beta_{MC}(\lambda)$ and $\kappa(\lambda)$ are available.
- Approximate model based on discrete segments, which is useful for simulating standard, phase-shifted and chirped MCs when the transverse index profile of the modified segment is complicated and needs to be solved for modes using finite element method.

3 Sample details, preparation and general experimental methods

This chapter describes the few-mode fiber (FMF), a method to selectively excite modes, methods to fabricate fiber Bragg gratings (FBG) and mode converter gratings (MC), and the spectroscopy apparatus. All FMF experiments presented in this thesis are based on this particular fiber. In conjugation with the mathematical tools in Chapter 2, the hardware tools and experimental methods listed here form the backbone of this thesis.

3.1 Few-mode fiber

The few-mode fiber used in this thesis exhibits four LP modes LP_{01}, LP_{11}, LP_{21} and LP_{02} (introduced in chapter 2.1.3) in the wavelength range of 1.46 μm to 1.72 μm. The transverse refractive index profile for a single 50 cm long sample of this fiber was measured by the company Interfiber Analysis LLC, using spatially resolved Fourier transform spectroscopy [58]. The refractive index profile along a diameter of the cross section of the fiber is shown in figure 3.1, for two different wavelengths.

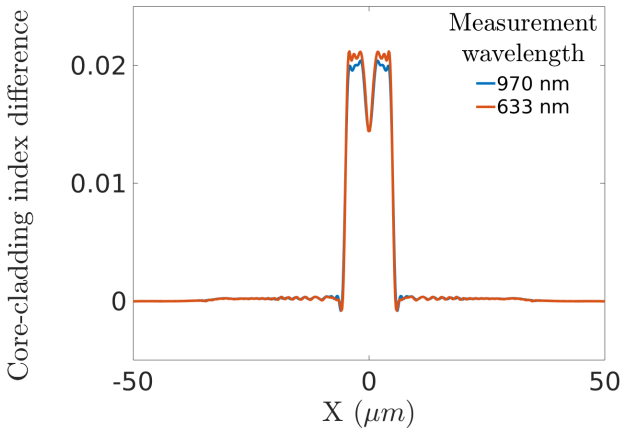

Figure 3.1 – Diametric refractive index profile of the FMF, offset by the cladding index, as obtained from Interfiber Analysis LLC

The core size is 10.0 ± 0.05 μm. In the core region, the calculated average refractive index difference between the core and cladding is 0.021 at 633 nm wavelength and 0.020 at 970 nm wavelength. The refractive index distribution along the measured diameter resembles a step-index profile, other than a dip in the center of the fiber. Assuming step-index profile, the V number in the wavelength measurement range from 1.46 μm to 1.72 μm varies from approximately 4.4 to 5.2. Thus in terms of LP modes, the fiber is a four-mode fiber in this wavelength range. The refractive index was assumed to be a linear combination of fused silica and germanium oxide refractive indices, which are described by Sellmeier equations [7; 8]. To match the index contrast, the germanium concentration was determined to be approximately 14 %. According to the purchased measurement report from Interfiber Analysis LLC, compared to silica index matching liquid, the fiber cladding had an index difference of -0.0004, suggesting that its draw tension was around 80 grams[59].

The local refractive index of the fiber $n(\lambda, x, y, z)$ is assumed to be a linear combination of the refractive index of fused silica $n_{SiO_2}(\lambda)$ and Germanium oxide $n_{GeO_2}(\lambda)$ [60]:

$$n(\lambda, x, y, z) = (1 - f(x, y, z))\, n_{SiO_2}(\lambda) + f(x, y, z)\, n_{GeO_2}(\lambda) \tag{3.1}$$

where $f(x, y, z)$ is the fractional concentration of GeO_2 at the location (x, y, z) in the fiber. Under the assumption that the centrosymmetric fiber has the same refractive index profile at any cross-section of the fiber, $f(x, y, z) = f(r)$, where $r = \sqrt{x^2 + y^2}$.

Sellmeier equation for refractive index $n(\lambda)$ is given by the following formula

$$n^2(\lambda) - 1 = \sum_{i=1}^{3} \frac{A_i \lambda^2}{\lambda^2 - B_i^2} \tag{3.2}$$

Table 3.1 presents the values of the Sellmeier coefficients for fused SiO_2 and GeO_2.

Material	A_1	B_1	A_2	B_2	A_3	B_3
Fused SiO_2 [7]	0.6961663	0.0684043	0.4079426	0.1162414	0.8974794	9.896161
GeO_2 [8]	0.80686642	0.068972606	0.71815848	0.15396605	0.85416831	11.841931

Table 3.1 – Sellmeier coefficients of fused SiO_2 [7] and GeO_2 [8]

Representing this fiber with a perfect step-index profile with radius a_{core} and 14 % Germanium concentration at the core ($f(r < a_{core}) = 0.124$), and using Sellmeier equations for the wavelength dependence of fused silica and Germanium oxide, V-numbers can be calculated for different wavelengths. Table 3.2 shows approximate V-numbers at the edges of wavelength measurement range, at the center of the telecom wavelength range at 1.55

μm, and at the wavelength where the V-number reaches the cut-off condition of LP_{02}, i.e., V=3.832. For the step-index model, the cut-off wavelength of the LP_{02} is thus within the interval 1.985±0.005 μm. Since the upper limit of wavelength measurement at 1.72 μm is far from the LP_{02} cut-off wavelength, and the V-number at at 1.46 μm is smaller than the cut-off wavelength of the next LP mode, the first four LP modes LP_{01}, LP_{11}, LP_{21} and LP_{02} are supported in 1.46 μm-1.72 μm. Table 3.2 represents the indicative V-numbers calculated based on the core and cladding refractive indices at different wavelengths, particularly corresponding to the edges of the available measurement range, the center of the telecom wavelength range and calculated GVE from step-index simulations for different LP_{01}-$LP_{\hat{m}l}$ mode pairs.

Description	Wavelength	V-number	Refractive index	
	(μm)		cladding	core
Lower limit of SI 155 interrogator	1.46	5.19	1.445	1.465
Center of telecom wavelength	1.55	4.89	1.444	1.464
Measured LP_{01}-LP_{02} GVE	1.64	4.63	1.443	1.463
Upper limit of Ando OSA 6317Q	1.72	4.41	1.442	1.462
Simulated LP_{01}-LP_{21} GVE	1.97	3.86	1.438	1.459
Simulated LP_{21} and LP_{02} cut-off	1.98	3.84	1.438	1.459
Simulated LP_{01}-LP_{11} GVE	2.64	2.91	1.427	1.448

Table 3.2 – Specific wavelengths corresponding to the measurement setups and the step-index modeling of the few-mode fiber, together with the corresponding V-number, core refractive index and cladding refractive index

Although LP_{01} can potentially be converted to LP_{11} [2] or LP_{21} [61; 62], that was not pursued in this thesis since the intermodal dispersion curves of LP_{01}-LP_{11} and LP_{01}-LP_{21} mode pairs could not be estimated due to the inability to selectively excite these mode pairs with available setup. The cut-off wavelengths of LP_{11} and LP_{21} modes are larger than that of LP_{02}. According to the step-index simulation (table 3.2), the GVE wavelengths for both the LP_{01}-LP_{11} and LP_{01}-LP_{21} mode pairs are beyond 1.8 μm, which was above the measurement limit of available spectroscopic setup .

3.2 Lasers

The properties of the lasers used in this thesis are listed below:

Laser (Company)	Pulse duration	Wavelength	Average power	$\frac{1}{e^2}$ diameter	Repetition frequency	Phase mask pitch
	(s)	(nm)	(mW)	(mm)	(Hz	(μm))
Argon, 2H (Coherent)	CW	244	200*	0.6*	–	1.060
ArF Excimer (Coherent)	15×10^{-9}	193	150	20 (|| to fiber), 8 ($\perp$ to fiber)	10	1.07931
ArF Excimer (Optec)	6×10^{-9}	193	150	N.A.**	200	–
fs laser Yb:YAG, 4H (Pharos)	0.18×10^{-12}	257	40*	4.1*	1000	–

Table 3.3 – Lasers used during the thesis. Values indicated with * are measured, while the others are specified by the corresponding manufacturing companies. The Coherent excimer laser had rectangular beam shape, whereas the other lasers had elliptical beam shape. ** For the commercial Optec Excimer laser setup, the beam diameter was not available, whereas only the spot size was measured from fluorescence of the fiber core as seen under a microscope. Average power for a periodically sequenced pulses is defined over the sequence period, which was the quantity measured by power meters

2H and 4H implies second and fourth harmonic, respectively, of the fundamental beam with 1030 nm wavelength. The higher harmonic wavelengths were generated using high-harmonic modules adjoined to the Pharos laser. The Argon laser model was Sabre FRED. The Optec excimer laser is located in the CMI facility of EPFL. It is provided as a package complete with microscope, apertures and translation stage by the company Atlex. All the parts of the Atlex system could be controlled from the same computer. For the other two systems, Matlab was used to communicate between the spectrometers, translation stages and laser/shutters.

3.3 Fiber-Bragg grating fabrication

Fiber Bragg-gratings are periodic perturbations in the index profile along the fiber axis, the wavevector of which matches the difference in axial wavevectors of two counter-propagating modes [63; 64; 65]. Reflection peak(s) is(are) observed at wavelength(s) where the perturbation wavevector $\frac{2\pi}{\Lambda_{FBG}}$ matches the difference of in axial wavevectors of any two counter-propagating modes: $\Lambda_{FBG}|\vec{\beta}_1(\lambda) - \vec{\beta}_2(\lambda)| = \beta_1(\lambda) - (-\beta_2(\lambda)) = \beta_1(\lambda) + \beta_2(\lambda) = \frac{2\pi}{\Lambda_{FBG}}$ [66].

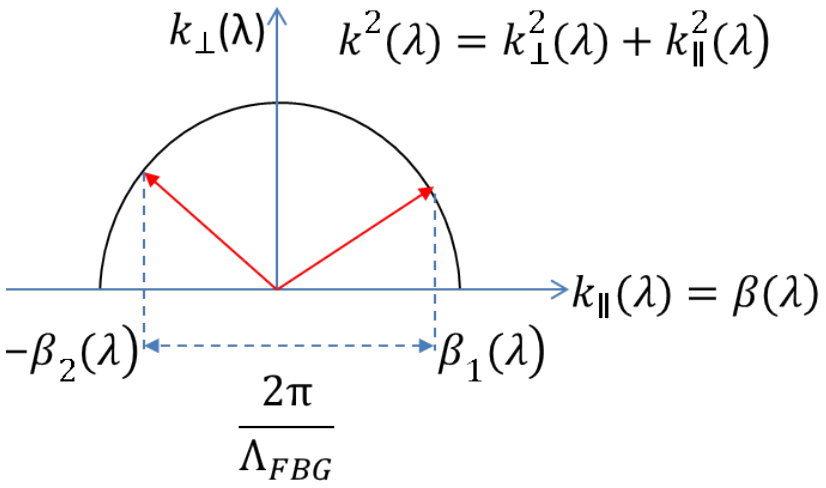

Figure 3.2 – Phase matching of an FBG: Matching of the difference in axial wavevectors of a forward ($\beta_1(\lambda)$) and backward propagating mode, ($-\beta_2(\lambda)$)

The method used in this thesis to introduce such index perturbations was illumination from the side though a phase mask [1].

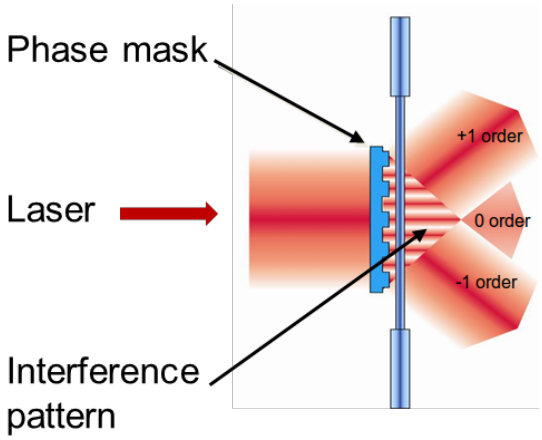

Figure 3.3 – Phase mask side-illumination for fabricating FBG [1]

The Argon laser and Coherent ArF excimer [1] laser were used for writing FBGs reported

in this thesis, with corresponding phase masks of pitch 1060 nm from Ibsen photonics and 1079.31 nm from QPS technology, respectively. A cylindrical fused silica lens was used to focus the Coherent excimer beam perpendicular to the fiber, with an estimated $\frac{1}{e^2}$ diameter of 0.5 mm perpendicular to the fiber. The estimates of corresponding energy density per pulse (energy per pulse / spot size at fiber location) and total fluence (energy density per pulse × number of pulses = average intensity × exposure time) were 150 mJcm^{-2} and 900 Jcm^{-2} respectively. The phase masks consist of periodic lines etched in silica, thus forming a line grating. The period of the grating is chosen to be the desired pitch of the FBG. When laser was illuminated perpendicular to the phase mask, multiple diffraction orders were transmitted through the phase mask. The depth of the periodic lines of the masks were adjusted such that power in the 0^{th} order diffraction is minimized. The -1 and +1 diffraction orders have the maximum transmitted power. The interference of these two orders is imprinted in the photosensitive core of the optical fiber. The UV absorbing coating of the fiber was removed by mechanical stripping, in order to expose the fused silica cladding. The residues were cleaned by wiping with isopropanol, so that residues do not contaminate the delicate phase mask. Sufficient length of coating was removed from the fiber such that the coating does not touch the phase mask. On the other hand, the removed length of the coating was limited such that on both sides of the removed region, the coating touches the unpatterned boundary of the phase mask, in order to control vibration instabilities. During irradiation, the contact was maintained by applying slight controlled strain.

Generally the index profile of the modified core for standard FBGs at any fixed wavelength is represented by [56]

$$n_1(z) = n_0(z) + \Delta n_{dc}(z)\left(1 + v(z)\ cos(\frac{2\pi}{\Lambda_{FBG}}z + \phi_0)\right) \tag{3.3}$$

where $\Delta n_{dc}(z)$ is the induced refractive index change averaged over a grating period with center at z, $v(z) \leq 1$ is the fringe visibility at z, and ϕ_0 is some constant. An illustration of an FBG represented by equation 3.3 , with $\Lambda_{Phasemask} = 1$ μm and therefore $\Lambda_{FBG} = 0.5$ μm, Gaussian $\Delta n_{dc}(z) = 0.006\ e^{(\frac{z-600}{25})^2}$ with z in microns, $n_0(z) = 1.463$ and $v(z) = 0.85$ is presented in figure 3.4. The pitch of the interference of the -1 and +1 diffraction orders was half of the phase mask pitch. The minima of the perturbations are slightly raised from the baseline, which represents a loss in contrast, corresponding to $v(z) < 1$. Such loss of contrast can arise from vibrations, which is why contact is maintained between the fiber coating and unpatterned edges of the phase mask during irradiation. For no loss of contrast, corresponding to $v(z) = 1$, the minima of the perturbations will touch the baseline. Since refractive index change induced by the Gaussian shaped Argon laser beam in the few-mode fiber is positive, such an illustration represents a realistic perturbation profile in presence of some vibration, when the index change in linear.

For two counter-propagating modes with magnitudes of propagation constants $\beta_x(\lambda)$ and

$\beta_y(\lambda)$, reflection peaks for an FBG with pitch Λ_{FBG} appear centerd at the resonance wavelengths $\lambda_{x,y}$ where the following condition is satisfied [66]:

$$2M\pi = \Lambda_{FBG}\Big[\beta_x(\lambda_{x,y}) + \beta_x(\lambda_{x,y})\Big], \quad M \in \mathbb{N} \tag{3.4}$$

$$\text{or} M\lambda_{x,y} = \Lambda_{FBG}\Big[n_{e,x}(\lambda_{x,y}) + n_{e,y}(\lambda_{x,y})\Big], \quad M \in \mathbb{N} \tag{3.5}$$

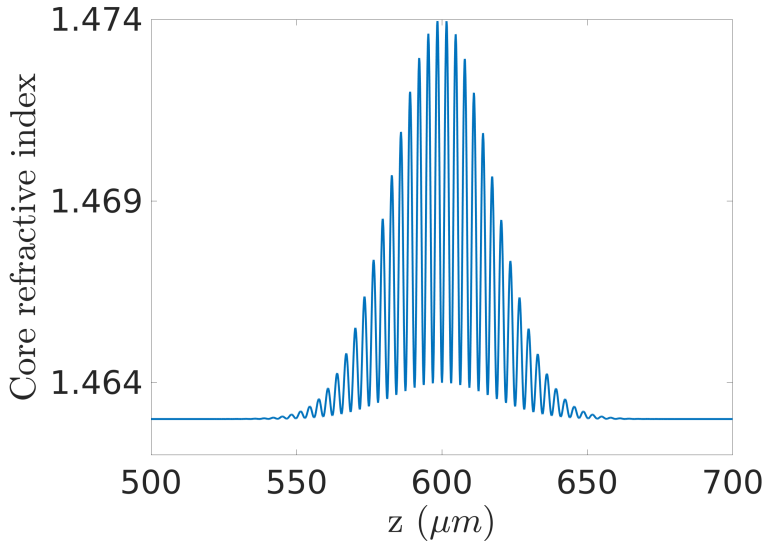

Figure 3.4 – Illustration of an FBG represented by equation 3.3 , with $\Lambda_{FBG} = 0.5$ μm, Gaussian $\Delta n_{dc}(z) = 0.006\ e^{(\frac{z-600}{25})^2}$ with z in μm, $n_0(z) = 1.463$ and $v(z) = 0.85$. An FBG fabricated with this refractive index profile along the fiber axis would have resonance wavelengths 1.4690 μm, 0.7345 μm and 0.4897 μm for the first ($M = 1$), second ($M = 2$) and third order ($M = 3$) reflection peaks respectively

The reflection strength (normalized intensity) at the resonance wavelength(s) $\lambda_{x,y}$ of the FBG is(are) described by the following formula [66]:

$$R(\lambda_{x,y}) = tanh^2(\kappa L) \tag{3.6}$$

where L is the length of the FBG. The coupling constant κ is defined by:

$$\kappa = K_F\ \eta_{x,y}\ \frac{\Delta n_{ac}}{\lambda_{x,y}} \tag{3.7}$$

$\eta_{x,y}$ is the overlap integral of the two counter propagating modes at $\lambda_{x,y}$ inside the core of the fiber. K_F is a constant which depends on the envelope of the irradiation. For top-hat profile FBGs $K_F = \pi$. The $tanh^2(\kappa L)$ functionality implies that even for small κ, FBGs can be made strongly reflecting by increasing the length L.

3.4 Mode converter fabrication using laser irradiation

Mode converter gratings are periodic perturbations in the index profile along the fiber axis, the wavevector of which matches the difference in axial wavevectors of two co-propagating modes (Figure 3.5). Conversion peak(s) is(are) observed at wavelength(s) where the perturbation wavevector matches the difference in axial wavevectors of any two modes, which is called resonance wavelength [56]. The perturbations can be made using arcs [67], CO_2 laser [39], UV laser [31] etc. Although modes with different symmetry can be coupled in reflection with non-uniform transverse index change of the core by laser irradiation [68], it takes sophisticated fabrication strategies to couple co-propagating modes of different symmetry using MCs [39]. This is mainly because of the coupling constant between modes of different symmetry is very small for an MC without tilt, unlike FBGs where the coupling constant is large.

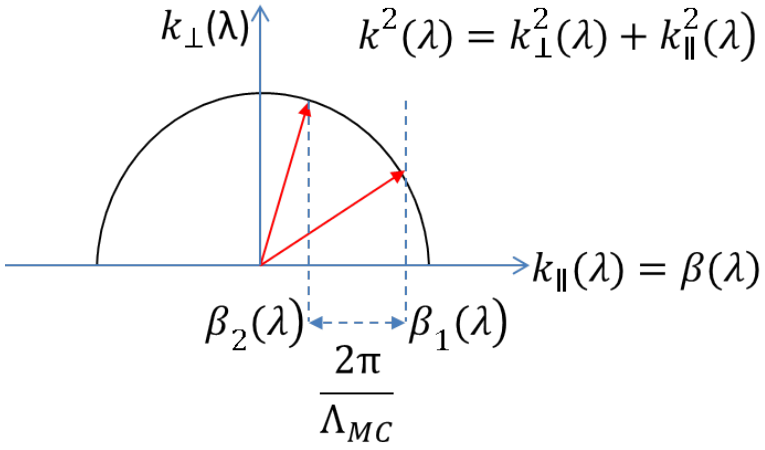

Figure 3.5 – Phase matching of an MC: Matching of the difference in axial wavevector of two different co-propagating modes, $\beta_1(\lambda)$ and $\beta_2(\lambda)$

For two co-propagating modes with magnitudes of propagation constants $\beta_x(\lambda)$ and $\beta_y(\lambda)$, and an MC with pitch Λ_{MC}, the resonance wavelength $\lambda_{x,y}$ satisfies the following [66]:

$$2M\pi = \Lambda_{MC}|\beta_x(\lambda_{x,y}) - \beta_x(\lambda_{x,y})| \qquad M \in \mathbb{N} \tag{3.8}$$

$$\text{or} \quad M\lambda_{x,y} = \Lambda_{MC}|n_{e,x}(\lambda_{x,y}) - n_{e,y}(\lambda_{x,y})| \qquad M \in \mathbb{N} \tag{3.9}$$

The conversion strength of the MC, which is the ratio between the original and converted mode intensities at a given wavelength, is described by the following formula [66]:

$$T(\lambda) = \frac{\kappa^2(\lambda)}{\delta^2(\lambda) + \kappa^2(\lambda)} sin^2\left(L\sqrt{\delta^2(\lambda) + \kappa^2(\lambda)}\right) \tag{3.10}$$

where L is the length of the MC, $\kappa(\lambda)$ coupling constant as a function of wavelength and $\delta(\lambda) = |\frac{\beta_x(\lambda)-\beta_y(\lambda)}{2}| - \frac{\pi}{\Lambda_{MC}}$ is defined by the intermodal dispersion $|\beta_x(\lambda) - \beta_y(\lambda)|$ and MC pitch Λ_{MC}. The detailed mathematical model of MC transmission and extinction ratio has been described in more detail in chapter 2.1.6. For fabrication of MCs in this thesis, the fiber was iteratively translated along the fiber axis, while exposing it with the laser for controlled periods of time between the translations [2]. An illustration is shown in figure 3.6. The point-by-point irradiation using a high-precision translation stage, instead of using an amplitude mask, gave more flexibility and resolution in choosing the value of the pitch. The flexibility and precision is crucial since slight changes in pitch cause large shift in resonance wavelength. For the LP_{01}-LP_{02} mode pair in the wavelength range of 1.5 μm-1.7 μm, the sensitivity of resonance wavelength with respect to MC pitch $|\frac{\Delta\lambda_{MC}}{\Delta\Lambda_{MC}}| > 0.05$ (Detailed calculation in figure 4.8). The shutter could be an external shutter for the Argon laser, external trigger for the Optec Excimer laser [29], or pulse-picker of the femtosecond laser [69], all of which could be controlled with a master PC. The translation stage was Aerotech ANT130, which had a translation range of 5 cm in two perpendicular horizontal directions, and a resolution of 10 nm. From the practical viewpoint, it is crucial to maintain suitable ratio of the perturbation size along the axis to the period length (duty cycle), in order to achieve high-extinction MC conversion [70].

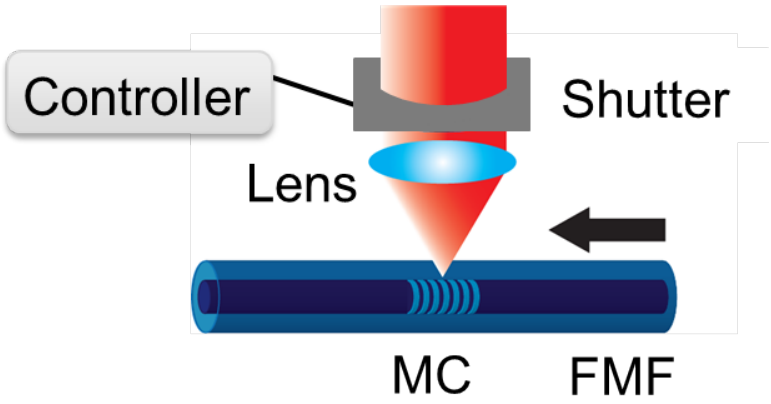

Figure 3.6 – Illustration of MC irradiation using a translation stage and shutter [2]

3.5 Selective coupling of LP_{01} mode

Although it is ideally possible to in- and out-couple only the LP_{01} mode in the FMF by splicing with a SMF with same mode-field diameter as the LP_{01} mode of the FMF, in practice splicing with most fibers excites some amount of higher order mode. Especially while splicing with centrosymmetric SMF, centrosymmetric LP_{02} mode is excited whenever the mode field of LP_{01} is not matching between the SMF and FMF. This is especially problematic during the fabrication of strong LP_{01}-LP_{02} mode converters, due

to the presence of LP_{02} TMI, thus degrading the spectrum of the MC conversion peak. Consequently it becomes hard to determine high extinction ratios. To retain only LP_{01} at the region of irradiation and output of the FMF, the higher order modes are forced to experience stronger loss compared to LP_{01} under bending of the fiber [71; 72; 73]. Splicing OFS CS0424630 SMF pigtails excited approximately 5 % LP_{02} in the FMF. It was experimentally determined that 30 turns of diameter 7 mm got rid of LP_{02}, beyond the detection limit even at 99.99 % mode conversion by MCs. The loops were made by winding around the tip of a pen, which was then removed and arrested in place with scotch tapes. MC exposure was done on a part of the fiber between two consecutive loops. An example of fiber loops is shown in figure 3.7.

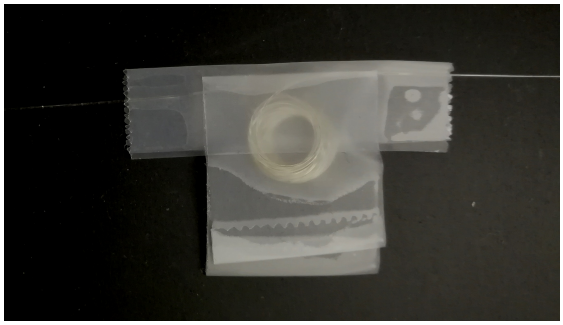

Figure 3.7 – Fiber loops for getting rid of higher order modes in MC samples

3.6 Spectroscopy apparatus

Two types of spectroscopic apparatus were used for different experiments-

- Micron Optics SI 155 interrogator, which had wavelength scanning laser output and photodetector at each of its 4 fiber-coupled ports, enabling direct reflection measurement from samples. For transmission measurements, the sample had to be attached between two ports, with an intermediate fiber isolator blocking any light going into one of the ports, including reflections from the sample. The acquisition time for the wavelength range 1.46 μm to 1.62 μm was 0.1 s. Therefore this was used whenever the wavelength range was sufficient.
- When larger spectral range needed to be measured, combination of SuperK Extreme broadband light source from NKT photonics with Ando OSA 6317Q spectrometer was used. Measurements in the wavelength range 1.5 μm to 1.7 μm were done with this device combination. Transmission signal could be measured by placing fiber samples between these two devices. For reflection experiments, both the devices were attached to the input port of a 50-50 fiber coupler, while the sample was attached on an output port. The output power of the SuperK Extreme broadband light source was low, thereby often requiring long acquisition times for decreasing the noise of the spectra.

4 Determination of intermodal dispersion in a few-mode fiber

Knowledge of the intermodal dispersion $\delta\beta(\lambda)$ of the pristine fiber is important for fabricating mode converters (MC) [30] as well as for understanding the temperature and strain response of both MCs [74] and TMI [75; 76]. Although it is long known how to measure the higher order dispersion coefficients of the intermodal dispersion curve using two-mode interferometry [77; 78], the offset of the dispersion curve is indeterminate due to phase offset indeterminacy inherent to any interferometric signal. A novel method is presented here which enables determining the offset of intermodal dispersion, using resonance peaks of an FBG written in the FMF [79]. Combining this method with the estimates of higher order dispersion terms from TMI, the intermodal dispersion was fully characterized for LP_{01}-LP_{02}. This estimate of $\delta\beta(\lambda)$ was used as a first guess for choosing the MC pitch for a desired resonance wavelength, on top of which more sophisticated estimation tools have been built in this thesis, as described in chapter 6.

Development of this method was inspired by the lack of methods for accurately estimating the intermodal dispersion of the pristine fiber including its offset. Only recently some methods were reported e.g. using imaging of the scattering of the modal beat pattern [80] or using acousto-optic gratings [54]. MC resonance using weak acousto-optic gratings can provide very accurate estimate of the offset of $\delta\beta(\lambda)$. Although acousto-optic gratings can only couple two modes with $\Delta\widehat{m} = \pm 1$ (Equation 2.20), as has been reported for LP_{01}-LP_{11} mode pair in reference [54], the method is easily scalable to other modes by sequential combination of different mode pairs with $\Delta\widehat{m} = \pm 1$ [81]. For example, first determining the intermodal dispersion of LP_{01}-LP_{11} followed by the determination of the intermodal dispersion of LP_{11}-LP_{02} with high precision, over a range of wavelength, will provide estimate for intermodal dispersion of LP_{01}-LP_{02} in that range using simple combination of the previous two estimates. The advantage of this method is that the same maximum coupling can be maintained for a smaller perturbation by increasing the coupling length, whereas the bandwidth of the conversion peaks decrease with increasing

length [35]. As claimed in [54], in this way, by using a long coupling length of 50 cm, it was possible to resolve the vector modes. LP modes are combinations of vector modes [44] under the assumption of degeneracy of modes with close dispersion values, and therefore the estimates of intermodal dispersion from vector modes can be used for estimating the intermodal dispersion of the corresponding LP mode. Since vector modes were not relevant for the experimental results and scope of this thesis, detailed discussion of vector modes is skipped here, and can be followed in the relevant textbook [44] if needed. Also since the index perturbation was small for a 50 cm long grating, the determined intermodal dispersion is close to its value in an unperturbed pristine fiber. Previous to the method of acousto-optic mode converter gratings and the novel method presented in this chapter, only very approximate methods existed for estimating the intermodal dispersion of a pristine fiber [82], which suffer from errors of neglecting significant contributions from some effects. On the other hand, while trying to estimate intermodal dispersion of the pristine fiber at the resonance wavelength of an MC written using strong perturbations, the estimation becomes biased since intermodal dispersion of the pristine and exposed fiber are significantly different [33; 34]. However strong perturbation is often necessary for fabricating an MC within a limited exposure length, and to obtain sufficient depth of the conversion peak such that the resonance wavelength can be determined with precision against the background noise in the transmission spectrum. Since the resonance wavelength varies strongly with the pitch, it becomes difficult to a priori estimate the needed pitch for a desired resonance wavelength, without having a good estimate of the intermodal dispersion. On the other hand, (a) FBGs which are a few mm long, with discernible reflection peaks, can be easily fabricated with small perturbations, and (b) the resonance peaks do not shift as strongly as an MC when the perturbation strength or the FBG pitch is changed. Especially based on these practical points, the presented method was developed and applied on fabricated FBGs in the few-mode fiber.

4.1 Mathematical description

Intermodal dispersion between two modes with propagation constants $\beta_1(\lambda)$ and $\beta_2(\lambda)$, where $\beta_2(\lambda) < \beta_1(\lambda)$, is defined as $\delta\beta(\lambda) = \beta_1(\lambda) - \beta_2(\lambda)$. Intermodal dispersion can be expressed as a Taylor expansion around a wavelength of interest, which is generally the GVE wavelength (also known as achromatic fringe) [77]:

$$\delta\beta(\lambda) = \sum_{n=0}^{\infty} \frac{1}{n!}(\lambda - \lambda_0)^n \frac{\partial^n \beta(\lambda_0)}{\partial \lambda^n} \tag{4.1}$$

With precise alignment, two modes of a few-mode fiber with real-valued electric field amplitudes $E_{\beta_1}(\lambda)$ and $E_{\beta_2}(\lambda)$ can be selectively excited by coupling the mode of a single mode fiber (SMF), with real-valued electric field amplitude $E_{SMF}(\lambda)$, at junction between the cleaves of these fibers e.g. splice or physical contact. The coupling can be further

varied by coupling the diffracted field after propagation outside the SMF cleave to the modes on the few-mode fiber at its cleaved end, at the expense of having lesser coupling and physical stability compared to a splice [83]. At splices on both ends of the few-mode fiber, if the normalized inner products $A_{\beta_1}(\lambda) =< E_{SMF}(\lambda), E_{\beta_1}(\lambda) >$ and $A_{\beta_2}(\lambda) =< E_{SMF}(\lambda), E_{\beta_2}(\lambda) >$ (equation 2.31)dominate with respect to the nomalized inner products of $E_{SMF}(\lambda)$ with other modes in the few-mode fiber, then the transmission spectrum through the SMF-FMF-SMF system shows particular oscillating intensity called two-mode interference (TMI) [77; 84; 85; 86], given by the following formula:

$$I_{TMI}(\lambda) = \quad I_{SMF}(\lambda)\ |A_{\beta_1}(\lambda)e^{iL\beta_1(\lambda)} + A_{\beta_2}(\lambda)e^{iL\beta_2(\lambda)}|^2 = I_{dc}(\lambda) + I_{ac}(\lambda)cos\Big(\phi(\lambda)\Big) \quad (4.2)$$

where $\phi(\lambda) = \int_0^L \delta\beta(\lambda, z)\ dz$, $I_{SMF}(\lambda) =< E_{SMF}(\lambda), E_{SMF}(\lambda) >$, $I_{ac}(\lambda) = 2I_{SMF}(\lambda)\ A_{\beta_1}(\lambda)\ A_{\beta_2}(\lambda)$ and $I_{dc}(\lambda) = I_{SMF}(\lambda)\ \Big(A^2_{\beta_1}(\lambda) + A^2_{\beta_2}(\lambda)\Big)$, and $I_{ac}(\lambda) \leq I_{dc}(\lambda)$. The quantity $\delta\beta(\lambda, z)$ is the intermodal dispersion as a function of position along the fiber axis, which is assumed constant $(= \delta\beta(\lambda))$ for the pristine fiber. Therefore for the pristine fiber $\int_0^L \delta\beta(\lambda, z)\ dz = L\delta\beta(\lambda)$.

Phase extraction of TMI gives estimates of higher order coefficients of equation 4.1, up to a certain finite number N_s which depends on the signal quality and the noise [78; 79].

$$\delta\beta(\lambda) = \sum_{n=0}^{N_s} \frac{1}{n!}(\lambda - \lambda_0)^n \frac{\partial^n \beta(\lambda_0)}{\partial \lambda^n} + \epsilon(\lambda - \lambda_0) \quad (4.3)$$

where $\epsilon(\lambda - \lambda_0)$ is too noisy for reliable polynomial fitting of degree higher than N_s.

By fitting equation 4.2 to the measured TMI signal, estimate can be obtained for the shape of $L\delta\beta(\lambda)$. However, periodic nature of the cosine function introduces an indeterminacy of integer multiples of 2π in estimating the offset of $L\delta\beta(\lambda)$ from phase unwrapping of TMI.

4.2 Identification of TMI modes

The identification of the modes producing the TMI needs to be confirmed with some mode selective method e.g. far-field imaging [87] or reflection peaks from FBGs [88]. In the FMF used here, identification of the modes which exhibit TMI with GVE at 1.639 μm is done using reflection peaks from FBG written in the fiber.

In general, different collections of resonance peaks can be observed in presence of an FBG in the few-mode fiber, under different excitation conditions:

- In presence of only two modes, one intermodal and two intramodal reflection peaks.
- In presence of multiple modes, a mixture of intramodal and intermodal reflection peaks.
- In presence of a single mode, only one intramodal reflection peak.

Since the resonance peaks occur due to phase matching $2M\pi = \Lambda_{FBG}|\vec{\beta}_x(\lambda_{x,y}) - \vec{\beta}_y(\lambda_{x,y})| = \Lambda_{FBG}|\beta_x(\lambda_{x,y}) + \beta_y(\lambda_{x,y})|$ where M is a natural number, and since for fibers with profiles close to step-index have $b_{LP_{02}}(\lambda) < b_{LP_{21}}(\lambda) < b_{LP_{11}}(\lambda) < b_{LP_{01}}(\lambda)$ (Figure 2.3), formula 2.12 implies that $\beta_{LP_{02}}(\lambda) < \beta_{LP_{21}}(\lambda) < \beta_{LP_{11}}(\lambda) < \beta_{LP_{01}}(\lambda)$. Since for any mode index x, $\beta_x(\lambda)$ is a monotonically decreasing function of λ for fibers with transverse refractive index profiles resembling step-index fibers, amongst all possible reflection peaks in the 4-mode FMF, the extremal peaks must be from LP_{01} and LP_{02}. An FBG with pitch 530 nm in the FMF, written using the Coherent ArF Excimer laser, was excited by scanning a single-mode SM1500 fiber across its cleaved end, using a mechanical alignment stage (schematic shown in figure 4.1). The two excitation conditions are visible in figure 4.2, which corresponded to no offset between the axes of the fibers (plot on bottom) and with offset (plot on top). Since for a centrosymmetric FMF only LP_{01} and LP_{02} should be excited in absence of any offset and there are only three peaks with two of them being extremal (among all possible peaks), the excitation of only LP_{01} and LP_{02} was verified. After splicing, only these three peaks were retained. Thus it was deduced that the TMI in figure 4.4a, exhibited by a spliced SM1500-FMF-SM1500 sample comes from LP_{01} and LP_{02}.

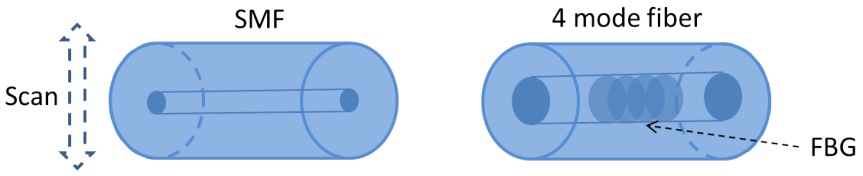

Figure 4.1 – General schematic for exciting modes in a cleaved FMF (containing FBG) using scanning of a cleaved SMF with spectroscopic set up attached on the other end. In general, the strengths of the reflection peaks depend on the mode coupling at the beginning of the few-mode fiber, and therefore has more prominence when (1) an SMF with suitable mode field diameter is spliced, or (2) appropriate gap is put between the neighboring SMF and FMF ends such that diffracted output of the SMF couples into higher-order modes of the FMF

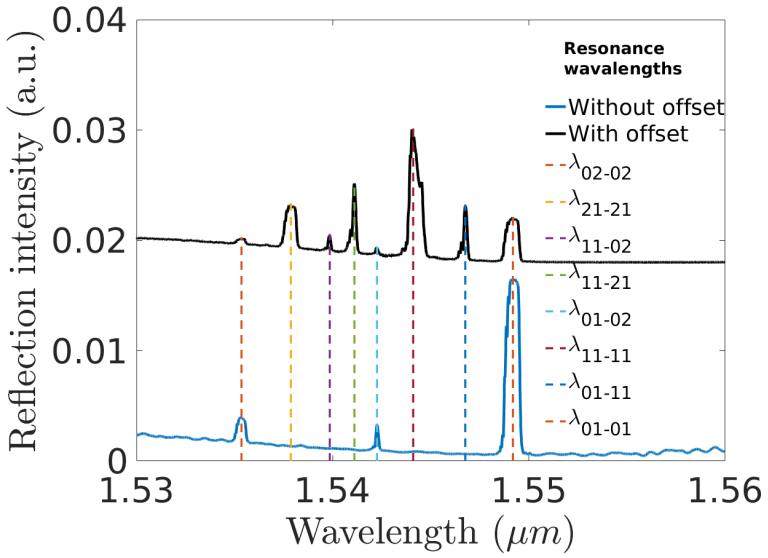

Figure 4.2 – Bragg resonance peaks due to intramodal and intermodal coupling of LP modes from an FBG of pitch 530 nm written inside the FMF, when excited with the scheme in figure 4.1 using an SM1500 SMF. The wavelength of resonance between LP_x and LP_y mode is denominated by λ_{x-y}. The spectrum on top shows the reflection peaks through the SMF, when the end of the SMF was put in contact with the end of the particular FMF sample at a slight offset, such that maximum number of peaks were observed. The spectrum at bottom shows reflection peaks through the SMF when the offset was minimized. After splicing the SMF to the particular FMF sample, three reflection peaks similar to the no-offset condition were observed

4.3 Estimating higher order dispersion coefficients

When the fiber contains only two centrosymmetric modes, for example LP_{01} and LP_{02}, TMI can be generated by splicing two ends of the few-mode fiber (FMF) with single mode fibers of suitable mode field diameter. The overlap of the mode-field diameters of the single-mode and few-mode fibers determine the ratio of $E_{\beta_1}(\lambda)$ and $E_{\beta_2}(\lambda)$ is equation 4.2, which determines the TMI contrast. Maximum contrast occurs when $|E_{\beta_1}| = |E_{\beta_2}|$. In this case, the LP_{01}-LP_{02} TMI is generated by automatic splicing of the FMF ($\Delta n \approx 0.02, a_{core} = 5\ \mu m$) with SM1500 single mode fiber pigtails with mode field diameter $4.2 \mu m$ (Figure 4.3). The splicer used was Fujikura FSM-20CS. Figure 4.4a shows the TMI from a sample of length $869 \pm 0.5 mm$.

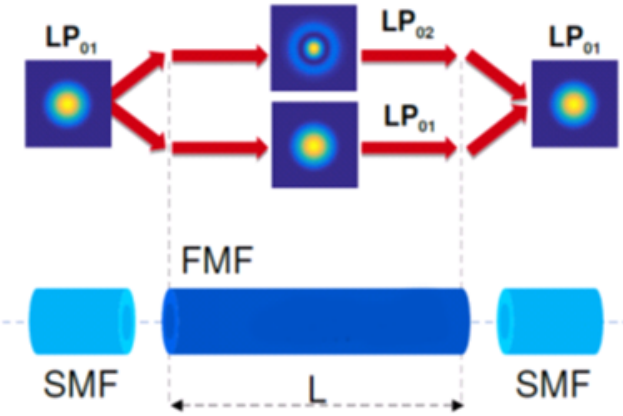

Figure 4.3 – Schematic of TMI sample. The SMF are SM1500, and spliced to FMF on both ends without offset

The TMI shows an oscillating signal of varying period, where the period is decreasing on both sides of a certain wavelength, which is named as the group-velocity equalization wavelength (GVE) (Figure 4.4a). Physically GVE is the wavelength where the group velocities of the two corresponding modes is the same, implying that temporal pulses of the two modes with peak wavelengths at the GVE wavelength travel with the same speed through the fiber. In order to extract the phase of the TMI signal in figure

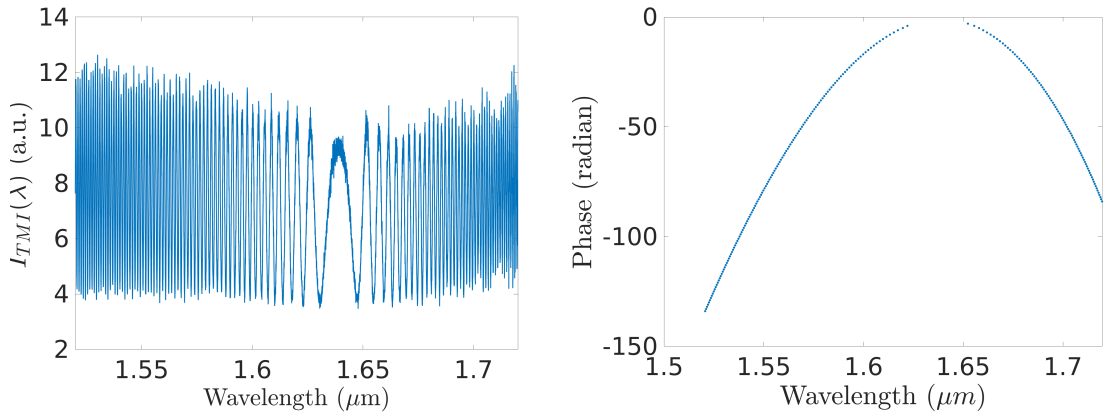

Figure 4.4 – (a) LP_{01}-LP_{02} TMI signal (b)Phase unwrapped signal with unknown offset for 869±0.5 mm few-mode fiber

4.4a, between every neighbouring minimum and maximum, a *zero wavelength* was identified as the wavelengths where the interpolated TMI signal attained the average of its neighbouring extrema. The zero wavelengths were assigned increasing phases $(-N_2\pi - \frac{\pi}{2}, -(N_2-1)\pi - \frac{\pi}{2}, ..., -\frac{5\pi}{2}, -\frac{3\pi}{2})$ with N_2 number of zero wavelengths which are

shorter than GVE wavelength, while for N_1 number of zero wavelengths larger than GVE wavelength were assigned phases in decreasing order $(-\frac{3\pi}{2}, -\frac{5\pi}{2}, ..., -(N_1-1)\pi-\frac{\pi}{2}, -N_1\pi-\frac{\pi}{2})$. Figure 4.4b shows the extracted phase curve which is forced to have $\frac{\partial^2\delta\beta(\lambda)}{\partial\lambda^2} < 0$ in 1.0 μm $\leq \lambda \leq$ 1.6 μm, from previous MC fabrications done in this FMF [29]. The degree N_s of the fitted polynomial $\phi_{fit}(\lambda)$ is determined such that the sum of square errors $\sum_\lambda |\phi_{fit}(\lambda)-\phi(\lambda)|^2$ does not change significantly for $N > N_s$, in comparison to the change in sum of square errors observed for $N \leq N_s$. In the dataset of figure 4.4a, the corresponding fitting degree was $N_s = 4$. The root of the derivative of the fitting polynomial gives the GVE wavelength $\lambda_e : \frac{d\phi_{fit}(\lambda_e)}{d\lambda} = 0, \quad 1.52\mu m < \lambda_e < 1.72\mu m$. The extracted phase is divided with the length and transformed to equation 4.3 with unknown offset $\delta\beta(\lambda_e)$. The extracted coefficients of 4.3 without the offset are presented in table 4.1.

λ_e	$\delta\beta(\lambda_e)$	$\frac{\partial\delta\beta(\lambda_e)}{\partial\lambda}$	$\frac{1}{2}\frac{\partial^2\delta\beta(\lambda_e)}{\partial\lambda^2}$	$\frac{1}{3!}\frac{\partial^3\delta\beta(\lambda_e)}{\partial\lambda^3}$	$\frac{1}{4!}\frac{\partial^4\delta\beta(\lambda_e)}{\partial\lambda^4}$
(μm)	(μm^{-1})	(μm^{-2})	(μm^{-3})	(μm^{-4})	(μm^{-5})
1.639	N.A.	0	-0.0805	-0.388	-2.97
$\pm 5\times10^{-4}$	–	$\pm 5\times10^{-5}$	$\pm 1\times10^{-4}$	$\pm 2\times10^{-3}$	$\pm 8\times10^{-2}$

Table 4.1 – Higher order LP_{01}-LP_{02} intermodal dispersion coefficients from TMI phase unwrapping of FMF with length 869±0.5 mm, with unknown offset

The determination of zero wavelengths become unreliable in presence of high noise (for example when the TMI signal is weak in strength), which can be mitigated by better fitting algorithms to estimate the locations of maxima and minima wavelengths, or for direct normalization of the data to remove $I_{dc}(\lambda)$ and $I_{ac}(\lambda)$ (equation 4.2). Such data treatment became necessary for the experiments reported in the next chapters. In this chapter, phase extraction using zero wavelength is described since it was reported in the same form in conference talks and proceedings [79].

4.4 Determination of offset

In order to estimate the offset of the intermodal dispersion curve of LP_{01}-LP_{02}, a new method was developed which gives estimates for $\delta\beta(\lambda)$ at specific wavelengths by using reflective resonance peaks from fiber Bragg gratings (FBG). In presence of two modes with effective indices $n_{e,1}(\lambda) > n_{e,2}(\lambda)$, an FBG with pitch Λ_{FBG} can exhibit three resonance

peaks $\lambda_{FBG,1} > \lambda_{FBG,2} > \lambda_{FBG,3}$ with the following phase matching conditions:

$$\begin{aligned} \lambda_{FBG,1} &= 2\Lambda_{FBG} \quad n_{e,1}(\lambda_{FBG,1}) \\ \lambda_{FBG,2} &= \Lambda_{FBG} \quad \left(n_{e,1}(\lambda_{FBG,2}) + n_{e,2}(\lambda_{FBG,2})\right) \\ \lambda_{FBG,3} &= 2\Lambda_{FBG} \quad n_{e,2}(\lambda_{FBG,3}) \end{aligned} \tag{4.4}$$

Under the first order approximation that the value of the effective indices of the two modes, $n_{e,1}(\lambda) = n_{e,1}$ and $n_{e,2}(\lambda) = n_{e,2}$ are constant over the wavelength range $[\lambda_{FBG,3}, \lambda_{FBG,1}]$, any pair of equation 4.4 can be solved to get an estimate for $n_{e,1}$ and $n_{e,2}$. From that an estimate of the intermodal dispersion at $\lambda_{FBG,2}$ can be obtained:

$$\delta\beta_{1-2}(\lambda_{FBG,2}) \approx 2\pi \frac{(n_{e,1} - n_{e,2})}{\lambda_{FBG,2}} \tag{4.5}$$

For an FBG of pitch 530 nm made with a phase mask imprint from the side with Coherent ArF excimer laser (table 3.3), the resonance peaks observed for LP_{01} and LP_{02} (Figure 4.2) are presented in table 4.2. Using these peaks, three estimates of

$\lambda_{FBG,3} = \lambda_{02-02}$ (μm)	$\lambda_{FBG,2} = \lambda_{01-02}$ (μm)	$\lambda_{FBG,1} = \lambda_{01-01}$ (μm)
1.5353	1.5422	1.5491
$n_{e,LP_{01}}$	$\frac{n_{e,LP_{01}} + n_{e,LP_{02}}}{2}$	$n_{e,LP_{02}}$
1.4484 ± 0.0002	1.4549 ± 0.0002	1.4614 ± 0.0002

Table 4.2 – Effective index estimates of LP_{01} and LP_{02} modes, at the intermodal resonance wavelength of an FBG with pitch 530 nm. The nomenclature $\lambda_{FBG,x}$ corresponds to equations 4.4-4.5 and the nomenclature λ_{x-y} corresponds to figure 4.2

$n_{e,LP_{01}} - n_{e,LP_{02}} = \{0.00650, 0.00655, 0.00610\}$ were obtained, with relative errors $\pm 4 \times 10^{-4}$. This gives the final estimate $\delta\beta_{01-02}(\lambda_{01-02}) = 0.0531 \pm 0.0004 \mu m^{-1}$. According to this estimate, when the pitch used to fabricate an MC with weak index perturbation is $\frac{2\pi}{\delta\beta_{01-02}(\lambda_{01-02})} = 118.3 \pm 0.9 \mu$m, the resonance will happen at 1.5422 μm wavelength.

4.4.1 Limitations

Before moving on to making MCs with this estimate, the validity of this method should be verified with simulation of the well-understood step-index model. The solid curves in figure 4.5 shows the effective indices for LP_{01} and LP_{02}, and their average for a step-index fiber with 5 μm radius and 14 % GeO_2 concentration at the core, calculated using formula 2.12 and the $V-b$ diagram for step-index fibers (Figure 2.3). In the presence of an FBG with pitch Λ_{FBG}, the intersection of these curves with $\frac{\lambda}{2\Lambda_{FBG}}$ gives the corresponding resonance wavelengths.

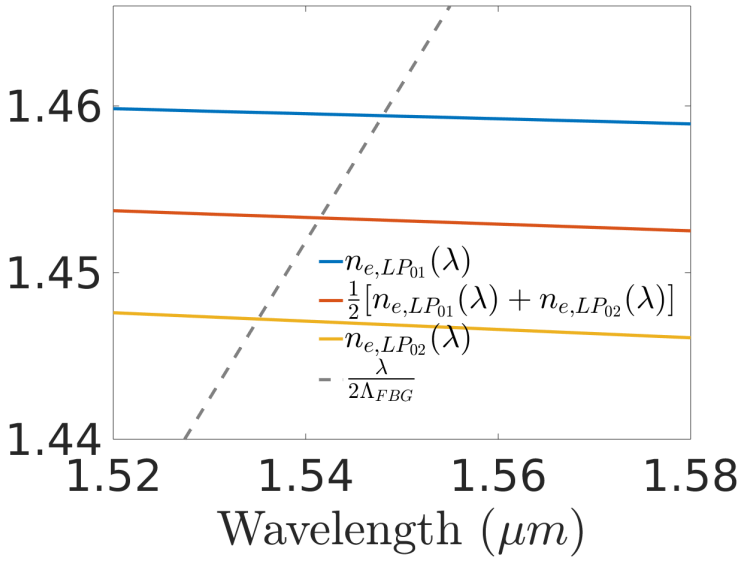

Figure 4.5 – Simulated effective indices for step-index fiber with radius 5.0 μm and 14 % GeO_2 concentration in the core (Solid curves). The dashed gray line represents $\frac{\lambda}{2\Lambda_{FBG}}$. The intersection of the dashed line with the solid curves give the values of the resonance wavelengths for an FBG of pitch $\Lambda_{FBG} = 530.15$ nm

In figure 4.5 three FBG resonance wavelengths are {1.5355 μm, 1.5422 μm, 1.5488 μm}, which gives an estimate of $\delta\beta(1.5422\ \mu\text{m}) = 0.0511\ \mu m^{-1}$. According to the simulation results illustrated in figure 4.6, the exact value of the intermodal dispersion at the peak wavelength is $\beta_{01}(1.5422\ \mu\text{m}) - \beta_{02}(1.5422\ \mu\text{m}) = 0.0508\ \mu m^{-1}$. Compared to the exact value, using the new method gives a relative error of 0.6 %, which is a good starting point for MC and TMI studies.

Regarding the technical aspect of attaining grating resonance at desired wavelength, FBGs are much more robust compared to MC, since slight changes in FBG pitch Λ_{FBG} and correspondingly the wavevector $\frac{2\pi}{\Lambda_{FBG}}$ still match the dispersion $\beta(\lambda)$ of individual modes close to the original resonance wavelength. On the other hand, the magnitude and curvature of $\delta\beta(\lambda)$ is quite smaller in comparison, which causes hundreds on nm of shift in resonance wavelength for few microns of change in the MC pitch, the sensitivity of which

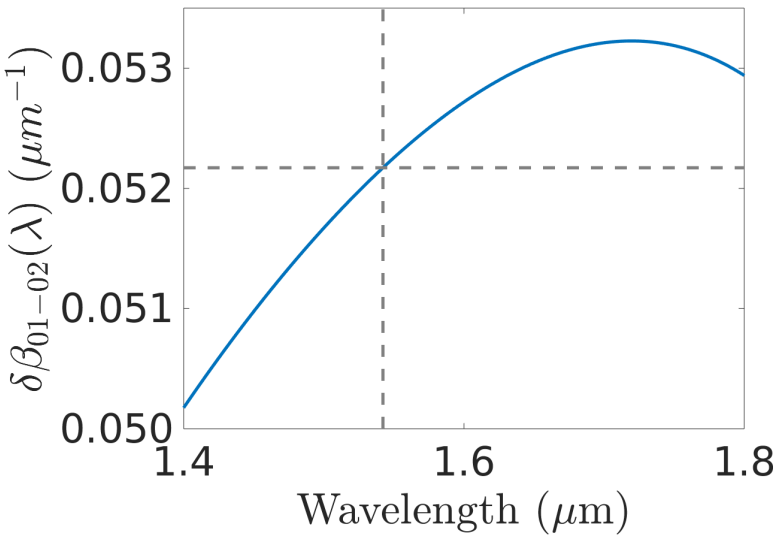

Figure 4.6 – Simulated difference in propagation constants of LP_{01} and LP_{02} modes for a step-index fiber of radius 5.0 μm and 14 % GeO_2 concentration in the core. According to the simulation, the exact value of $\delta\beta(1.5422\ \mu m) = 0.0508\ \mu m^{-1}$

has been calculated in the next section for the MC resonance between LP_{01} and LP_{02} in this FMF. Permanent FBGs can be reliably made using phase mask side-illumination technique, while temporary FBGs can be made using Brillouin gratings [89; 90]. The guess of $\delta\beta(\lambda)$ can be used as the starting point for the iteration of making MCs, with further iterations with a few μm on each side of the guess.

The simulation can be used to compare the estimation error for the offset of $\delta\beta(\lambda)$ with the higher-order error in the assumption that the effective index is constant over the range defined by the intramodal resonance wavelengths of the two corresponding modes.

As illustrated in figure 4.7, $\delta n_e(\lambda) = \lambda\frac{\delta\beta(\lambda)}{2\pi}$ for LP_{01} and LP_{02} varies between 0.0124-0.0125 in the wavelength range of 1.542±0.007 μm, which corresponds to a relative error of 0.5 %. For the simulation, the relative error in estimating the value of $\delta\beta(\lambda = 1.542\mu\text{m})$ using the novel method is 0.6 %.

In addition to such an expected approximation error inherent to this novel method, it is also known that the intermodal dispersion experienced by an MC differs from that of a pristine fiber due to change in the local intermodal dispersion due to perturbation [33; 34]. A conservative relative error estimate of 2 % was therefore assigned in the determination of the pitch for a desired resonance wavelength, encompassing the error of the novel method with FBG peaks and the change in $\delta\beta(\lambda)$ due to perturbation.

In section 4.4, an estimate of $\delta\beta(\lambda = 1.5422\ \mu\text{m})$ was obtained from experimental mea-

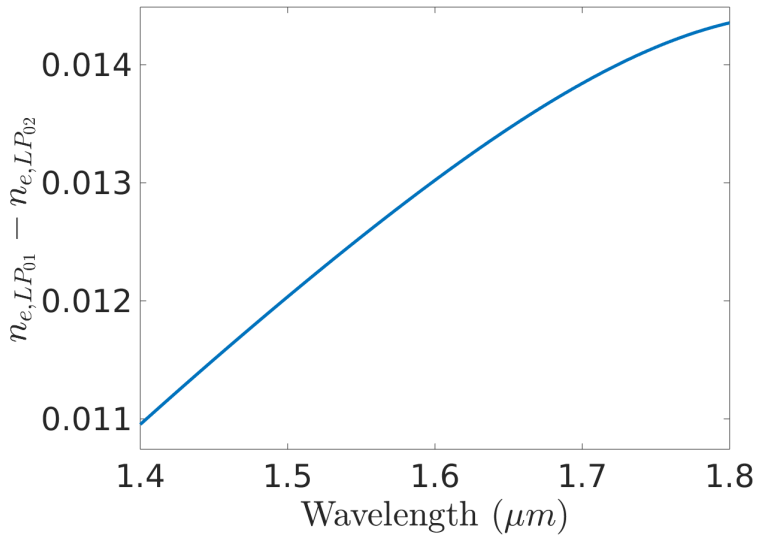

Figure 4.7 – Effective index difference of LP_{01} and LP_{02} for the simulated step-index fiber in figure 4.5

surements of FBG reflections peaks. Using this estimate gives $\Lambda_{MC} = \frac{2\pi}{\delta\beta(\lambda)} = 118.3$ μm at $\lambda = 1.5422$ μm, a 2 % error on which implies a range of $\Lambda_{MC} = (116.0, 120.7)$ μm for resonance at $\lambda = 1.5422$ μm. Assuming an exact value of $\delta\beta(\lambda = 1.5422\ \mu\text{m})$, this range exceeds the variation of $\Lambda_{MC}(\lambda) = \frac{2\pi}{\delta\beta(\lambda)}$ due to the measured shape of $\delta\beta(\lambda)$ (table 4.1) over the whole wavelength range of $(1.46, 1.62)$ μm (See sections 4.5 and 4.6). Therefore it does not make sense to illustrate a graph for $\Lambda_{MC}(\lambda)$ with realistic errors at this stage. Generally it might be more useful to utilize more precise estimates of the offset of $\delta\beta(\lambda)$ using non-permanent acousto-optic [54] or Brillouin gratings [89; 90; 91] with weak index perturbations, if available.

4.5 Sensitivity of MC resonance wavelength with respect to pitch

Given the estimate of $\delta\beta(\lambda)$, the sensitivity of the MC resonance wavelength λ_{MC} with changes in the MC pitch Λ_{MC} can be understood by taking differentials along the contour line of the phase $\phi(\lambda, \Lambda) = \Lambda_{MC}\delta\beta(\lambda)$ at the phase-matching value of $2\pi = \phi(\lambda_{MC}, \Lambda) = \Lambda_{MC}\delta\beta(\lambda_{MC})$, as a function of wavelength and pitch [33].

$$\begin{aligned}
\frac{d\phi(\lambda,\Lambda)}{d\Lambda_{MC}} &= \frac{\partial\phi(\lambda,\Lambda)}{\partial\Lambda_{MC}} + \frac{d\lambda_{MC}}{d\Lambda_{MC}}\frac{\partial\phi(\lambda,\Lambda)}{\partial\lambda}\Big|_{\lambda=\lambda_{MC}} = 0 \\
&\implies \delta\beta(\lambda_{MC}) + \frac{d\lambda_{MC}}{d\Lambda_{MC}}\Lambda_{MC}\frac{\partial\delta\beta(\lambda)}{\partial\lambda}\Big|_{\lambda=\lambda_{MC}} = 0 \\
&\implies \delta\beta(\lambda_{MC}) + \frac{d\lambda_{MC}}{d\Lambda_{MC}}\frac{2\pi}{\delta\beta(\lambda_{MC})}\frac{\partial\delta\beta(\lambda)}{\partial\lambda}\Big|_{\lambda=\lambda_{MC}} = 0 \\
&\implies \frac{d\lambda_{MC}}{d\Lambda_{MC}} = -\frac{1}{2\pi}\frac{\delta\beta(\lambda_{MC})^2}{\frac{\partial\delta\beta(\lambda)}{\partial\lambda}|_{\lambda=\lambda_{MC}}}
\end{aligned} \tag{4.6}$$

Figure 4.8 shows the sensitivity of $\frac{d\lambda_{MC}}{d\Lambda_{MC}}$ for resonance between LP_{01} and LP_{02} in the FMF as a function of resonance wavelength λ_{MC}, which has been calculated using equation 4.6 and the estimates from tables 4.1 and 4.2. In the whole wavelength range of 1.5 μm to 1.7 μm, $|\frac{d\lambda_{MC}}{d\Lambda_{MC}}| > 0.05$. This implies that a change of 1 μm in pitch $\Lambda_{MC} = \frac{2\pi}{\delta\beta(\lambda_{MC})}$ will lead to at least 50 nm shift in resonance wavelength λ_{MC}. $|\frac{d\lambda_{MC}}{d\Lambda_{MC}}|$ also becomes bigger without any bound as the resonance wavelength approaches the GVE wavelength.

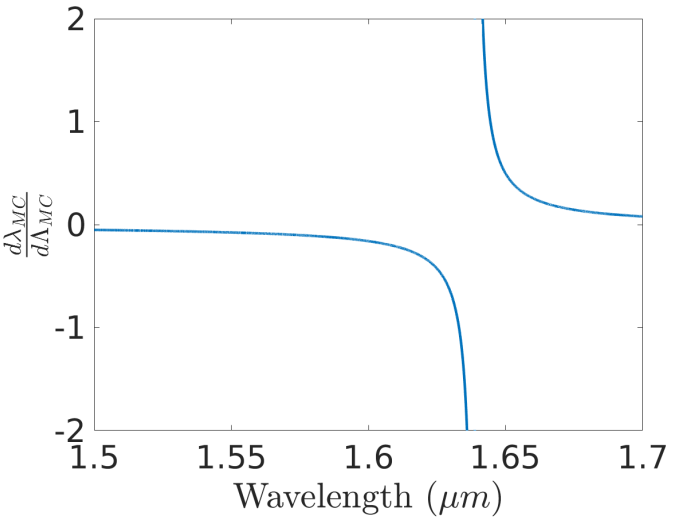

Figure 4.8 – The calculated sensitivity of LP_{01}-LP_{02} MC resonance wavelength with change in the MC pitch for the FMF, as a function of the resonance wavelength. $|\frac{d\lambda_{MC}}{d\Lambda_{MC}}| > 0.05$ in the whole wavelength range of 1.5 μm to 1.7 μm, and becomes bigger as the resonance wavelength gets closer to the GVE wavelength

4.6 Sensitivity of MC resonance wavelength with respect to offset

Another sensitivity that can be estimated only with the knowledge of the shape of $\delta\beta(\lambda)$ (4.1), without knowing any material parameters or the exact value of the offset of $\delta\beta(\lambda)$, is the sensitivity of the resonance wavelength with respect to an error in determining the offset.

For some pitch Λ whose exact value is unimportant for this analysis, the exact $\delta\beta(\lambda)$ gives a resonance wavelength at some λ less than GVE wavelength given by $\delta\beta(\lambda) = \frac{2\pi}{\Lambda_{MC}}$. If another estimate $\delta\beta^*(\lambda)$ has been made due to an added error of $\Delta > 0$ in estimating the offset, implying $\delta\beta^*(\lambda) = \delta\beta(\lambda) + \Delta$, the resonance would be guessed at some other wavelength $\lambda - \Delta\lambda,\ \Delta\lambda > 0$ by $\delta\beta^*(\lambda - \Delta\lambda) = \frac{2\pi}{\Lambda_{MC}}$. The phase matching relation would then give

$$
\begin{aligned}
&\delta\beta^*(\lambda) = \delta\beta^*(\lambda-\Delta\lambda) + \Delta\lambda\frac{\partial\delta\beta^*(\lambda)}{\partial\lambda} + \frac{(\Delta\lambda)^2}{2}\frac{\partial^2\delta\beta^*(\lambda')}{\partial\lambda^2} && \text{...for some } \lambda-\Delta\lambda < \lambda' < \lambda \\
&\implies \delta\beta^*(\lambda) = \delta\beta^*(\lambda-\Delta\lambda) + \Delta\lambda\frac{\partial\delta\beta(\lambda)}{\partial\lambda} + \frac{(\Delta\lambda)^2}{2}\frac{\partial^2\delta\beta(\lambda')}{\partial\lambda^2} && \text{...since } \delta\beta^*(\lambda) = \delta\beta(\lambda) + \Delta \\
&\implies \delta\beta(\lambda) + \Delta = \delta\beta^*(\lambda-\Delta\lambda) + \Delta\lambda\frac{\partial\delta\beta(\lambda)}{\partial\lambda} + \frac{(\Delta\lambda)^2}{2}\frac{\partial^2\delta\beta(\lambda')}{\partial\lambda^2} && \text{...replacing } \delta\beta^*(\lambda) = \delta\beta(\lambda) + \Delta \\
&\implies \Delta = \Delta\lambda\frac{\partial\delta\beta(\lambda)}{\partial\lambda} + \frac{(\Delta\lambda)^2}{2}\frac{\partial^2\delta\beta(\lambda')}{\partial\lambda^2} && \text{...since } \delta\beta^*(\lambda-\Delta\lambda) = \delta\beta(\lambda) = \frac{2\pi}{\Lambda_{MC}} \\
&\implies \Delta \le \Delta\lambda\frac{\partial\delta\beta(\lambda)}{\partial\lambda} \implies \Delta\lambda \ge \frac{\Delta}{\frac{\partial\delta\beta(\lambda)}{\partial\lambda}} && \text{...since } \frac{\partial^2\delta\beta(\lambda)}{\partial\lambda^2} < 0 \text{ and } \frac{\partial\delta\beta(\lambda)}{\partial\lambda} > 0 \\
&\implies \left|\frac{\Delta\lambda}{\lambda}\right| \ge \left|\frac{\Delta}{\lambda\frac{\partial\delta\beta(\lambda)}{\partial\lambda}}\right| = \left|\frac{\delta\beta(\lambda)}{\lambda\frac{\partial\delta\beta(\lambda)}{\partial\lambda}}\right| \times \left|\frac{\Delta}{\delta\beta(\lambda)}\right| && (4.7)
\end{aligned}
$$

For 1.5 μm$\le \lambda \le$ to 1.7 μm, the quantity $\left|\frac{1}{\lambda\frac{\partial\delta\beta(\lambda)}{\partial\lambda}}\right| > 50\ \mu m$, which implies that an error of $\pm\ 5\times10^{-4}\ \mu\text{m}^{-1}$ in determining the offset of $\delta\beta(\lambda)$ (corresponding to approximately $\pm$ 1 % error for LP_{01}-LP_{02} mode pair) will lead to at least 25 nm error in determining the resonance wavelength for some pitch. The absolute value of the sensitivity of the resonance wavelength with determination error or changes in value of the offset of $\delta\beta(\lambda)$ also increases in an unbounded manner as the resonance wavelength gets closer to the GVE wavelength.

4.7 Conclusion

In this chapter a new method for determining the intermodal dispersion coefficients of a few mode fiber, from combination of TMI phase extraction and multiple resonance peaks

from FBG written in the FMF is presented. The modes with highest and lowest effective indices can be identified from the reflection peaks, using differential excitation of the modes by scanning a single mode fiber across the cleaved end of the FMF. Using this method the TMI was ascertained to be from LP_{01} and LP_{02}. The determined intermodal dispersion is used for the studies of different perturbations on TMI, and as starting guesses for making mode converters, which are presented in the following chapters.

5 Effect of perturbations on two-mode interference

5.1 Introduction

Modal interference in optical fibers has been studied extensively for use in devices. For example, multimode interference fringes have been used as temperature and strain sensors [84; 92; 93], temperature and strain differentiation [94], bending sensors [95], refractive index sensors [92] etc. The two-mode interference (TMI) fringes shift when any parameter change induces a change of intermodal phase between the corresponding modes [84]. It is thus important to know the response of the intermodal dispersion $\delta\beta(\lambda)$ with respect to these parameters [76; 96]. In this chapter experiments on three different parameter estimates is presented-

- Subsection 5.2.1 presents a method to estimate $\frac{\partial\delta\beta(\lambda)}{\partial T}$ from the few-mode fiber length, phase shifts due to temperature and the intermodal dispersion curve of the unperturbed fiber (Estimated in chapter 4). This has very recently been reported also by [76].
- Subsection 5.2.2 presents a method to estimate $\frac{\partial\delta\beta(\lambda)}{\partial\epsilon}$ from the few-mode fiber length, phase shift due to strain and the intermodal dispersion curve (Estimated in chapter 4).
- Subsection 5.2.3 presents a method based on similar principles for estimating the change in $\delta\beta(\lambda)$ with laser fluence, under the condition that the laser spot is scanned at constant speed over the whole length of the FMF. Enforcing such scanning implied that every spot in the FMF was equally irradiated.

Regarding sensing, the following modalities of TMI have been explored-

- Relative wavelength shift of both TMI fringes and MC resonance are described by the same equations, with the only different term being the intermodal dispersion of the FMF and the MC. The intermodal dispersion of an MC converges to the intermodal dispersion of the FMF when the index perturbation is made smaller. The relative shift of TMI fringes and MC resonance wavelength is experimentally compared in 5.2.1, along with the comparison of relative wavelength shifts of FBG and GVE wavelength.
- The group-velocity equalization (GVE) wavelength has also been used in sensing: e.g. in temperature sensing [84], temperature and strain differentiation [94], refractive index sensing with etched FMF [92], and bending characterization of an FMF [96]. Although mathematical explanations exist for effects of temperature and strain on two-mode interference, there is no simple model describing the sensitivity of GVE wavelength to temperature, strain and photoinduced change in core refractive index. Section 5.3 presents a simple model for these sensitivities and experimentally verifies the model for temperature and strain (subsection 5.3.1 and 5.3.2).
- Subsection 5.3.3 presents a novel and precise method to measure the change in refractive index of the photosensitive core due to UV laser exposure, under the assumption that the change in the *shape* of the refractive index profile due to the perturbation is insufficient to cause significant change in the V-b diagram for that profile shape. Under this assumption, the relative shift in the V-number corresponding to the GVE wavelength is negligible compared to the relative changes of the GVE wavelength and change in refractive indices. This method allows the estimate of small UV-induced refractive index changes of the photosensitive core, without the need of detailed calculations of the $V-b$ diagram of the fiber [97].
- The last subsection 5.4 illustrates investigations on simultaneous temperature and strain determination, which is a highly studied topic [98; 99; 100; 101; 102; 94; 103]. The capability of using the combination of GVE wavelength and FBG resonance peak for temperature and strain differentiation was explored. A complete error analysis was done for this method, with care taken to consider every algorithmic step from the measurement to the estimation.

5.2 Effect of perturbation on fringes

The TMI fringes are characterized by constant phase $\phi(\lambda_m(X), X)$, with respect to the change in a parameter X (e.g temperature, strain or UV laser exposure). The change in a fringe wavelength due to a change in X corresponds to a locus on the contour curve for $(\lambda, X) : \phi(\lambda_m, X) = K_m$ in the (λ, X) landscape, where K_m is a constant dependent on the natural number m. Since $\phi(\lambda, X)$ is smooth with respect to both the

parameters, the magnitude of the relative shifts in $(\lambda_m(X), X)$ is related by multi-variable calculus. Following a fringe wavelength corresponds to keeping the phase constant, i.e. $\Delta\phi(\lambda_m(X), X) = 0$ [104]:

$$\frac{d\phi_m}{dX} = \frac{\partial\phi(\lambda_{m,0})}{\partial X} + \frac{d\lambda_m}{dX}\frac{\partial\phi(\lambda)}{\partial\lambda}\Big|_{\lambda=\lambda_{m,0}} = 0 \tag{5.1}$$

where $\lambda_{m,0} = \lambda_m(\Delta X = 0)$. Equation 5.1 provides an estimate for the shift of λ_m

$$\begin{aligned}
\frac{d\lambda_m}{dX} &= -\frac{\partial\phi(\lambda_{m,0})}{\partial X} \Big/ \frac{\partial\phi(\lambda)}{\partial\lambda}|_{\lambda=\lambda_{m,0}} && \text{... Rearranging equation 5.1} \\
&= \frac{1}{\phi(\lambda_{m,0})}\frac{\partial\phi(\lambda_{m,0})}{\partial X} \Big/ \Big[-\frac{1}{\phi(\lambda_{m,0})}\frac{\partial\phi(\lambda)}{\partial\lambda}|_{\lambda=\lambda_{m,0}}\Big] \\
&= \frac{1}{\phi(\lambda_{m,0})}\frac{\partial\phi(\lambda_{m,0})}{\partial X} \Big/ \Big[-\frac{1}{\delta\beta(\lambda_{m,0})}\frac{\partial\delta\beta(\lambda)}{\partial\lambda}|_{\lambda=\lambda_{m,0}}\Big] && \text{... Since } L \text{ is independent of } \lambda \\
&= \frac{\lambda_{m,0}}{\phi(\lambda_{m,0})}\frac{\partial\phi(\lambda_{m,0})}{\partial X} \Big/ \Big[-\frac{\lambda_{m,0}}{\delta\beta(\lambda_{m,0})}\frac{\partial\delta\beta(\lambda)}{\partial\lambda}|_{\lambda=\lambda_{m,0}}\Big] \\
&= \gamma(\lambda_{m,0})\frac{\lambda_{m,0}}{\phi(\lambda_{m,0})}\frac{\partial\phi(\lambda_{m,0})}{\partial X} && \text{... Renaming } -(\frac{\lambda_{m,0}}{\delta\beta(\lambda_{m,0})}\frac{\partial\delta\beta(\lambda)}{\partial\lambda}|_{\lambda=\lambda_{m,0}})^{-1}
\end{aligned} \tag{5.2}$$

where $\gamma(\lambda)$ is defined as $\gamma(\lambda) = -\Big(\frac{\lambda}{\delta\beta(\lambda)}\frac{\partial\delta\beta(\lambda)}{\partial\lambda}\Big)^{-1}$, which is a completely waveguide-dispersion dependent term. Once $\delta\beta(\lambda)$ has been estimated, $\gamma(\lambda)$ can directly be calculated. For X which uniformly affects the whole length of the FMF, the relative change in phase $\frac{1}{\phi(\lambda_{m,0})}\frac{\partial\phi(\lambda_{m,0})}{\partial X}$ can be written in terms of relative changes of FMF length L and $\delta\beta(\lambda)$ with X [1]

$$\frac{1}{\phi(\lambda_{m,0})}\frac{\partial\phi(\lambda_{m,0})}{\partial X} = \begin{cases} \Big[\alpha + \frac{1}{\delta\beta(\lambda_{m,0})}\frac{\partial\delta\beta(\lambda_{m,0})}{\partial T}\Big] = \Gamma_T(\lambda_{m,0}) & \text{for } X = T \text{ (Temperature)} \\ \Big[1 + \frac{1}{\delta\beta(\lambda_{m,0})}\frac{\partial\delta\beta(\lambda_{m,0})}{\partial\epsilon}\Big] = \Gamma_\epsilon(\lambda_{m,0}) & \text{for } X = \epsilon \text{ (Strain)} \\ \Big[\frac{1}{\delta\beta(\lambda_{m,0})}\frac{\partial\delta\beta(\lambda_{m,0})}{\partial F}\Big] = \Gamma_F(\lambda_{m,0}) & \text{for } X = F \text{ (Laser fluence)} \end{cases} \tag{5.3}$$

where strain is defined as $\epsilon = \frac{\Delta L}{L}$, and laser fluence F is the product of average intensity and exposure time. The equation involving fluence holds when the full FMF sample has been uniformly irradiated, for example by scanning a laser spot with fixed intensity across the full length of the FMF with constant speed.

[1] For local perturbations as well, equation 5.2 still holds

For any perturbation X which uniformly affects the whole length of the fiber, the fringe wavelength for a fixed phase (fixed m) exhibits the same shift for any length of the fiber. The length dependence of fringe wavelength shift arises implicitly; for fixed m, $|\lambda_m(L_1) - \lambda_e| < |\lambda_m(L_2) - \lambda_e|$ for $L_1 < L_2$. Normalizing with the fringe wavelength removes the implicit dependency on both length and m [105]. The definition of $\Gamma_X(\lambda) = \frac{1}{\phi(\lambda)} \frac{\partial \phi(\lambda)}{\partial X}$ is motivated from [105], in which similar term was defined for LPG resonance sensitivity. The quantity $\alpha = \frac{1}{L} \frac{dL}{dT}$ is the thermal expansion coefficient of fused silica, with a value of 0.6×10^{-6} °C^{-1} [106]. Although germano-silicate glass has doping dependent thermal expansion coefficient [60], since the cladding occupies an ≈ 155 times more area than the core in a cross-section of the FMF, the thermal expansion of the fused silica cladding dominates compared to the thermal expansion of the germano-silicate core. Therefore the value of fused silica was used for α. The dispersion-only term $\gamma(\lambda)$ has a singularity at the GVE wavelength $\lambda = \lambda_e$ and changes sign at λ_e. Since $\frac{1}{L} \frac{\partial L}{\partial X} + \frac{1}{\delta\beta(\lambda_{m,0})} \frac{\partial \delta\beta(\lambda_{m,0})}{\partial X}$ is positive for strain,temperature change and uniform laser exposure across the core of the FMF, the following are observed, as expected from previous studies [84; 93; 76]

- Sensitivity increases as the fringe wavelength gets closer to λ_e.

- The fringes move in opposite directions on two sides of λ_e, for any perturbation.

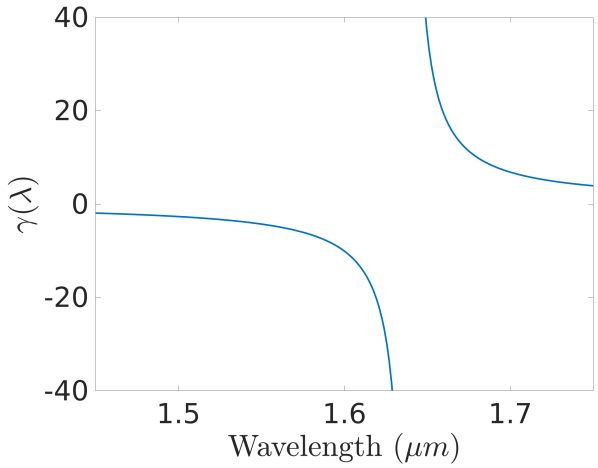

Figure 5.1 – Calculated $\gamma(\lambda)$ based on the estimate of $\delta\beta(\lambda)$ in chapter 4

The novelty here is better estimate of $\gamma(\lambda)$, due to accurate estimate of $\delta\beta(\lambda)$ using the method described in chapter 4. This allows precise estimates for $\frac{\partial \delta\beta(\lambda_{m,0})}{\partial T}$ [76] and

$\frac{\partial\delta\beta(\lambda_{m,0})}{\partial\epsilon}$, following from the differential formula of $\phi(\lambda)$:

$$\frac{d\phi(\lambda_{m,0})}{dX} = \left(L\frac{\partial\delta\beta(\lambda_{m,0})}{\partial X} + \delta\beta(\lambda_{m,0})\frac{\partial L}{\partial X}\right) = 0 \implies$$

$$\frac{\partial\delta\beta(\lambda_{m,0})}{\partial T} = \frac{1}{L}\frac{\partial\phi(\lambda_{m,0})}{\partial T} - \alpha\ \delta\beta(\lambda_{m,0}) \quad \text{for } X = T \tag{5.4}$$

$$\frac{\partial\delta\beta(\lambda_{m,0})}{\partial\epsilon} = \frac{1}{L}\frac{\partial\phi(\lambda_{m,0})}{\partial\epsilon} - \quad \delta\beta(\lambda_{m,0}) \quad \text{for } X = \epsilon \tag{5.5}$$

.

5.2.1 Temperature response of TMI

The temperature response of TMI was studied by slow and gradual cooldown using a water bath described in figure 5.2a. The TMI sample was loosely wrapped around a hollow aluminum cylinder (radius 9 cm, height 27 cm) with holding hooks and one closed face, without tension or tight winding to avoid strain from expansion of the aluminum cylinder. The aim was to provide uniform temperature all over the fiber, avoiding both radial and vertical gradients. The sample holder was suspended on an aluminum cylinder in the middle of a glass beaker of 5 L volume (diameter 20 cm). The beaker was kept inside a styrofoam box. The beaker was filled with boiling water, followed by closing the styrofoam box for reducing the cooling rate. Two K-type thermocouples were introduced through holes on top of the styrofoam box. One of the thermocouples measured the temperature at the closed planar face of the aluminum cylinder, while another flexible thermocouple was wound around the aluminum cylinder before wounding the fiber. The difference between the readings of the two thermocouples provided an estimate of the radial temperature gradient (Figure 5.2b). Pigtails from the TMI sample were passed through small holes in the cover of the styrofoam box. Spectra were excited using supercontinuum SuperK Extreme source and recorded using Ando OSA 6317Q spectrometer. OSA parameters were set to the following- resolution of 50 pm, sensitivity setting of MID against the other available settings NORM, HIGH1 and HIGH2, 10000 data points and 200 nm span centered at 1600 nm. Each spectrum took approximately 20 seconds to record in these settings, while the NORM setting gave very noisy measurements and HIGH1 and HIGH2 settings took more than 3 min to record a single spectrum. Fitting a 4th order polynomial through the logged thermocouple temperature gives a maximum rate of change of temperature $\frac{dT}{dt} = 1.1 \times 10^{-3}$ °Cs^{-1}.Thus the fastest rate at which a cooldown of 0.1°C (resolution of the thermocouples) can happen is approximately 91 s. A 20 s time resolution of the spectrum acquisition in the MID setting thus gave a temperature resolution < 0.22 °C, whereas the long acquisition times of the HIGH1 and HIGH2 settings gave <1.98 °C resolution. Since accurate phase extraction was possible in the MID setting, it was deemed appropriate for the measurements irrespective of the better spectral quality in HIGH1 and HIGH2 settings.

For all the TMI measurements reported in this chapter, the TMI was excited using centrosymmetric splicing of SM1500 on both sides of the FMF piece, as has been described in chapter 4.

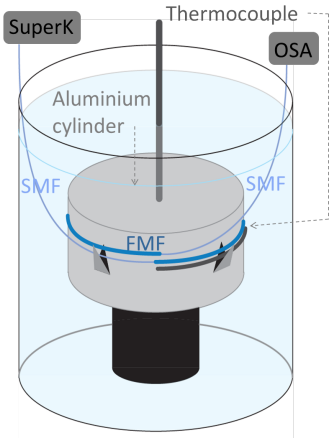

(a) Water bath

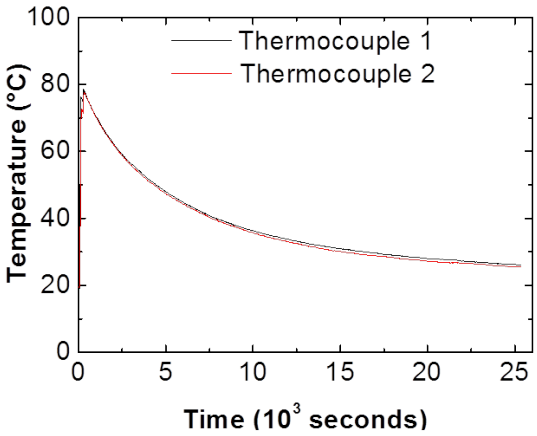

(b) Temperature measured by different thermocouples

Figure 5.2 – (a) Cooldown setup and (b) temperature decay of the bath with time, measured from two different thermocouples; one placed at the center of FMF coils, another placed right next to the FMF by concentric coiling. The two thermocouples showed slightly different temperatures, and the thermocouple right next to the FMF was used to get the temperature experienced by the FMF

The fringes move away from λ_e with increasing temperature (Figure 5.3), as expected from the sign arguments in equation 5.2. λ_e increases with increasing temperature. The shift is negligible compared to neighboring fringes: 1.6337 μm$\leq \lambda_e \leq$ 1.6349 μm for 25.3 °C<T<53.7 °C.

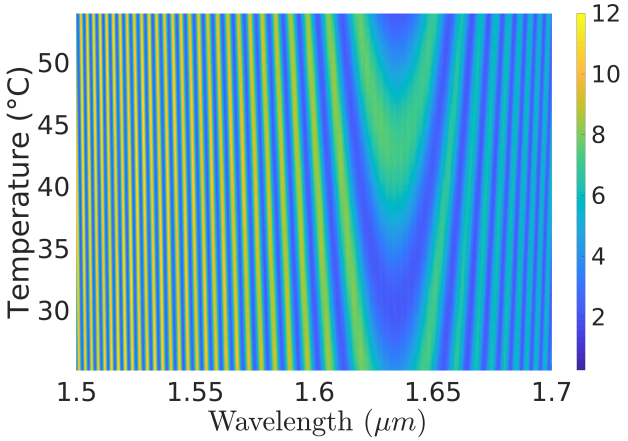

Figure 5.3 – 3D plot of measured spectral evolution of TMI with temperature, where the spectral intensity (a.u.) is represented by color

From background and amplitude normalized signal of the last frame (lowest temperature), wavelength values of maxima corresponding to phases of $2M\pi : \ M \in \mathbb{Z}$ were extracted. Due to small changes in temperature, the extrema wavelengths can be continuously tracked from the last frame to the first frame recorded during cooldown (Figure 5.3). The relative fringe shifts appear to be linear (Figure 5.4). The same can be done for minima wavelengths, corresponding to $\phi_M = 2M\pi \pm \pi : \ M \in \mathbb{Z}$

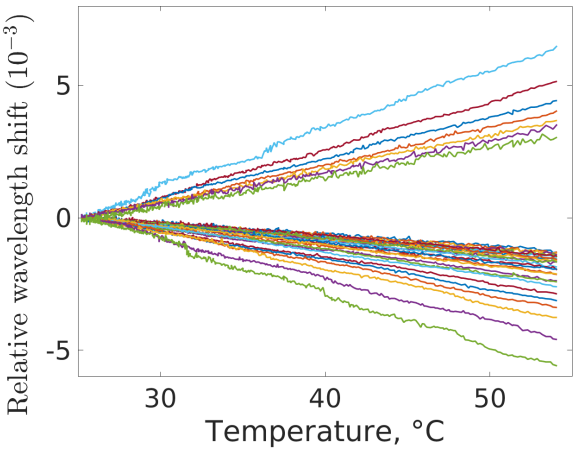

Figure 5.4 – Measured relative wavelength shifts of spectral maxima in figure 5.3 with temperature, which indicate linear shift for each measured maxima wavelength

The lines which are increasing with temperature correspond to maxima wavelengths larger than λ_e, whereas the lines which are decreasing with temperature correspond to maxima wavelengths smaller than λ_e. On both sides of λ_e, maxima wavelengths which are closer to λ_e have larger absolute value of their linear slopes. Due to the linear shift of the tracked fringes in figure 5.4, fitting straight lines to the relative wavelength shift gives an estimate of $\frac{1}{\lambda_{m,0}} \frac{d\lambda_m}{dT}$ for the tracked extrema wavelengths. These estimates are illustrated in figure 5.5. As expected from the singularity in $\gamma(\lambda)$ in equation 5.3, $\frac{1}{\lambda_{m,0}} \frac{d\lambda_m}{dT}$ has a singularity at $\lambda_e(\Delta T = 0)$.

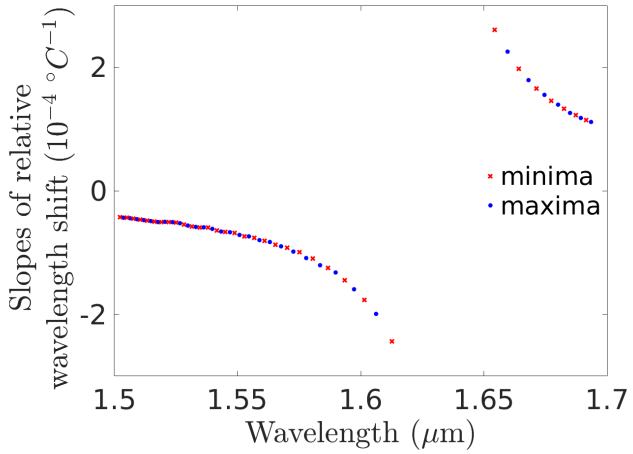

Figure 5.5 – Extracted linear slopes of relative wavelength shift of the extrema. These represent the left-hand side of the equation 5.3, for temperature

Each spectrum was fitted with equation 4.2, by taking the extracted wavelengths and values of the extrema, together with the assigned phases, as guesses. The extracted phase as function of temperature, $\phi(\lambda, T)$ was fitted with a two-dimensional polynomial which is linear in temperature and of fourth order in wavelength. Applying equation 5.4 on the fitted phase, along with using the estimate of $\delta\beta(\lambda)$ from chapter 4, the relative change in intermodal dispersion with temperature is obtained, which is plotted in figure 5.6.

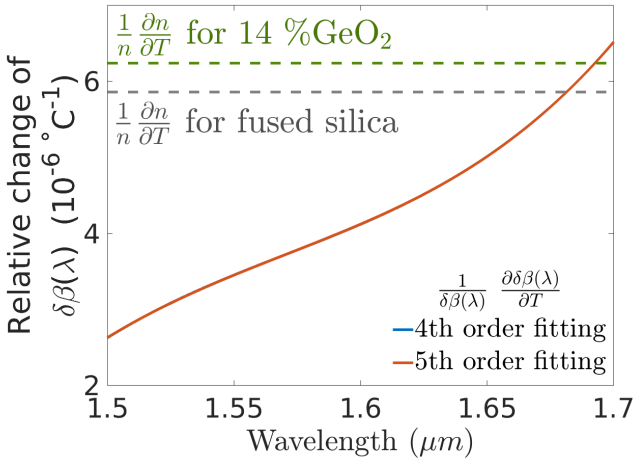

Figure 5.6 – Measured relative change of $\delta\beta(\lambda)$ with temperature (coinciding blue and red colored solid curves corresponding to 4^{th} and 5^{th} order 2-dimensional polynomial fitting of extracted phase with respect to wavelength), obtained using equation 5.4, exhibiting a strong change compared to the relative change in refractive index with temperature for fused silica (dashed gray curve) and 14 % GeO_2-doped silica (dashed green curve) in the wavelength range 1.5 μm-1.7 μm

Thus $\frac{1}{\delta\beta(\lambda)}\frac{\partial\delta\beta(\lambda)}{\partial T}$ can vary significantly ($2.5\times10^{-6}-6.5\times10^{-6}$ μm^{-1}) for 1.5 $\mu m \leq \lambda \leq 1.7$ μm. For most of this wavelength range, the values of $\frac{1}{\delta\beta(\lambda)}\frac{\partial\delta\beta(\lambda)}{\partial T}$ are also outside the range defined by the thermo-optic coefficients ($\frac{1}{n}\frac{dn}{dT}$) of fused silica [107] (5.9×10^{-6} $°C^{-1}$, indicated by dashed gray curve in figure 5.6) and 14 % GeO_2-doped silica [108] (6.2×10^{-6} $°C^{-1}$, indicated by dashed green curve in figure 5.6).

Figure 5.7 compares the measured relative wavelength shifts of GVE (see subsection 5.3.1), FBG resonance, closest TMI zero wavelength less than the GVE wavelength, MC resonance and farthest TMI zero wavelength less than the GVE wavelength, all weighted against the slope of the relative FBG wavelength shift [109]. The FBG was made using the Argon laser and phase mask of pitch 1079.31 nm. The MC pitch, duty cycle, intensity and exposure time per mark were 116 μm, 0.52, 5 $kWcm^{-2}$ and 10s, respectively. Compared to the relative shift of the FBG resonance wavelength, the relative shift of the GVE wavelength and MC resonance wavelength at $\lambda_{MC} = 1.5142$ μm are 2.9 and -5.4 times, respectively. The absolute value of relative wavelength shifts of the TMI fringes increases as the fringes are closer to the GVE wavelength. Compared to the relative shift of the FBG resonance wavelength, the relative wavelength shift of the farthest and closest TMI fringes from the GVE wavelength had values -4.7 and -17.6, respectively. The interpolated relative wavelength shift of TMI fringes (figure 5.5) at $\lambda = 1.5142$ μm is -4.9 $°C^{-1}$, while the measured value for the MC is -5.4 $°C^{-1}$. The error is less than 10 %. The small difference comes from the fact that $\delta\beta(\lambda)$ and $\frac{\partial\delta\beta(\lambda)}{\partial T}$ change upon exposure.

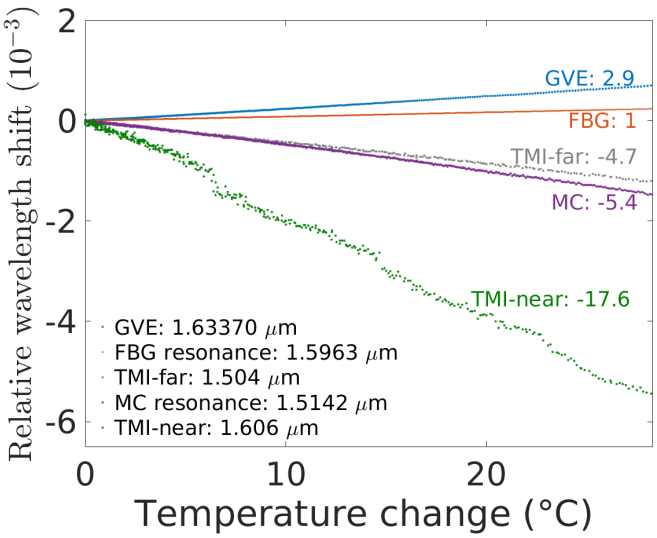

Figure 5.7 – Measured relative wavelength shift with temperature change for GVE, FBG, nearest fringe of TMI, MC and farthest fringe of TMI

Graphs of the MC and FBG spectra at the lowest temperature of the cooldown experiment are shown in figure 5.8. The temperature and strain response of MC resonance is a highly studied topic in itself due to the possibility of tuning the sensitivity by making the

resonance wavelength close to the GVE wavelength, although it was not concentrated on in this thesis.

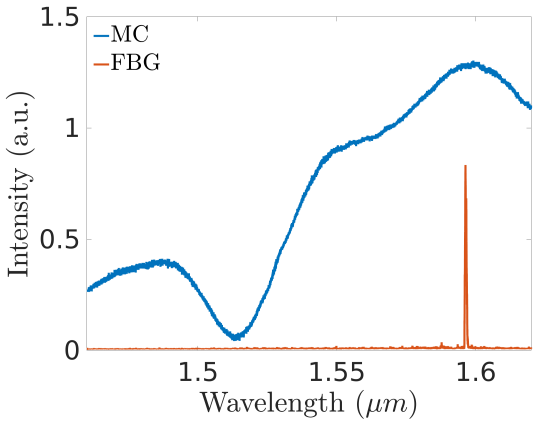

Figure 5.8 – Measured MC and FBG spectrum for the lowest temperature of the cooldown experiment

5.2.2 Strain response of TMI

Strain was applied on the whole few-mode fiber through translation stages. Coatings from parts of the single-mode pigtails were stripped, which was then glued with UV-cured resin on the translation stages (Figure 5.9). Stripping was necessary for avoiding partial force transfer through the coating of the fiber. In order to avoid temperature changes, this setup was covered with a polycarbonate box with a small hole through which the knob of the translation stage stuck out. Temperature inside the box was tracked with a thermocouple. Strain measurements were done once the temperature stabilized.
The fringes moved away from λ_e with increasing strain (Figure 5.10), as expected from the sign arguments in equation 5.2. λ_e itself shifted slightly with strain, whereas its relative shift was orders of magnitude smaller than the relative shift of the fringe extrema wavelengths . It stayed in the range 1.6368 μm $\leq \lambda_e \leq$ 1.6377 μm for $0 < \epsilon < 8.5 \times 10^{-4}$.

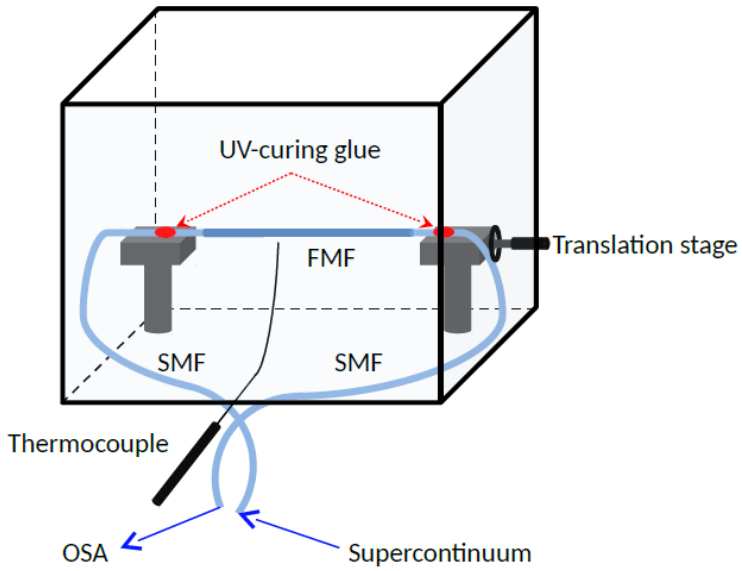

Figure 5.9 – Strain setup for TMI samples

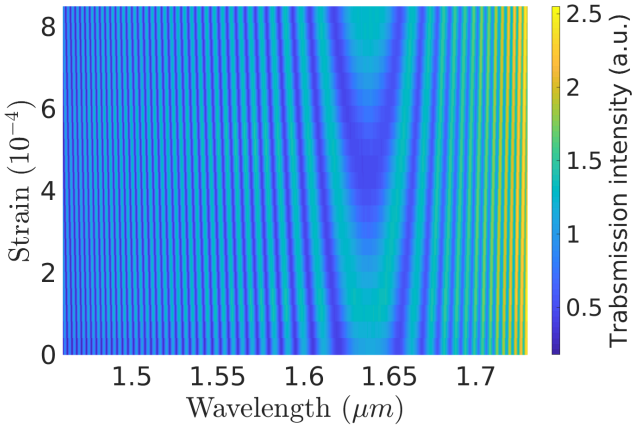

Figure 5.10 – Measured TMI transmission intensity spectrum (a.u.) for a 325 ± 0.5 mm long few-mode fiber sample, for different applied strains

From background and amplitude corrected signal of the first frame (zero strain), maxima and minima wavelengths corresponding to phases of $2M\pi : M \in \mathbb{Z}$ and $2M\pi \pm \pi : M \in \mathbb{Z}$ were extracted. Applying strain in small incremental values allowed continuous tracking of the extrema wavelengths and phase (without phase indeterminacy). The relative fringe shifts shown in figure 5.11 were linear. The lines which are increasing with strain correspond to maxima wavelengths larger than λ_e, whereas the lines which are decreasing with strain correspond to maxima wavelengths smaller than λ_e. The absolute value of the slope of the relative fringe shift increases as the maxima wavelengths get closer to λ_e.

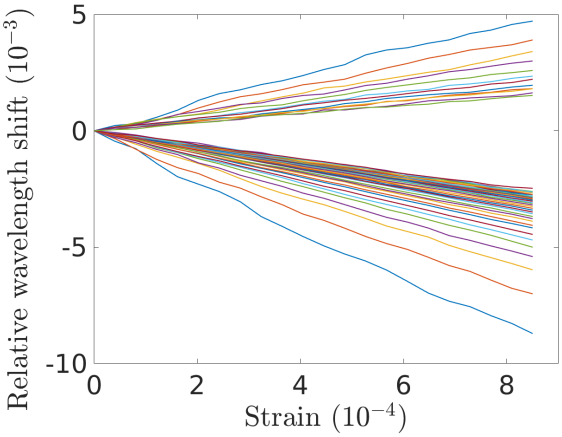

Figure 5.11 – Measured relative wavelength shifts of spectral maxima in figure 5.10. The apparent nonlinearity of the curves with extreme slopes come from the technical difficulty in precise determination of the two maxima wavelengths close to the GVE wavelength, to which these particular curves correspond

The slopes from linear fitting of the relative shift of the extrema wavelengths gave estimates of $\frac{1}{\lambda_m}\frac{d\lambda_m}{d\epsilon}$ (figure 5.12) at the fringe wavelengths. $\frac{1}{\lambda}\frac{d\lambda}{d\epsilon}$ seemed to blow up at $\lambda_e(\epsilon = 0)$. The functionality of $\frac{1}{\lambda_m}\frac{d\lambda_m}{d\epsilon}$ can be used to approximately predict the ratio of relative wavelength shifts of two MCs fabricated at different wavelengths, since the equations are the same for TMI and MC other than difference in the intermodal dispersion term. For MCs fabricated with weak index perturbations, $\frac{1}{\lambda_{MC}}\frac{d\lambda_{MC}}{d\epsilon} = \gamma(\lambda_{MC})\left[1 + \frac{1}{\delta\beta_{MC}(\lambda)}\frac{\partial\delta\beta_{MC}(\lambda)}{\partial\epsilon}|_{\lambda=\lambda_{MC}}\right] \approx \gamma(\lambda_{MC})\left[1 + \frac{1}{\delta\beta(\lambda)}\frac{\partial\delta\beta(\lambda)}{\partial\epsilon}|_{\lambda=\lambda_{MC}}\right]$.

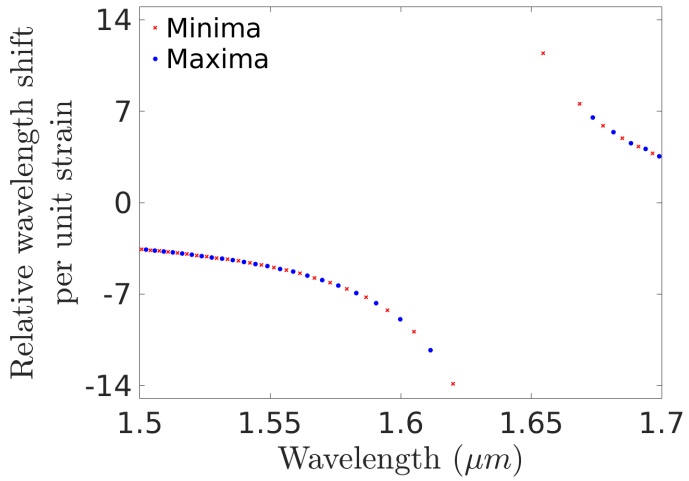

Figure 5.12 – Extracted linear slopes of relative wavelength shifts of extrema with applied strain.

TMI phase was sequentially extracted from the frames, by taking the phase of the previous frame as guess. $\phi(\lambda,\epsilon)$ was fitted with a two-dimensional polynomial which is linear in strain and of fourth order in wavelength. Similar to cooldown experiments, the linearity of the phase with strain is justified by the linearity of the fringe shift with strain. Figure 5.13 shows the estimate of the relative change of intermodal dispersion with strain ($\frac{1}{\delta\beta(\lambda)}\frac{\partial\delta\beta(\lambda)}{\partial\epsilon}$), which is obtained by applying equation 5.5 on the extracted phase change, together with the estimate of $\delta\beta(\lambda)$ from chapter 4. The quantity is highly dependent on wavelength, varying monotonically from to -0.28 to -0.80 for 1.5 μm $\leq \lambda \leq$ 1.7 μm, which has been illustrated as the solid blue curve in figure 5.13. In comparison, $\frac{1}{\beta_{01}(\lambda)}\frac{\partial\beta_{01}(\lambda)}{\partial\epsilon} \approx \frac{1}{\beta_{01}(\lambda)}\frac{\partial\beta_{01}(\lambda)}{\partial\epsilon}$ [110], which has a value $\approx -p_e = -0.22$, the strain-optic coefficient of silica [3; 4; 5]. The strain-optic coefficient of silica has been illustrated as the solid blue curve in figure 5.13. Therefore $\frac{1}{\delta\beta(\lambda)}\frac{\partial\delta\beta(\lambda)}{\partial\epsilon} \neq -p_e$. This implies that ignoring $\frac{1}{\delta\beta(\lambda)}\frac{\partial\delta\beta(\lambda)}{\partial\epsilon}$ for estimating $\delta\beta(\lambda)$, which was suggested by [82], is highly susceptible to errors.

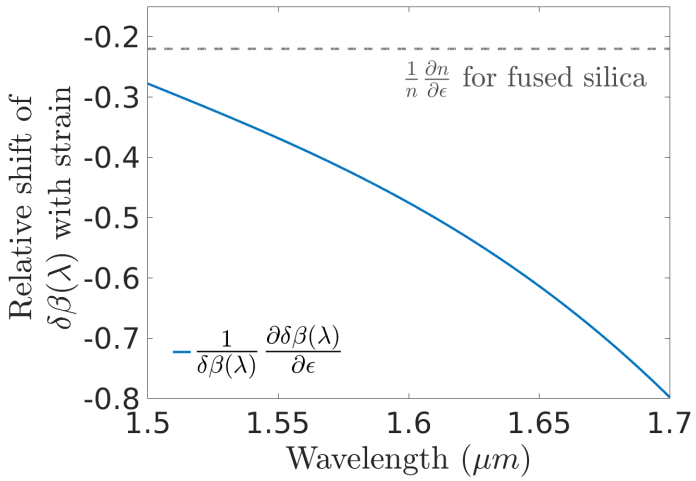

Figure 5.13 – Extracted relative shift of LP_{01}-LP_{02} intermodal dispersion with strain (blue curve), obtained using equation 5.5, indicating a strong change in the wavelength range 1.5 μm-1.7 μm compared to that obtained by simply using the strain-optic coefficient of fused silica (dashed gray curve)[3; 4; 5]

5.2.3 Scanning laser exposure response of TMI

Use of fiber Mach-Zhender interferometer with two physically separate arms consisting of two single mode fibers, for measuring the change in propagation constant in one of the single mode fibers due to laser irradiation, is long-known [111], . For a TMI sample, Mach-Zhender interferometer shares a common physical path but different optical lengths for the two modes. This enables measurement of the change in intermodal dispersion arising from UV exposure with a laser spot, and has already been measured with high resolution [97]. In the following measurements, uniformity of the laser exposure along the fiber axis was ascertained by scanning a laser spot with constant speed v along the

fiber axis. Under such exposure condition, the change in the intermodal dispersion curve, $\Delta\delta(\beta(\lambda))$, can be estimated using the following formula:

$$
\begin{aligned}
\phi(t)-\phi(0) &= \int_0^L \delta\beta(\lambda,z)\ dz \quad - \quad \int_0^L \delta\beta(\lambda)\ dz \\
&= \int_0^{L_F=v\ t} \Big(\delta\beta(\lambda)+\Delta\delta\beta(\lambda)\Big)\ dz + \int_{L_F}^{L} \delta\beta(\lambda)\ dz \quad - \quad \int_0^L \delta\beta(\lambda)\ dz \\
&= \int_0^{L_F} \Big(\delta\beta(\lambda)+\Delta\delta\beta(\lambda)\Big)\ dz \quad - \quad \int_0^{L_F} \delta\beta(\lambda)\ dz \\
&= \int_0^{L_F} \Delta\delta\beta(\lambda)\ dz \\
&= L_F\ \Delta\delta\beta(\lambda) \\
&= v t\ \Delta\delta\beta(\lambda) \\
\implies \frac{d\phi(\lambda)}{dt} &= v\ \Delta\delta\beta(\lambda)
\end{aligned}
\tag{5.6}
$$

where t represents time, L is the length of the FMF and L_F is the length of the exposed part. The estimate from this method is only indicative with respect to periodic exposure of marks along the fiber axis for making MCs , since the index change from a static laser spot and a scanning laser spot are different, depending on the beam shape and photosensitivity response. Using multiple passes over the exposed length, it is possible to estimate the change for different fluence for the same intensity.

For this experiment, the Pharos 4H laser beam (table 3.3) was focused using a cylindrical fused silica lens of effective focal length 10 mm. At the position of the fiber axis, the $\frac{1}{e^2}$ diameters of the beam profile with assumed elliptical cross-section were 60 μm and 1800 μm along the fiber and perpendicular to the fiber, respectively. The spot size was roughly estimated from throughfocus measurements, taking care to incorporate the fiber cross-section in the optical path, and assuming no self-focusing. The average laser power was 40 mW, 1 KHz repetition rate and pulse duration of 180 fs, corresponding to peak intensity of approximately 0.5×10^{12}W cm^{-2}. Energy per pulse was 40 μJ. The speed of scanning along the fiber axis was v =20 μms^{-1}. Figure 5.14 shows the shift of TMI fringes with exposure. Four scanning exposures were performed over a length of 43 mm in alternating directions, whose spectra are separated by the red lines in figure 5.14. $L = 51$ mm was taken to have enough number of fringes in the TMI spectra. Single spectral acquisition after every 60 s was done using the si155 MI interrogator (0.1 s acquisition time). For the data analysis, only the spectra concurrent with the scanning of the laser

spot were used. From visual inspection, the induced photosensitive change is maximum for the first scan, and decreasing with each subsequent scan, probably due to decrease in photosensitivity with increased fluence. Eleven spectral frames are missing from the beginning of the first scan.

Applying equation 5.6 to the extracted phase change over the first scan (cumulative exposure of $\Delta t = 3\ s$ per point from 1 scan of the laser spot), and separately over the second scan (cumulative exposure of $\Delta t = 6\ s$ per point from 2 scans of the laser spot), the change in intermodal dispersion, $\Delta\delta(\beta(\lambda))$ for the corresponding exposure conditions have been estimated. Equations 5.2 and 5.3 with $X = t$ relates the fringe shift to the unwrapped phase. Different two-dimensional polynomials, of degrees 2,3 and 4 in the wavelength variable, and degree 1 (linear) in the time variable, were used to fit the extracted phase over these two sets of exposure, which verifies the accuracy of the fitting method. The third and fourth scans are not reported since the fitting results for different degrees of polynomials were significantly different for each of those scans, therefore deeming the fits unreliable. The relative change in $\delta\beta(\lambda)$ for each of the first and second scans is shown in figure 5.16, for different degrees of fitting polynomial in the wavelength variable for each individual scan. Compared to the magnitude of the intermodal dispersion of the pristine fiber, $0.0533\ \mu\text{m}^{-1} \leq \delta\beta(\lambda) \leq 0.0536\ \mu\text{m}^{-1}$ for $1.46\ \mu\text{m} \leq \lambda \leq 1.62\ \mu\text{m}$, the measured perturbation $\Delta\delta\beta(\lambda)$ is less than $3 \times 10^{-4}\ \mu\text{m}^{-1}$ over four scans, which corresponds to less than 0.6 % change in $\delta\beta(\lambda)$. The low value is due to the small intensity of the laser spot, arising from the lack of focussing in the directional perpendicular to the fiber axis. $\Delta\delta\beta(\lambda)$ might have arisen from changes in both the core and cladding index, induced by the high peak power. Since measurements were not done to identify whether the index change happened only for the core or also for the cladding, speculations were avoided.

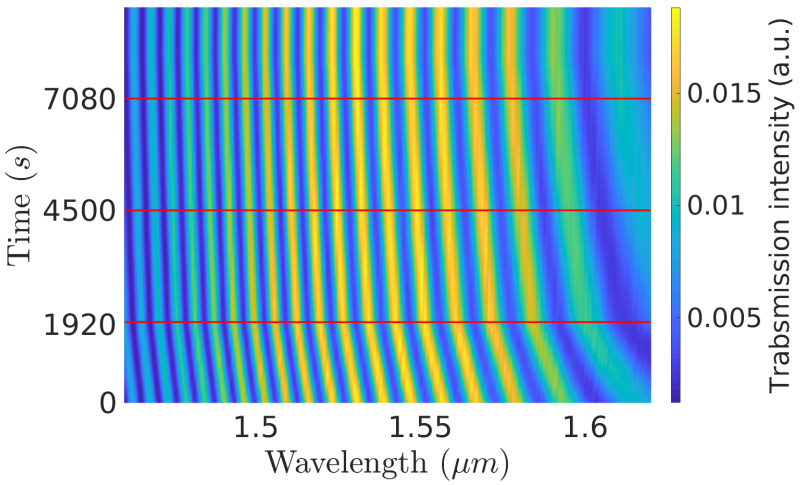

Figure 5.14 – Measured TMI fringe shift with exposure for four scans with translation speed v =20 μms^{-1} over the whole length of the FMF in the TMI sample. The red lines delineate the start of a new scan

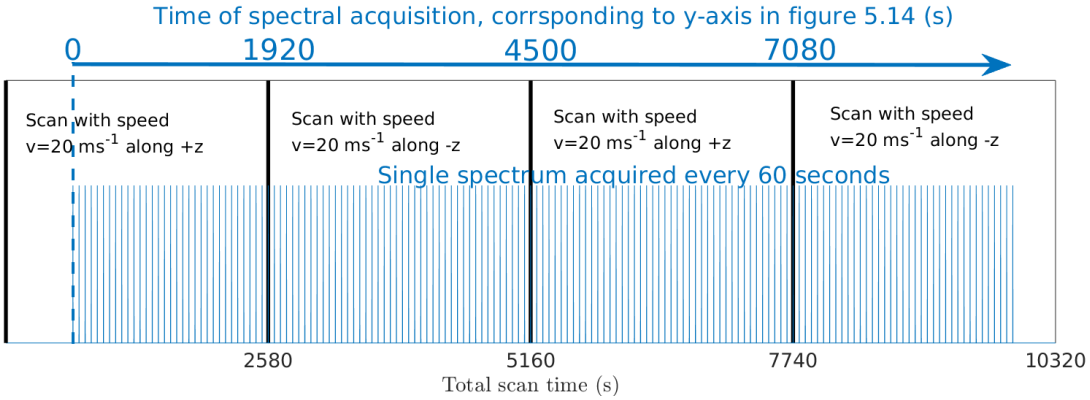

Figure 5.15 – Timing diagram of figure 5.14

The timing diagram of the spectra in figure 5.15 is illustrated in figure 5.16.

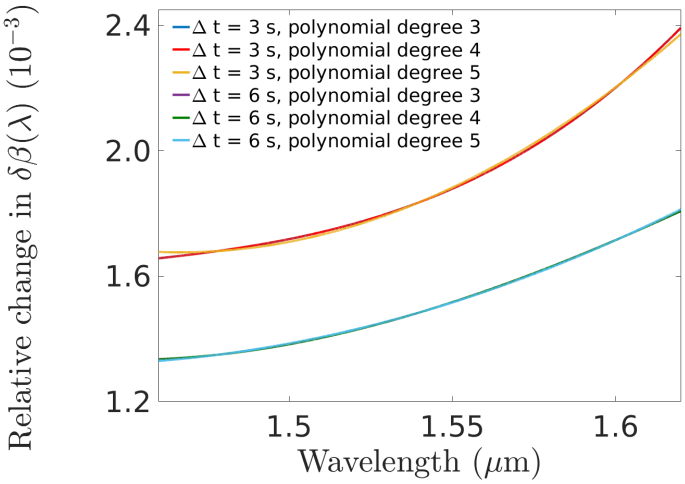

Figure 5.16 – Change of intermodal dispersion with scanning laser spot, obtained using equation 5.6 on the extracted phase of the TMI in figure 5.14, for the first (3 s exposure per point on the FMF) and second scan (6 s total exposure per point on the FMF from 2 consecutive scans of the laser spot)

5.3 Effect of perturbations on GVE

In addition to fringe shift, the GVE wavelength λ_e can also shift with temperature [84], strain, laser exposure and bending [96; 112]. The dispersion curves can be described by the normalized $V-b$ parameters with some fixed dependency, as long as the shape of the fiber index profile does not change significantly under such perturbations.

$$V = \frac{2\pi a}{\lambda}\sqrt{n_1^2 - n_0^2} \tag{5.7}$$

$$b = \frac{n_e^2 - n_0^2}{n_1^2 - n_0^2} \tag{5.8}$$

where λ is wavelength, a is the core radius, n_0 is the cladding index and n_1 is a well-defined index corresponding to the core, for example the maximum of the core index.

If the perturbation does not significantly affect the shape of the refractive index profile and consequently the $V-b$ diagram compared to the changes in a,n_0 and n_1, the relative change of $V_e = V(\lambda_e)$ can be ignored with respect to the these parameters. Differentiating the logarithm of equation 5.7 gives

$$\begin{aligned} \frac{2}{V_e}\frac{dV_e}{dX} &= \frac{2}{a}\frac{da}{dX} + \frac{2}{n_1^2(\lambda_e) - n_0^2(\lambda_e)}\left[n_1(\lambda_e)\frac{dn_1(\lambda_e)}{dX} - n_0(\lambda_e)\frac{dn_0(\lambda_e)}{dX}\right] - \frac{2}{\lambda_e}\frac{d\lambda_e}{dX} = 0 \\ \implies \frac{1}{\lambda_e}\frac{d\lambda_e}{dX} &= \frac{1}{a}\frac{da}{dX} + \frac{1}{n_1^2(\lambda_e) - n_0^2(\lambda_e)}\left[n_1(\lambda_e)\frac{dn_1(\lambda_e)}{dX} - n_0(\lambda_e)\frac{dn_0(\lambda_e)}{dX}\right] \end{aligned} \tag{5.9}$$

5.3.1 Effect of temperature on GVE wavelength

Figure 5.17 shows the measured shift of GVE wavelength with temperature, which appears to be highly linear. The linear fit of measured GVE wavelength gives $\lambda_e(T) = (4.077 \pm 0.004) \times 10^{-5} T + (1.632657 \pm 0.000002)$ μm, where T is in °C, which corresponds to measured $\frac{1}{\lambda_e}\frac{d\lambda_e}{dT} = (2.497 \pm 0.003) \times 10^{-5}$ K^{-1}.

For $X = T$ (temperature), most of the parameters in equation 5.9 are known; $\frac{1}{a}\frac{da}{dT} = 0.6 \times 10^{-6}$ K^{-1} [106] and $\frac{dn_0(\lambda_e)}{dT} = 8.46 \times 10^{-6}$ K^{-1} (Following from figure D.3 in the PhD thesis [108], which also matches the average of the numbers corresponding to wavelengths 1.5 μm, 1.6 μm and 1.8 μm in table 6 of [107] for fused silica at 300 K temperature). For the FMF, $n_0(\lambda_e) = 1.443$ and $n_1(\lambda_e) = 1.463$, where n_1 is defined as the maximum index of the index profile. $n_1(\lambda_e) = 1.463$ is achieved when the concentration of GeO_2 in the glass is 14 %. For this concentration of GeO_2 in silica, $\frac{dn_1(\lambda_e)}{dT} = 9.13 \times 10^{-6}$ K^{-1} (Following from figure D.3 in the PhD thesis [108]). Putting this in equation 5.9, an estimate of $\frac{1}{\lambda_e}\frac{d\lambda_e}{dT} = 2.6 \times 10^{-5}$ K^{-1} is obtained. The estimate from equation 5.9 is less than 14 % off from the measurement. Following equation 5.9, $\frac{1}{\lambda_e}\frac{d\lambda_e}{dT}$ should approximately be same for all mode pairs.

λ_e is intrinsic to intermodal dispersion, which depends on the transverse refractive index profile of fiber and does not depend on length of the TMI sample [77]. For the temperature range 25.3 °C<T<53.7 °C, GVE showed a linear shift. Since the linear shift

is confirmed by both step-index simulations with appropriate material parameters and measurements performed in this thesis, it is highly likely that nonlinear shift of GVE wavelength with temperature reported in literature [84] is from systematic error. Such systematic error can easily arise in absence of precise phase unwrapping and in presence of large temperature change during acquisition of a single spectrum. Such problems are mitigated in this work by precise phase unwrapping and slow cooldown rate.

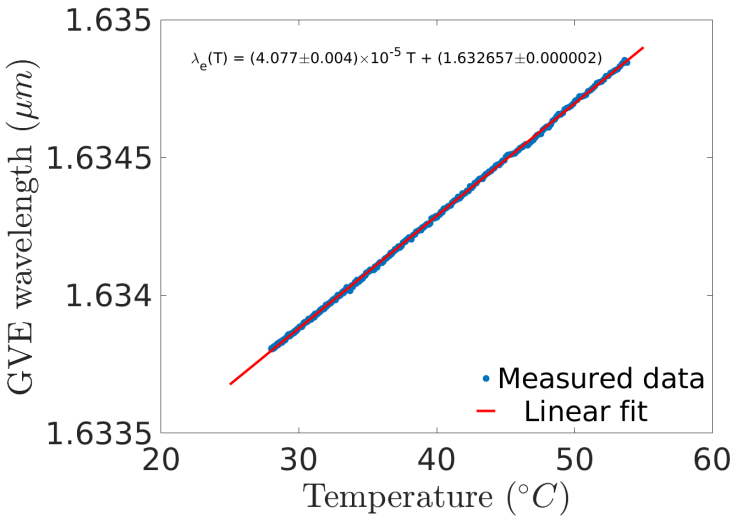

Figure 5.17 – Measured temperature response of GVE wavelength

It is also important to take into consideration the shift of GVE due to bending while undertaking sensing experiments [96; 112]. Other than observing a a 4 nm shift in the GVE wavelength when it was wound around the aluminum cylinder, no further systematic characterization was done in this thesis.

5.3.2 Effect of strain on GVE wavelength

Figure 5.18 shows the measured response of λ_e with strain ϵ, which shows linear dependence. A linear fit of the measurements gives $\lambda_e(\epsilon) = (1.01 \pm 0.01)\epsilon + (1.637681 \pm 0.000004)\ \mu$m. This corresponds to measured $\frac{1}{\lambda_e}\frac{d\lambda_e}{d\epsilon} = (-0.62 \pm 0.006)$.

For $X = \epsilon$ (strain), $-\frac{1}{a}\frac{da}{d\epsilon} = \nu$, Poisson's ratio and $\frac{1}{n_0(\lambda_e)^3}\frac{dn_0(\lambda_e)}{d\epsilon} = \frac{1}{n_1^3(\lambda_e)}\frac{dn_1(\lambda_e)}{d\epsilon} = -\frac{p_{12}-\nu(p_{11}+p_{12})}{2}$ from photoelasticity theory [113; 114] . Thus from equation 5.9

$$\begin{aligned}\frac{1}{\lambda_e}\frac{d\lambda_e}{d\epsilon} &= -\nu - \frac{n_1^4(\lambda_e) - n_0^4(\lambda_e)}{n_1^2(\lambda_e) - n_0^2(\lambda_e)}\frac{p_{12} - \nu(p_{11}+p_{12})}{2} \\ &= -\nu - \left(n_1^2(\lambda_e) + n_0^2(\lambda_e)\right)\frac{p_{12} - \nu(p_{11}+p_{12})}{2} \end{aligned} \tag{5.10}$$

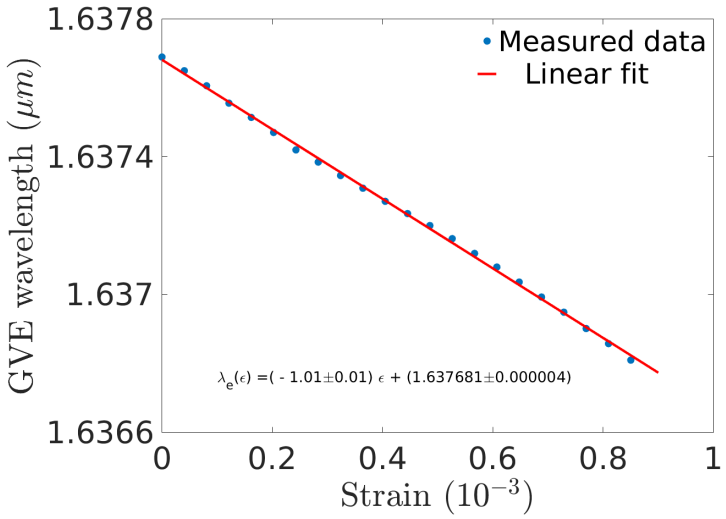

Figure 5.18 – Measured strain response of GVE wavelength

In a first approximation, $p_{11} = 0.12$, $p_{12} = 0.27$ [4] and $\nu = 0.164$ [5] is taken to be the values of fused silica, since the contribution from the cladding dominates compared to the core, as the former has ≈ 155 times larger area in the cross-section. This gives an estimate $\frac{1}{\lambda_e}\frac{d\lambda_e}{d\epsilon} = -0.60$. The estimate from equation 5.10 is less than 3.5 % off from the measurement. Therefore material parameters are dominant in $\frac{1}{\lambda_e}\frac{d\lambda_e}{d\epsilon}$, which implies that it should have similar value for any mode pair, independent of the modes, according to equation 5.9.

5.3.3 Effect of laser exposure on GVE wavelength

From accurate measurements of TMI shift under local irradiation, the change in photosensitive core index can be estimated by incorporating explicit calculations of the $V-b$ diagram of the fiber [97]. However a direct method does not exist in literature which avoids calculating the $V-b$ diagram of the FMF. Such a novel method is presented here which works for certain irradiation conditions, and is based on shift of the GVE wavelength.

For $X = F$ (laser fluence), photosensitivity can be estimated under the particular conditions that only the core should be affected (a) by uniform photo-induced index change along the core (e.g. UV laser exposure which does not cause nonlinear effects in fused silica), or (b) by such a small amount that even non-uniform photo-induced index change does not change the transverse index profile significantly to cause a significant change in the $V-b$ diagram of the FMF. In such cases $\frac{1}{n_0(\lambda_e)}\frac{dn_0(\lambda_e)}{dF} = 0$ and $\frac{1}{a}\frac{da}{dF} = 0$ in equation 5.9,

thus leading to

$$\frac{1}{\lambda_e}\frac{d\lambda_e}{dF} = \frac{n_1(\lambda_e)}{n_1^2(\lambda_e) - n_0^2(\lambda_e)}\frac{dn_1(\lambda_e)}{dF}$$
$$= \frac{n_1^2(\lambda_e)}{n_1^2(\lambda_e) - n_0^2(\lambda_e)}\left(\frac{1}{n_1(\lambda_e)}\frac{dn_1(\lambda_e)}{dF}\right) \tag{5.11}$$

Thus for small fluence, and if $n_0(\lambda_e)$ and $n_1(\lambda_e)$ are known, estimate of $\frac{dn_1(\lambda_e)}{dF}$ is obtained from the shift of the GVE wavelength using equation 5.11. Compared to the relative shift of an FBG resonance wavelength ($\approx \frac{1}{n_1(\lambda)}\frac{dn_1(\lambda_e)}{dF}$) due to uniform exposure across the grating length, the relative shift of GVE wavelength approximately $\frac{n_1^2(\lambda_e)}{n_1^2(\lambda_e)-n_0^2(\lambda_e)}$ times larger, by equation 5.11. Care has to be taken to expose the full length of the few-mode fiber uniformly before recording a new spectrum to determine the shifted GVE wavelength, so that the GVE pertains to the full fiber. Otherwise the formula of the GVE coming from dissimilar segments is complicated.

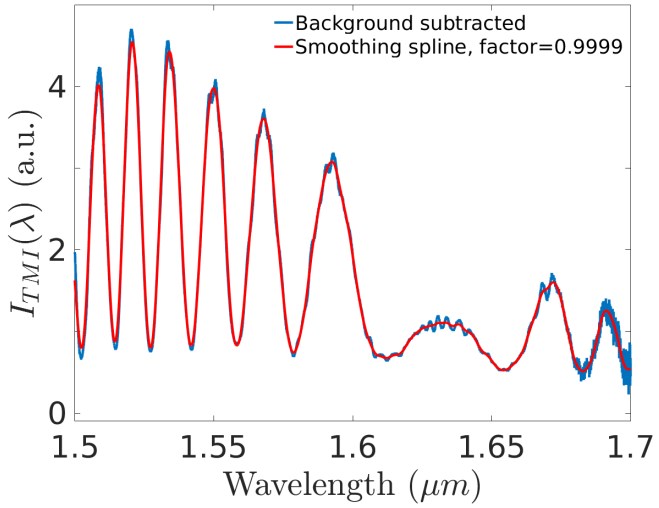

Figure 5.19 – Measured TMI spectrum for FMF length 37 mm. Due to small number of fringes, phase unwrapping using zero wavelengths like chapter 4 was unreliable. Therefore smoothing spline was fitted to the first frame with a smoothing factor=0.9999 as defined in Matlab curve fitting toolbox to obtain a smooth fit, on which the extrema could be detected with certainty and thereby the phase could be estimated by cosine fitting of the normalized TMI spectrum. For further frames, the fitted intensity envelope and phase for the previous frame was used as guess for directly fitting equation 4.2

Figure 5.19 shows the measured TMI spectrum from a TMI sample containing a 37 mm long few-mode fiber. There are less than 10 fringes for such a short sample, in addition to high noise at longer wavelengths. To have reliable normalization using all

available fringes, the background corrected spectra were individually smoothed with cubic smoothing splines, with suitable smoothing factors. Figure 5.20 shows the GVE extracted from each normalized spectrum, as a function of exposure time per point on the fiber axis. The laser spot size and intensity are same as section 5.2.3: A focused cylindrical spot of the Pharos 4H laser beam with assumed elliptical cross-section had diameter of 60 μm and 1800 μm along the fiber and perpendicular to the fiber, respectively. The average laser power was 40 mW, 1 KHz repetition rate and pulse duration of 180 fs, corresponding to peak intensity of approximately 0.5×10^{12}W cm^{-2}. Energy per pulse was 40 μJ. For a scan over 41 mm with a speed of 1.2 mm/min, every point was exposed for 3 s during each scan. Therefore the laser fluence/dose per scan was 141 Jcm^{-2} per point of the exposed fiber. Spectrum was gathered at the end of each scan. 41 scans were performed.

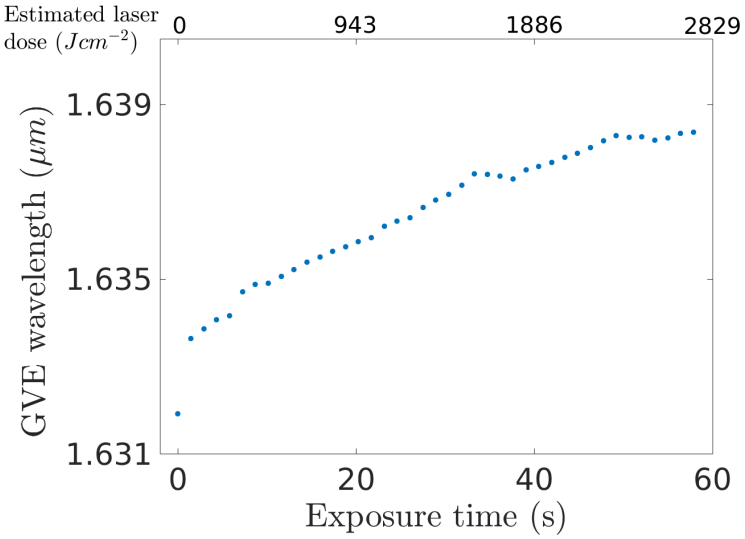

Figure 5.20 – Measured shift of GVE wavelength with laser exposure

The minimum measured shift of λ_e is $1 \times 10^{-4}\mu$m. Given $\lambda_e = 1.6319$ μm, $n_0(\lambda_e) = 1.443$ and $n_1(\lambda_e) = 1.463$, this corresponds to an index change $\Delta n_1(\lambda_e) = 2.4 \times 10^{-6}$. In comparison, the resolution for measuring effective index change via the shift of the resonance of a weak FBG (around λ_e) is $\Delta n_1(\lambda_e) = 9 \times 10^{-6}$, when measured with a spectrometer with resolution of 10 pm (e.g. MI si155 interrogator). In addition, measuring TMI fringes do not require very high spectral resolution (50 pm is this particular case). The maximum index change was $\Delta n_1 = 1.6 \times 10^{-4}$. Following the treatment of [115; 116], shown in figure 5.21, the following power law dependence is obtained for constant spot intensity and laser pulse-width:

$$\Delta n_1(t) = C\ t^{(0.426\ \pm\ 0.007)} \tag{5.12}$$

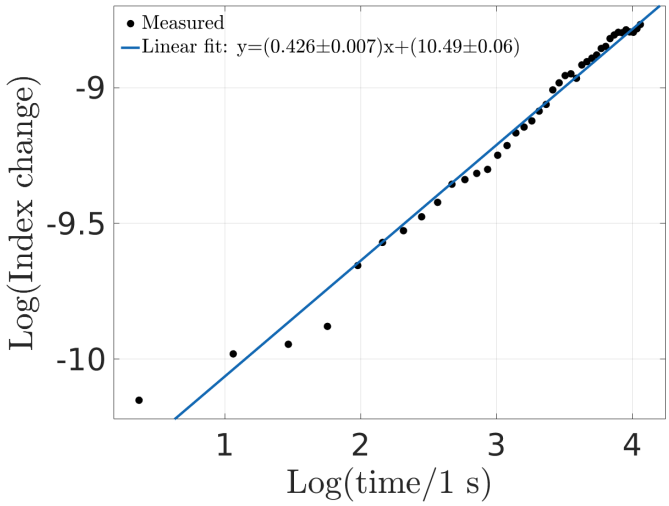

Figure 5.21 – Change of core index with exposure time, t_0=1 s

For finding the power law exponent similar to [115; 116], fitting with respect to t suffices for constant intensity and pulse-width, since t is then proportional to the number of pulses. Neither actual measurement nor systematic variation was done for the intensity (considering focusing and losses by the fiber itself) and the pulse-width; a 10 % error in the intensity gives a >20 % error in the square of the fluence. Therefore the analysis was restrained to only the power law exponent which can be determined with high confidence. The value of the exponent of time seems small compared to existing literature (0.7 reported by [116] for fused silica, and 0.66 reported by [115] for 5.5 % GeO_2 concentration in the core). This might be due to the lack of measurement points at low fluence, resulting in large uncertainty in determining the exponent, or due to other mechanisms of photosensitivity. Judiciously avoiding speculations on such mechanisms without undertaking appropriate experiments, it is shown here as a proof-of-principle that such exponents can be measured using the GVE wavelength, which can be later used for fabrication or material studies.

5.4 Temperature and strain differentiation

Resonant structures fabricated in fibers are widely used for sensing modalities [110; 117]. As in the general theme of the thesis to use non-resonant and resonant spectral responses in FMF either individually or in combination to measure various modalities, the capability to differentiate temperature and strain using such a combination is explored. This method has a few benefits-

1. Non-resonant devices are less demanding to make technically.

2. For the particular combination of GVE wavelength and FBG resonance wavelength used here, the signs of sensitivities improve both the accuracy and the differentiation capability of the method.

5.4.1 Working principle

Most generally, temperature or strain is differentiated by tracking two quantities which vary linearly with these parameters. For example, some reported combinations are resonance peaks of gratings (FBGs in spliced dissimilar fibers [118; 119], two FBGs with one isolated from strain [120], FBG and LPG [121], different resonances from the same FBG in a few-mode fiber [100], some function of the strength of grating combinations (LPG and FBG) [101], FBG and in-fiber Mach-Zhender interferometer [122; 123], FBG and TMI peak [102] etc. The benefit of finding linearly dependent parameters with temperature and strain is that the dependence can be written as a linear equation:

$$\begin{bmatrix} p_1 \\ p_2 \end{bmatrix} = \begin{bmatrix} K_{1T} & K_{1\epsilon} \\ K_{2T} & K_{2\epsilon} \end{bmatrix} \begin{bmatrix} T \\ \epsilon \end{bmatrix} \tag{5.13}$$

p_1 and p_2 are the two parameters which are experimentally tracked, T represents temperature and ϵ represents strain. K_{1i} are the coefficients of the linear variations of these parameters with fixed strain, and K_{2i} are the coefficients of the linear variations of these parameters with fixed temperature. If the temperature coefficient is independent of strain and vice versa, the coefficients are just constant numbers. Under these circumstances, the temperature and strain is then estimated by solving this linear equation for measured p_1 and p_2 , which gives the solution:

$$\begin{aligned} \begin{bmatrix} T \\ \epsilon \end{bmatrix} &= \frac{1}{K_{1T}K_{2\epsilon} - K_{2T}K_{1\epsilon}} \begin{bmatrix} K_{2\epsilon} & -K_{1\epsilon} \\ -K_{2T} & K_{1T} \end{bmatrix} \begin{bmatrix} p_1 \\ p_2 \end{bmatrix} \\ &= \frac{1}{K_{1T}K_{2\epsilon} - K_{2T}K_{1\epsilon}} \begin{bmatrix} p_1K_{2\epsilon} - p_2K_{1\epsilon} \\ p_2K_{1T} - p_1K_{2T} \end{bmatrix} \end{aligned} \tag{5.14}$$

The accuracy depends on the error of determining p_1 and p_2, combined with the errors in measuring K_{ij}. The standard deviations in estimating the slope and intercept of a linear least square fitting from measurements with error bars is given by standard regression theory. The errors in determining p_1 and p_2 depend on the measurement and data analysis technique used. An useful way to determine the total error estimate of any similar method is to consider the error analysis of the following function, which is the

general description of the terms in the formulae for T and ϵ in equation 5.14 [98; 124]:

$$f(x_1, x_2, y_1, y_2) = x_1 y_2 - x_2 y_1 \tag{5.15}$$

$$\left|\frac{\Delta f(x_1, x_2, y_1, y_2)}{f(x_1, x_2, y_1, y_2)}\right| \leq \frac{|x_1 y_2|(\left|\frac{\Delta x_1}{x_1}\right| + \left|\frac{\Delta y_2}{y_2}\right|) + |x_2 y_1|(\left|\frac{\Delta x_2}{x_2}\right| + \left|\frac{\Delta y_1}{y_1}\right|)}{|x_1 y_2 - x_2 y_1|} \tag{5.16}$$

The error bounds in equation 5.16 can be applied individually for the terms $K_{1T}K_{2\epsilon} - K_{2T}K_{1\epsilon}$, $p_1 K_{2\epsilon} - p_2 K_{1\epsilon}$ and $p_2 K_{1T} - p_1 K_{2T}$ in equation 5.14, since all these terms are of the form in equation 5.15. The denominator in equation 5.16 implies that the total relative error of a function of the form 5.15 is smaller when one of the parameters among (x_1, x_2, y_1, y_2) has opposite sign compared to the others, for the same relative error of the individual parameters. This is a criteria for choosing a method with better accuracy, which holds in the case of this FMF since only $K_{2\epsilon}$ has a negative value when $p_1 = \lambda_{FBG}$ is the resonance wavelength of an inscribed FBG and $p_2 = \lambda_e$ is the GVE wavelength of $LP_{01} - LP_{02}$ mode pair.

The sensitivities and differentiation efficiency can be understood by normalizing the rows of the dependence equation [98]

$$\begin{bmatrix} p_1 \\ p_2 \end{bmatrix} = \begin{bmatrix} \frac{K_{1T}}{\sqrt{K_{1T}^2+K_{2T}^2}} & \frac{K_{1\epsilon}}{\sqrt{K_{1\epsilon}^2+K_{2\epsilon}^2}} \\ \frac{K_{2T}}{\sqrt{K_{1T}^2+K_{2T}^2}} & \frac{K_{2\epsilon}}{\sqrt{K_{1\epsilon}^2+K_{2\epsilon}^2}} \end{bmatrix} \begin{bmatrix} T\sqrt{K_{1T}^2+K_{2T}^2} \\ \epsilon\sqrt{K_{1\epsilon}^2+K_{2\epsilon}^2} \end{bmatrix} = \mathbb{P} \begin{bmatrix} T\sqrt{K_{1T}^2+K_{2T}^2} \\ \epsilon\sqrt{K_{1\epsilon}^2+K_{2\epsilon}^2} \end{bmatrix} \tag{5.17}$$

The coefficient in each individual column of $\mathbb{P}$ is the projection of some two-dimensional unit vector. Considering only the magnitude of sensitivity, the measured parameters p_1 and p_2 will have larger change for the same change in either T or ϵ when the factors K_{ij} are larger in magnitude. This leads to the simple conclusion that the sensitivity of the method is more when the magnitudes of the coefficients of $\mathbb{P}$ are larger. On the other hand, since temperature and strain are independent quantities, the differentiation efficiency is maximized if p_1 and p_2 are also independent. For this to happen, the matrix $\mathbb{P}$ should be a composition of rotation(s) and/or reflection(s) matrices, and consequently the determinant of $\mathbb{P}$, name $det(\mathbb{P})$ has value ± 1. For practical cases, the differentiation efficiency is more for larger values of $|det(\mathbb{P})|$. Compared to all coefficients having the same sign, $|det(\mathbb{P})|$ increases when one of the four coefficients of $\mathbb{P}$ has a sign which is different to the other three coefficients. This condition is satisfied by the tracking parameters used here: $p_1 = \lambda_{FBG}$ is the resonance wavelength of an inscribed FBG and $p_2 = \lambda_e$ is the GVE wavelength of $LP_{01} - LP_{02}$ mode pair. Only the GVE wavelength has a negative proportionality constant with strain while all the other three proportionality constants are positive.

5.4.2 Experiment parameters

The following parameters corresponding to a few-mode fiber (FMF) were used in our experiments for temperature and strain differentiation:

Parameter	Abbreviation	Description
p_2	λ_e	Group-velocity equalization (GVE) wavelength of the LP_{01} and LP_{02} mode in the FMF.
p_1	λ_{01}	Resonance wavelength of LP_{01} mode from a Fiber Bragg Grating (FBG) written in the FMF.

For determining the resonance wavelength of the FBG $LP_{01} - LP_{01}$ reflection peak, λ_{01}, full-width half-maxima wavelength is used. This wavelength is defined as the average of nearest wavelengths corresponding to half of the FBG peak strength, which are nearest to and on two sides of the FBG resonance wavelength. This method is robust to noise than direct peak wavelength detection, due to the sharp slopes near the half-maxima wavelengths and the noise at the strongest parts of the peak.

Different setups were used to study the temperature and strain responses. Insulated water bath (figure 5.2a) was used for the temperature studies, while translation stages with UV glue (figure 5.9) was used to apply strain. For TMI spectra, SuperK Extreme broadband light source from NKT photonics was used as the source. The spectrometer was the Ando OSA 6317Q, operated with a resolution of 50 pm, sensitivity "Mid" and fixed equispaced sample of 10000 points between 1.46 μm and 1.73 μm. For FBG spectra, the experiments were repeated using tunable laser interrogator from Micron Optics (si155).

5.4.3 Measurements and analysis

Both the GVE wavelength and the FBG resonance wavelength turned out to be highly linear with both temperature and strain (figure 5.23). The measurement range for temperature was $T \in (22.9°C,\ 55°C)$ for FBG resonance wavelength and $T \in (25.3°C,\ 55°C)$ for GVE wavelength, with $\epsilon = 0$ (Figure 5.23a 5.23b) . For strain, the measurement range was $\epsilon \in (0,\ 0.001)$ for $T = 22.9° \pm 0.1°C$ (Figure 5.23c, 5.23d). The fitted curves are

$$\lambda_e(T) = \left[(4.077 \pm 0.004) \times 10^{-5} T + (1.632657 \pm 0.000002)\right] \mu\text{m} \tag{5.18}$$

$$\lambda_e(\epsilon) = \left[(-1.01 \pm 0.01) \times \epsilon + (1.637681 \pm 0.000004)\right] \mu\text{m} \tag{5.19}$$

$$\lambda_{FBG}(T) = \left[(1.098 \pm 0.002) \times 10^{-5} T + (1.573126 \pm 0.000001)\right] \mu\text{m} \tag{5.20}$$

$$\lambda_{FBG}(\epsilon) = \left[(1.186 \pm 0.003) \times \epsilon + (1.560693 \pm 0.000001)\right] \mu\text{m} \tag{5.21}$$

where the unit of T is °C. FBG reflection spectra recorded at temperatures 22.9 °C and 55.0 °C are shown in figure 5.22. Since the maximum of the LP_{01}-LP_{01} peak was noisy with respect to wavelength, the average of the wavelengths corresponding to half of the maximum of the peak strength was defined as the FBG wavelength $\lambda_{FBG}(T)$ for the temperature T corresponding to each recorded FBG spectrum.

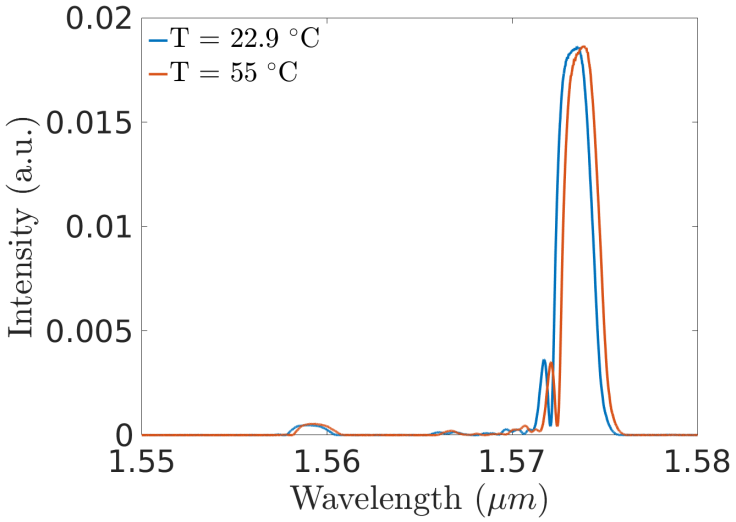

Figure 5.22 – Measured reflection spectrum from an FBG written in the FMF, at 22.9 °C and 55.0 °C

It was noted after the submission of this thesis that the resonance wavelength of the FBG used for strain measurements corresponded to an effective index of 1.446 for LP_{01}, which is too low for the FMF. Possibly due to an accidental mixing up of fibers before FBG irradiation, another fiber like SM 1500 was irradiated and used for this set of experiments. However, since relative wavelength shift of FBG resonance in fibers with strain is almost similar for different GeO_2 concentrations, the measured proportionality coefficient may suffice for the presented proof-of-principle studies.

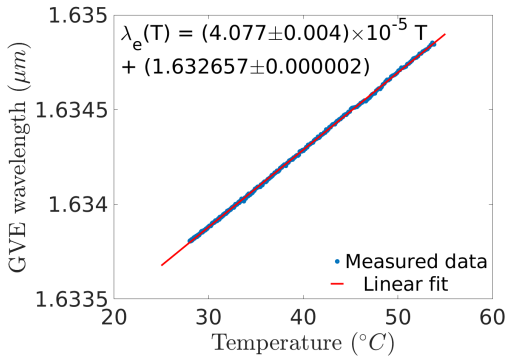

(a) Temperature response of GVE wavelength

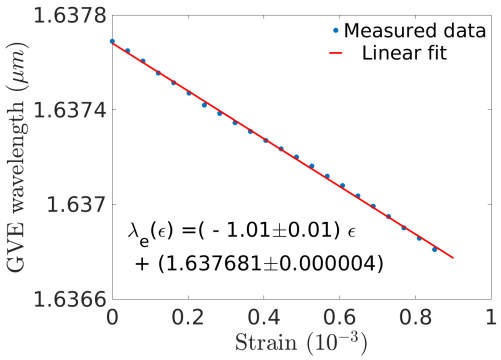

(b) Strain response of GVE wavelength

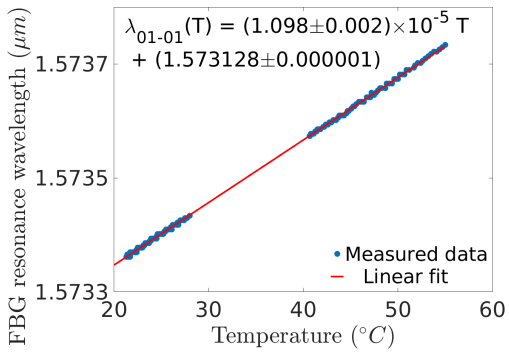

(c) Temperature response of FBG LP_{01-01} resonance wavelength

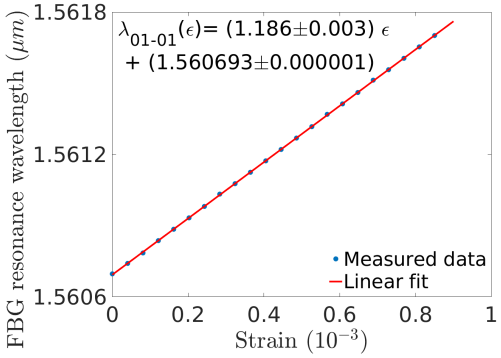

(d) Strain response of FBG LP_{01-01} resonance wavelength

Figure 5.23 – Measured temperature and strain dependence of λ_e and λ_{FBG}, with corresponding linear fits

Putting together the linear slopes from equations 5.18, 5.19, 5.20 and 5.21 in the inverted matrix equation 5.14 gives:

$$\begin{bmatrix} T \\ \epsilon \end{bmatrix} = \frac{1}{(5.94 \pm 0.02) \times 10^{-5}} \begin{bmatrix} (1.186 \pm 0.003) & (1.01 \pm 0.01) \\ -(1.098 \pm 0.002) \times 10^{-8} & (4.077 \pm 0.004) \times 10^{-8} \end{bmatrix} \begin{bmatrix} \lambda_e \\ \lambda_{FBG} \end{bmatrix} \tag{5.22}$$

Assuming a nominal value of $|\frac{\Delta\lambda_e}{\lambda_e}| \leq 3 \times 10^{-6}$ from the error estimate of polynomial root determination based on its coefficients, and $|\frac{\Delta\lambda_{FBG}}{\lambda_{FBG}}| \leq 5 \times 10^{-6}$ from the resolution of the tunable laser interrogator, relative errors of 1.4 % and 1.1 % were determined for temperature and strain respectively using equation 5.16. This corresponds to an error in estimating temperature of 0.8 °C at 55 °C. For strain, the error is 1.1×10^{-5} at a strain

of 0.001.

5.5 Conclusion

In this chapter, the following methods have been presented:

- Experimental methods to estimate $\frac{\partial \delta\beta(\lambda)}{\delta T}$, $\frac{\partial \delta\beta(\lambda)}{\delta \epsilon}$ and $\frac{\partial \delta\beta(\lambda)}{\delta F}$, for temperature ($T$), strain ($\epsilon$) and fluence ($F$), using TMI fringes. The method for estimating the effect of fluence works under the condition that the laser spot is scanned across the fiber at constant speed. The method for $\frac{\partial \delta\beta(\lambda)}{\delta T}$ has also been reported by another group in January 2019 [76]

- The temperature and strain dependence of GVE wavelength is explained, using simple model from the $V-b$ diagram, based only on material parameters. The error between the estimate and the measurements were less than 3 %, showing that material terms dominate in the GVE wavelength shift.

- A new method is presented for measuring the index change of the photosensitive core on UV irradiation, based on GVE. The novelty lies in the capability to directly estimate changes in the core index without undertaking the calculation for the $V-b$ diagram of the fiber [97]. Unlike FBGs, this method allows the exact measurements of the change of index starting from no exposure. The resolution is also high compared to measuring FBG resonance spectra with same spectral resolution . The method is valid only when the whole few-mode fiber is scanned with a laser spot, which limits speed and puts technical tolerances based on the measurable spectral range and number of fringes needed for phase estimation.

- Proof-of-principle of temperature and strain differentiation is shown using GVE wavelength and LP_{01-01} resonance wavelength from an FBG written in the same fiber. Relative errors of 1.4 % and 1.1 % were obtained respectively for temperature and strain, which offer a promising proof-of-principle. However full characterization by varying both temperature and strain for different values of each other was not done. The error on all the steps of the estimation algorithm was carefully tracked, including fitting GVE and FBG resonance wavelength, and the matrix inversion necessary to estimate temperature and strain from that.

6 Effect of irradiation of marks on intermodal dispersion

Although resonances of gratings composed of weak index modulations closely follow the intermodal dispersion of the pristine fiber [54], the effect of strong index modulation on the intermodal dispersion felt by the MC can be significant [33; 34]. It is understood that for a step-index fiber the MC feels the average of the core index along the location of the MC [33]. However, there is a lack of techniques to directly predict the effect of a particular mark irradiation condition on the intermodal dispersion experienced by an MC. The situation is even more complex for non-step-index fibers. There are empirical publications on this topic [34], which ask for attention to find possible methods to predict the effect of irradiation on the intermodal dispersion curve experienced by an MC.

This chapter presents a novel way to predict this effect, which works by connecting two measurable quantities- (a) additional intermodal phase introduced per mark, measured from shift of non-resonant TMI and (b) single points on MC dispersion curve $\delta\beta_{MC}(\lambda)$, defined by the MC pitch Λ_{MC} and the resonance wavelength λ_{MC} by the relation $\frac{2\pi}{\delta\beta_{MC}(\lambda_{MC})} = \Lambda_{MC}$. Once the TMI phase shift has been measured for any particular irradiation and alignment condition with a pitch which does not cause resonant mode conversion, consequently resonance wavelength can be predicted for the full measured wavelength range. Experimental verification is presented and technical requisites for the model to work are discussed.

6.1 Theory: Connection between intermodal dispersion and TMI

Due to index change in the core from periodic irradiation of N marks along the fiber axis, the MC does not feel only the intermodal dispersion curve of the pristine fiber, $\delta\beta(\lambda)$ [34]. If the exposure conditions (mark shape, intensity (I) and fluence (F)) are maintained over

the different exposed marks, then each mark adds an extra phase $\Delta\phi(\lambda, I, F)$ between the two corresponding modes, without causing any change in the period length. The phase experienced by the interacting modes can be calculated by adding the phase coming from the pristine fiber $\Lambda_{MC}\delta\beta(\lambda)$ over the period length Λ_{MC}, with the phase added by a mark $\Delta\phi(\lambda, I, F)$. The sum of these is the actual phase difference experienced per period length of the MC by the interacting modes, and therefore satisfies the following equation:

$$\Lambda_{MC}\delta\beta(\lambda) + \Delta\phi(\lambda, I, F) = \int_{z}^{z+\Lambda_{MC}} \delta\beta(\lambda, z')\ dz' \tag{6.1}$$

where an MC period is starting at z, and $\delta\beta(\lambda, z')$ is the modified intermodal dispersion at location $z \leq z' \leq z + \Lambda_{MC}$. With respect to this actual phase per period length experienced by the modes, the phase-matching condition at the resonance wavelength λ_{MC} is give by

$$\Lambda_{MC}\delta\beta(\lambda_{MC}) + \Delta\phi(\lambda_{MC}, I, F) = \int_{z}^{z+\Lambda_{MC}} \delta\beta(\lambda_{MC}, z')\ dz' = 2\pi \tag{6.2}$$

$$\implies \delta\beta(\lambda_{MC}) + \frac{\Delta\phi(\lambda_{MC}, I, F)}{\Lambda_{MC}} = \frac{2\pi}{\Lambda_{MC}}$$

Equation 6.2 is particularly amenable to accurate experimental verification using fabricated MCs, once estimate of $\Delta\phi(\lambda, I, F)$ for the corresponding irradiation condition is available from a complimentary TMI measurement method introduced in chapter 6.3.1. With respect to definition of average intermodal dispersion per period length experienced by the interacting modes introduced in section 2.1.6, $\delta\beta_{MC}(\lambda, I, F, \Lambda_{MC}) = \frac{1}{\Lambda_{MC}} \int_{z}^{z+\Lambda_{MC}} \delta\beta(\lambda, z')\ dz'$, equation 6.1 can be rewritten as:

$$\delta\beta_{MC}(\lambda, I, F, \Lambda_{MC}) = \frac{1}{\Lambda_{MC}} \int_{z}^{z+\Lambda_{MC}} \delta\beta(\lambda, z')\ dz' = \delta\beta(\lambda) + \frac{\Delta\phi(\lambda, I, F)}{\Lambda_{MC}} \tag{6.3}$$

In order to verify equation 6.2, estimates of $\delta\beta_{MC}(\lambda, I, F, \Lambda_{MC})$ over measured wavelength range were compared to the MC wavevectors $\frac{2\pi}{\Lambda_{MC}}$ at resonance wavelengths, for MCs fabricated using small, medium and large duty cycles. For a complementary verification of equation 6.2, as well as to get a more accurate estimation for the unknown offset of $\delta\beta(\lambda)$ compared to chapter 4, the estimated values of $\delta\beta(\lambda)$ at a fixed wavelength were compared for different duty cycles.

In existing literature, there is no method which can directly measure the extra phase coming from every exposed mark, $\Delta\phi(\lambda, I, F)$. A novel method to measure $\Delta\phi(\lambda, I, F)$, coming from each mark is presented here, which uses periodic or aperiodic writing of non-resonant marks, such that no mode conversion takes place. Resonant writing is avoided as it mixes the effects of mode conversion and addition of phase from every irradiated mark, which is complicated to separate.

Writing non-resonant marks in the FMF shifts the TMI phase. Measurement of the

phase shift before and after writing a mark directly gives an estimate of $\Delta\phi(\lambda, I, F)$. In practical experiments, the phase change $\Delta\phi(\lambda, I, F)$ estimated from writing a single mark is highly noisy, along with the risk of having an error from the indeterminate offsets in the pre- and post-exposure spectra. This is solved by writing multiple non-resonant marks, then manually correcting spurious phase-unwrapping offsets and finally fitting the phase change at every measured wavelength with a linear curve. Since the independent variable in the fitted linear curve is the number of marks N, there is physically no possible source of nonlinearity as long as the environmental parameters (temperature, strain) and the exposure parameters are reasonably maintained. Since the effect of temperature on $\delta\beta_{MC}(\lambda)$ is much smaller(chapter 5.2.1) than the irradiation, it was ignored during the MC exposure experiments. Although strain could have been ignored as well due to the same reason(5.2.2), equal amount of small strain was applied on each sample by using a removable pivot and magnetic weights. This additionally helped in keeping the fiber straight. Twists were avoided in the sample during loading.

With respect to the number of written marks N and wavelength, a two-dimensional polynomial was fitted to the extracted phases
$\widetilde{\phi}_N(\lambda, 0 \le n \le N) = \widetilde{c}_{0,N} + \sum_{m=1}^{d} (\widetilde{c}_{m,N}\lambda^m + n\, c_{m,N}\lambda^{m-1}) = \widetilde{c}_{0,N} + \sum_{m=1}^{d} \left(\widetilde{c}_{m,N}\lambda^m + n\, \Delta\phi_N(\lambda, I, F)\right)$,
where the quantity $\widetilde{\phi}_N(\lambda, n)$ is the extracted phase of the TMI spectra recorded after writing n-number of marks, which has a degree d in wavelength. Assuming repeatable phase change from each mark, the dependency of $\widetilde{\phi}_N(\lambda, n)$ with n was taken to be linear. Therefore an estimator of the extra phase added per mark is given by the partial derivative of $\widetilde{\phi}_N(\lambda, n)$ with respect to n. The limit of this estimator, provided it converges within a preset tolerance, gives precise estimate of the extra phase added per mark within that tolerance.

$$\Delta\phi_N(\lambda, I, F) = \frac{\partial}{\partial n}\widetilde{\phi}_N(\lambda, n) = \sum_{m=1}^{d} c_{m,N}\lambda^{m-1}$$

$$\Delta\phi(\lambda, I, F) = \lim_{N\to\infty} \Delta\phi_N(\lambda, I, F) \tag{6.4}$$

6.2 Experimental setup

6.2.1 Femtosecond laser setup with spherical lens

From the engineering perspective, laser power was easily maintained from the "power setting" mode of the Pharos SP-06-200-PP laser with the 4H (fourth harmonic) module (Table 3.3). The laser was single mode and the angular stability of the beam was in μrad range when it is started in "cold start" mode. For maintaining similar $\Delta\phi(\lambda, I, F)$ for the marks, the crucial parameters were the transverse axis Y (perpendicular to both the laser and fiber axis) and the axial alignment along X (along the laser axis) of the fiber core with respect to the laser focal spot (Figure 6.1). X and Z axes are adjusted

with Aerotech translation stage, which has 10 nm resolution. Jitter of the stage along both axes when the stage is stalled is ±20 nm. Transverse alignment along Y axis was done with motorized screws of 30 nm resolution (model Newport 8742 motorized screws, the control GUI of which is shown in bottom right of figure 6.2). The fiber core was approximately coincided with the laser focus along the fiber axis, with the optical path shift due to the fiber taken into consideration. Transverse alignment along Y was done by checking the symmetry of the far-field fringes after the FMF, from the line scan of images of the far-field fringe pattern (Figure 6.2). Only the largest peaks in the fringe were used to check symmetry. For peak intensity of 0.7×10^{13} Wcm^{-2} and fluence of 3500 Jcm^{-2}, change in λ_{MC} of up to 7 nm was observed for sub-micron misalignments along the laser axis, for a spot size of approximately 25 μm along the fiber axis. Such a large shift in resonance was probably caused by a shift in the center of the self-focused spot due to misalignment, thereby causing a different profile of index perturbation. The possible self-focusing of the beam comes from nonlinear refractive change caused by the peak intensity of the laser spot, which can be characterized using the formula $\frac{0.148\lambda_0^2}{n_{clad}\ n_{NL}}$ [125] for the critical power, above which a linearly polarized Gaussian laser beam at wavelength λ_0 self-focuses in a material which has linear and nonlinear refractive indices n_{clad} and n_{NL}. For $\lambda_0 = 0.257$ μm, the material constants for fused silica are $n_{clad} = 1.504$ and $n_{NL} = 2.44 \times 10^{-16}$ Wcm^{-2} [126], which gives a critical power of 0.3 MW. The peak power of the laser beam before being incident on the fiber was 0.4 GW, which is far above the calculated critical power. Ionization of the focused spot in air was also observed with the spherical lens. Therefore given the high peak power and peak intensity for the spherical lens, and further focusing of the beam by the fiber itself perpendicular to its axis, self-focusing was expected for the spherical lens. Thus the alignment of the laser spot perpendicular to the fiber axis was crucial for maintaining the irradiation parameters over different parts of the fiber.

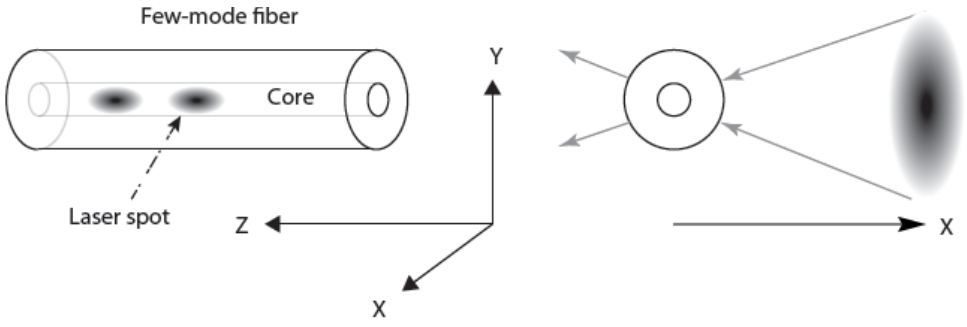

Figure 6.1 – Schematic of mark irradiation with fs laser for MC and TMI. Z is the fiber axis. The figure on the left shows the view from the X direction, while the one on the right shows the view from the Z direction

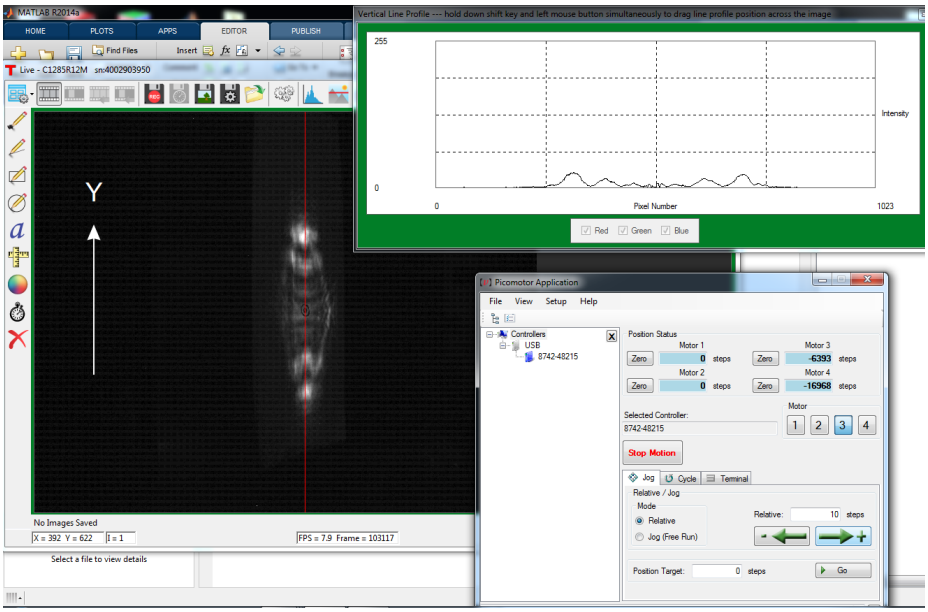

Figure 6.2 – The monochrome image shows a far field fringe behind the FMF after focusing the femtosecond laser spot. The green inset on top shows a line scan of the fringe along the red line, which is placed along the horizontal axis of symmetry of the fringe. The fiber is aligned using the buttons of GUI on the bottom right, till the line scan of the fringe becomes symmetric, as is presented in the inset line scan (green box on top right)

For alignment along laser axis, two complementary methods were used.

- The location of the core was checked with respect to a fixed point drawn on a CCD camera screen (Figure 6.3), while the camera imaged the FMF perpendicular to both the fiber axis and the laser axis. The camera was mounted at a fixed location and orientation on the optical table.
- The strengths of the largest peaks (equalized by transverse alignment) in the fringes was made to be the same on both the ends of the sample.

Axial and transverse alignment were iteratively repeated till all these criteria were satisfied to the available resolution. At the end of such an iteration cycle, the distance of the core from the fixed point on the camera screen was checked visually while translating the fiber along the fiber axis. This gave additional information whether the axial alignment was maintained over the whole sample length, which could not be checked with fringes as exposure would have changed the sample. This step was important since the Aerotech translation stage could not maintain exact alignment along the fiber axis for the entire available range of its translational motion. The effect of this was observed on screen but could not be quantified due to lack of resolution. Out of the available range Z=(-27.5 mm, 28.5 mm) along the fiber axis, only the range Z=(-27.5 mm, 23.5 mm) was used

after visual verification of the alignment on the screen, which sufficed for the verification of equation 6.2 for small and large duty cycles. Loading and unloading the fiber caused changes in all the alignments. Since the quality of the far-field fringes from a particular point in the fiber degraded quickly with exposure, the fiber was oscillated along the fiber axis for a distance of 0.3 mm with a speed of 5 mm/min during the alignment procedure with sufficient intensity for far-field imaging.

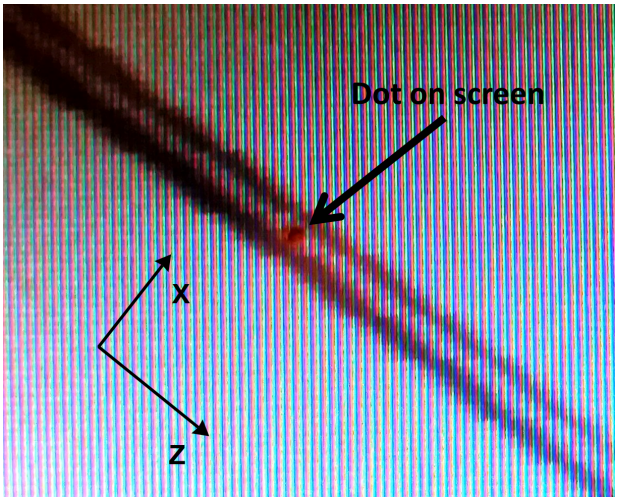

Figure 6.3 – Axial alignment at Z=-27.5 mm. The black arrow points the reference dot drawn on the camera screen

6.2.2 Excimer laser setup from Optec

The excimer laser used was a commercial LSV3 ArF laser from Optec, at 193 nm (table 3.3). The setup contains an inverted microscope aligned along Y axis (Figure 6.4), both for imaging and beam delivery, and the Aerotech translation stage. The laser spot at the focus of the microscope objective can be chosen to have circular shape with different sizes, using one of the many available circular apertures inside the beam-delivery system. The fiber was loaded parallel to the Z axis on two X-Y-Z flexure stages which were mounted on the translation stage. The focusing of the fiber through the objective was determined optimal when the edges of the FMF core had showed maximum image contrast. The fiber height was maintained by checking the focusing of the fiber on the extremal ends of the translation stage movement. The spot size was measured by clicking the two edges of the fluorescence coming from the fiber core during exposure, using the ”line measurement” tool inbuilt in the laser control software. For the transverse alignment along X (Figure 6.4), the fiber core was aligned with the cross in the imaging screen along X at the two extremes of the movement range of the translation stage, as shown in figure 6.5. An external trigger generated from the Aerotech translation stage after each translation was used to trigger the shooting of laser pulses. The number of laser pulses for each interrupt was preset in the laser control software. The entire procedure was automated using the

programming interface of the translation stage provided by Aerotech.

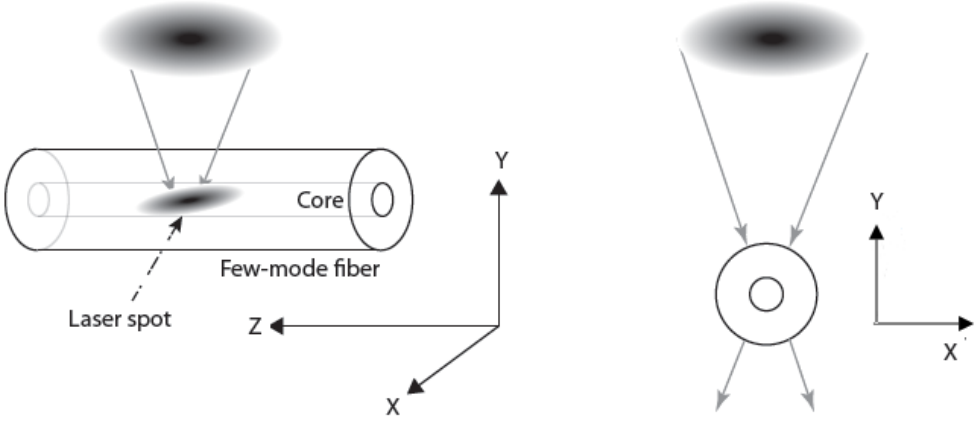

Figure 6.4 – Schematic of mark irradiation with Optec LSV3 excimer laser for MC and TMI. The figure on the left shows the view from the X direction, while the one on the right shows the view from the Z direction

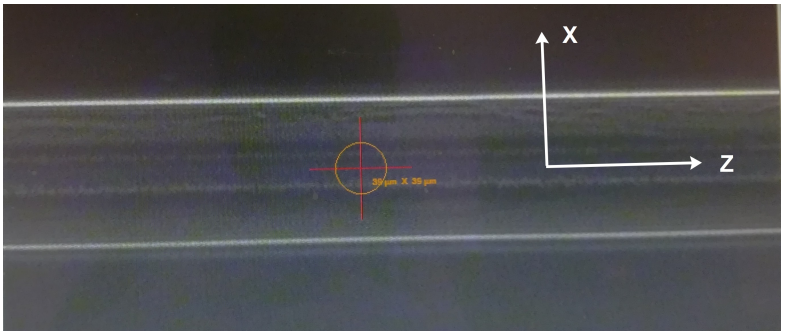

Figure 6.5 – FMF viewed at the focus of the imaging and beam-delivery objective of the Optec LSV3 Excimer setup, showing cross-arrows for the center of the focus. The white lines showing coordinates has been added laser for showing the actual coordinates aligned with fiber axis

6.3 Experimental results

6.3.1 Phase unwrapping from TMI and MC fabrication

Once the alignment was completed, marks were written with a constant pitch. The pitch had to be chosen carefully, sometimes with a few iterations, to maintain the following conditions:

- In TMI samples, avoid mode conversion even at wavelengths slightly outside the measurement range, which otherwise scrambles the extrema intensities in an an unpredictable manner. This adds systematic error to the determination of $\Delta\phi(\lambda, I, F, N)$, as illustrated later in figure 6.9.

- In MC samples, avoid conversion to cladding modes which have a peak close to the resonance wavelength, so that the peaks from the LP_{01}-cladding mode resonance and the LP_{01}-LP_{02} resonance do not coincide.

Figure 6.6 shows the shift of TMI fringes after writing each mark, using a pitch which avoids the onset of any mode conversion between the corresponding modes. The fringes shift away from GVE wavelength with the irradiation of each mark. The fringe shift is faster for the fringe wavelengths closer to GVE wavelength. For the first frame, the phase was extracted by fitting equation 4.2 to the spectrum, where the offset of the phase was arbitrarily assigned. Every other frame was also fitted with equation 4.2 to extract the phase, with the difference being that the guess of the fitting algorithm was taken to be the fitting outputs of the previous frame.

Equation 5.2 with $X = N$, number of marks, relates the fringe shift to the unwrapped phase.

Although at each wavelength, the phase added per mark was linear, the slope of the cumulative phase as a function of wavelength is unstable for small number of marks. Therefore sufficient number of marks needed to be written to have a stable estimate of $\Delta\phi(\lambda, I, F)$. The number of needed marks for stable estimation was determined by checking when the estimate $\Delta\phi_N(\lambda, I, F)$ (Equation 6.4) from the spectral series of frames {1,2...,N} (Figure 6.6) converged to a limit, as shown in figure 6.7. In this particular case, the fitted $\Delta\phi_N(\lambda, I, F)$ achieved limit within tolerance of 10^{-4} radians from 190 marks onwards. Thus writing 200 marks was deemed sufficient for estimating $\Delta\phi(\lambda, I, F) = \Delta\phi_{200}(\lambda, I, F)$ with this tolerance. It is important to keep in mind that a systematic or sudden shift in alignment will cause a systematic shift in $\Delta\phi_N(\lambda, I, F)$ with the number of written marks, thus adding uncertainty in determining whether $\Delta\phi_N(\lambda, I, F)$ has achieved a limit. This is another reason why precise alignment is a prerequisite for this method.

Note that, since the actual axial shape and amplitude of the marks are already clumped together in the term $\Delta\phi(\lambda, I, F)$, the exact knowledge of those parameters becomes unnecessary for estimating $\delta\beta_{MC}(\lambda)$. For low-loss marks, the only other term $\kappa(\lambda)$ needed to explicitly represent the mode conversion spectrum is measurable, and is cumulatively defined per period length of the MC (see equation 2.43). Therefore further microscopic details of both $\Delta\phi(\lambda, I, F)$ and the coupling constant $\kappa(\lambda)$ are redundant, except the dependence of maximum achievable extinction ratio on the duty cycle which was experimentally observed.

Furthermore, it is also noteworthy that if TMI is excited in an FMF containing an MC, the MC scrambles the neighboring extrema intensities of the TMI fringes differently in an unpredictable manner over a wavelength range broader than the MC peak. This indicates that the mode conversion and TMI are originating from the same mode pair. In contrast, conversion to another core mode or a cladding mode only reduces the TMI fringe contrast

locally in an uniform way, without affecting the neighbouring fringe maxima differently.

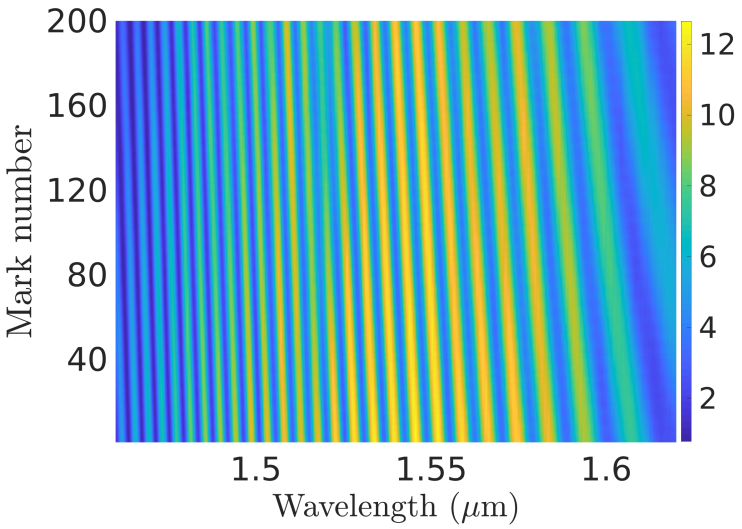

Figure 6.6 – 3D plot of measured evolution of TMI spectrum with mark number N. The pitch was chosen to be 105 μm such that no mode conversion happens between LP_{01} to higher order LP modes within the measured range of wavelength. At each wavelength, phase was added linearly per mark. The mark length was 95 μm. Colorbar shows transmission in arbitrary units. The fringes appear smudged around 1.52 μm after writing sufficient number of marks, which is due to the appearance of a cladding mode

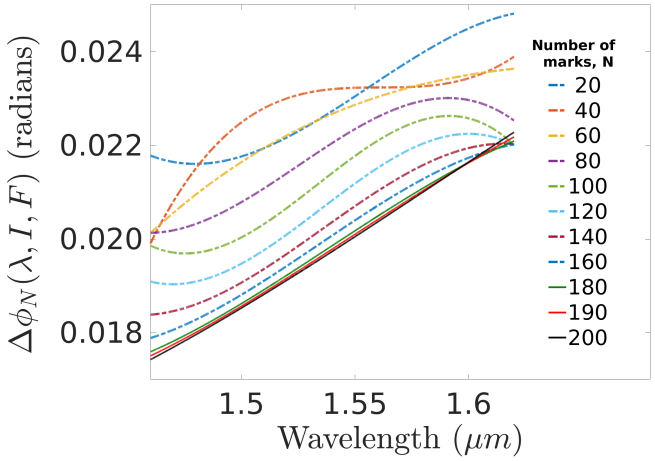

Figure 6.7 – Estimated average phase added per mark (Equation 6.4), showing convergence after writing sufficient number of marks

Further errors in phase unwrapping can arise from the method used in normalizing the TMI spectra and guessing the phase from cosine fitting with polynomial phase. This was characterized by checking estimates of $\Delta\phi_N(\lambda, I, F)$ for sufficiently large N with respect to polynomial fitting degrees of wavelength. An estimate was considered usable only if it did not vary too much for the different fitting degrees, as was the case of the 200

marks presented in figures 6.6 and 6.7. The different fitting degrees for wavelength for this particular measurement is presented in figure 6.8. An unusable example is presented in figure 6.9, which is the result of phase extraction from a TMI sample contaminated by the sidebands of an undesired MC. Since increasing the fitting degree gave inconsistent results, such data is deemed unsuitable for estimating the average phase added per mark and not analyzed further. In order to generally avoid such situations, the pitch was carefully chosen such that no mode conversion occurs while measuring the TMI shift.

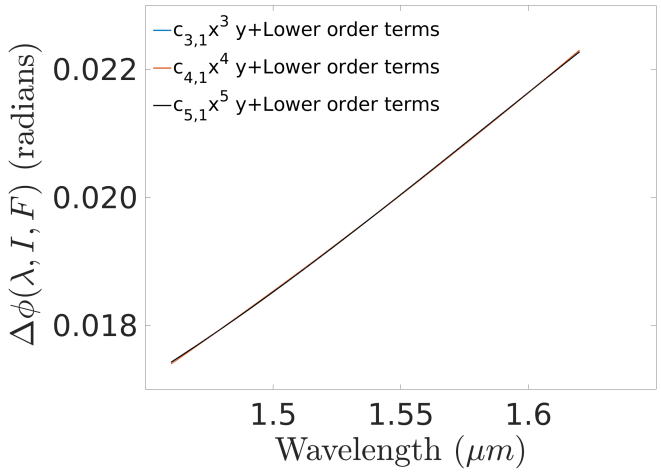

Figure 6.8 – In a measurement *without* mode conversion, comparison between different degrees of fitting polynomial for the average phase added per mark estimated using equation 6.4. once is has stabilized for 200 marks. The results for different fitting degrees are overlapping, deeming this measurement suitable for making estimations

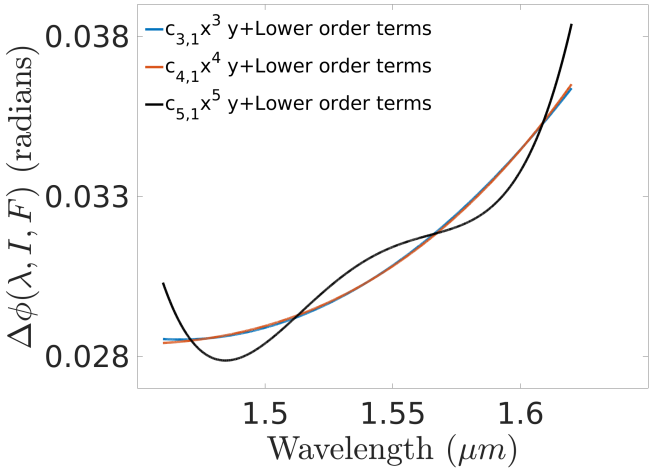

Figure 6.9 – In a measurement *with* mode conversion, comparison between different degrees of fitting polynomial for the average phase added per mark, once the estimate using equation 6.4 has stabilized after writing 200 marks. The inconsistency between different fitting degrees deems this measurement unsuitable for making estimations

Once reliable estimates of the average phase added by every laser mark was achieved, mode converters were fabricated at different pitches using the same conditions for exposure and alignment as the TMI. The evolution of the mode converters were monitored during exposure. If the resonance wavelength deviated significantly during the exposure, the laser was stabilized and the alignment procedure was repeated. Only MC exposures where the wavelength deviation during exposure was less than ±1 nm were accepted. Figure 6.10a and 6.10b show an example of an exposure using the femtosecond laser (table 3.3) with an average intensity 0.3×10^{13} Wcm^{-2} before the fiber, exposure time of 5 s, with a mark of $\frac{1}{e^2}$ diameter of 95 ± 1 μm and 1800 ± 2 μm, along the fiber axis and perpendicular to the fiber axis. The pitch was 117.5 μm, thereby giving a duty cycle of 0.81.

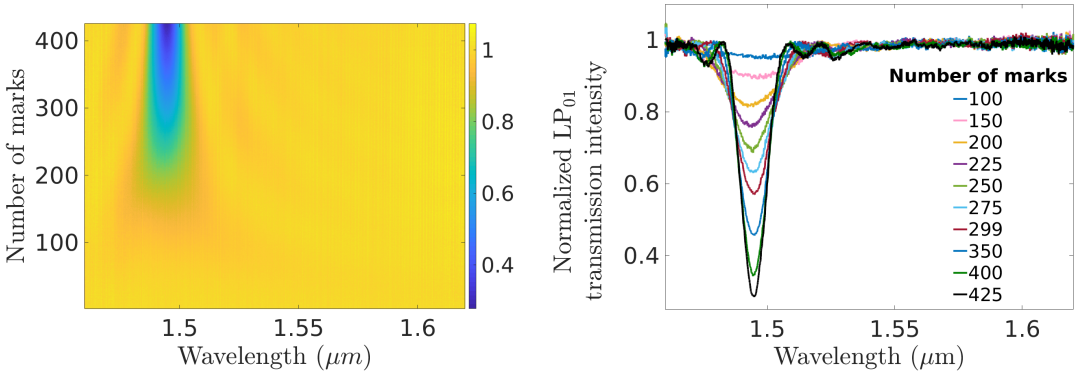

(a) 3D plot of measured MC spectral evolution with number of marks, N. The colorbar represents normalized LP_{01} transmission intensity

(b) Measured evolution of normalized LP_{01} transmission intensity spectrum during MC fabrication, visualized for some chosen marks amongst the full spectral set in figure 6.10a

Figure 6.10 – Example of MC fabrication with stable resonance wavelength.

Since only 70 % conversion happens at 425 marks (Figure 6.10b), the coupling constant is low. The resonance wavelength is at 1.495±0.001 μm. The bandwidth of the first zeros of the conversion peak is 20 nm.

The residual intensity left in a mode after passing through an MC is given by the coupled-mode theory [6; 56; 127]:

$$I_{MC}(\lambda, N, \delta\beta_{MC}(\lambda), \kappa(\lambda), \Lambda_{MC}) = cos^2\big(\xi(\lambda) N \Lambda_{MC}\big) + \frac{\delta^2(\lambda)}{\xi^2(\lambda)} sin^2\big(\xi(\lambda) N \Lambda_{MC}\big) \tag{6.5}$$

where $\kappa(\lambda)$ is the coupling constant arising from mode mixing in the exposed parts and $\delta(\lambda) = \frac{\delta\beta_{MC}(\lambda)}{2} - \frac{\pi}{\Lambda_{MC}}$, and $\xi(\lambda) = \sqrt{\kappa^2(\lambda) + \delta^2(\lambda)}$. κ is generally 3 orders of magnitude smaller than $\frac{\delta\beta_{MC}(\lambda)}{2}$. Even after subtraction with $\frac{\pi}{\Lambda_{MC}}$, $|\frac{\delta\beta_{MC}(\lambda)}{2} - \frac{\pi}{\Lambda_{MC}}|$ dominates $\kappa(\lambda)$ within few 10s of nm on both sides of λ_{MC} (Figure 6.10b). Equation 6.5 says that the strength of the intensity dip, $I(\lambda_{MC}, N)$, in the transmission spectrum of the converted mode will follow a specific trigonometric functionality with N.

$$I(\lambda_{MC}, N) = 1 - A\ sin^2(N \Lambda_{MC} \kappa) \tag{6.6}$$

This information can be used as another method to characterize the stability of the photoinduced effects coming from every mark. To isolate the effect, wavelengths far away from λ_{MC} can be used to characterize the loss with each mark. After correcting the spectrum for loss by normalization, any systematic deviation of the evolution of the transmission dip from equation 6.6 will imply systematic shifts of parameters during the exposure. For example, figure 6.11 shows the evolution of the transmission dip

strength of an overcoupled low-loss MC, which is fitted well with equation 6.6. Since the functionality follows equation 6.6, it is confirmed that every mark has equal effect.

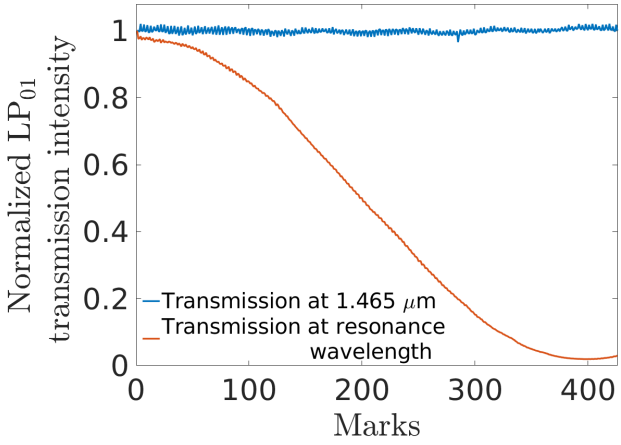

Figure 6.11 – Measured evolution of LP_{01} transmission intensity at λ_{MC} (red curve) and far away from λ_{MC} (blue curve), from the spectra presented in figure 6.10a. The lack of noticeable decay in transmission at the far wavelength showed that the particular irradiation condition induced low loss

The factor A in equation 6.6 is a function of the mark shape and the duty cycle. This becomes important when the extinction-ratio is desired to be high. For the duty cycle of 0.81, the coupling constant at λ_{MC} has a small value of < 31 m^{-1} .

For each irradiation condition, after achieving stable phase extraction from TMI, MCs with repeatable and stable resonance wavelengths were fabricated using different pitches. The collection of resonance wavelengths λ_{MC} from the fabricated MCs, along with the extracted $\Delta\phi(\lambda_{MC})$ and experimentally determined shape of the intermodal dispersion curve (chapter 4) was used to verify the prediction model (equation 6.2) for intermodal dispersion experienced by the fabricated mode converters. The verification with three different duty cycles, with rough estimates of 0.81, 0.2, 0.51 are presented below[1].

6.3.2 Model verification using large duty cycle

The femtosecond setup described in section 5.2.3 was used for large duty cycle, the only changes being (a) having a spot size 95 μm along the fiber axis, and (b) irradiating point-by-point instead of scanning the spot across the fiber. The spot size was roughly estimated from through-focus measurements, taking care to incorporate the fiber cross-section in the optical path, and assuming no self-focusing. Two MCs were fabricated with this spot, one with $\Lambda_{MC} = 117.5$ μm and 5s exposure per mark, and another with $\Lambda_{MC} = 116.5$ μm and 10s exposure per mark. The spectra for both these MCs after writing

[1]Duty cycles can be precisely estimated only if measurements of the refractive index perturbation for a particular mark-writing condition is available, which was not possible with available equipment.

425 marks is shown in figure 6.12, corresponding to maximum achievable conversion. Average phase added per mark was estimated by applying equation 6.4 on unwrapped phase of the TMI recorded during writing of 200 marks with pitch 105 μm, which is illustrated in figure 6.13 for both the exposure times of 5s (solid blue curve) and 10 s (solid red curve). The fitting polynomial was of degree 4 in wavelength.

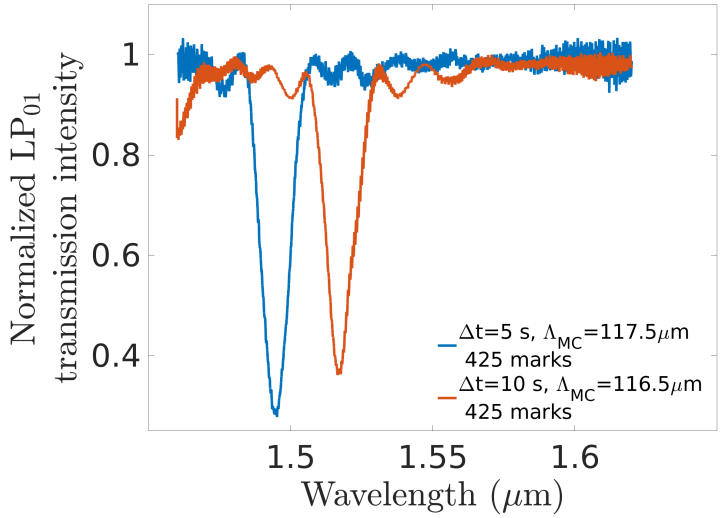

Figure 6.12 – Spectra of the MCs in figure 6.14 for two different exposure conditions (table 6.1), during the maximum conversion for each individual MC

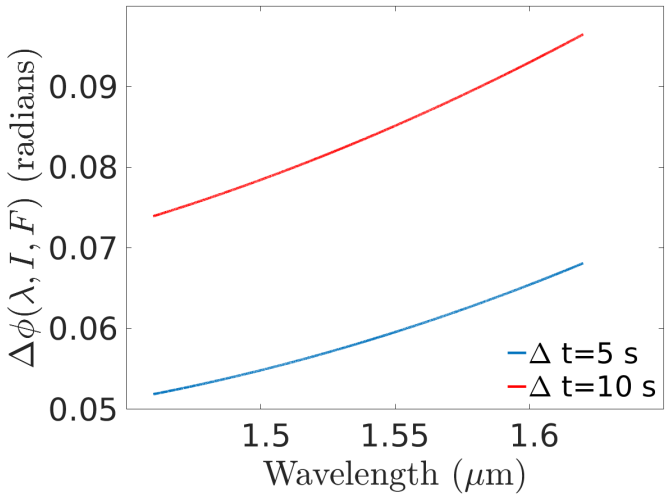

Figure 6.13 – Estimates of extra phase added per mark from 200 marks, using equation 6.4, for total exposure times 5 s (blue curve) and 10 s (red curve) per mark. Exposure conditions are detailed in table 6.1

Figure 6.14 shows the resonances of two MCs for different irradiation conditions and pitch, compared to the predicted $\delta\beta(\lambda)+\frac{\Delta\phi(\lambda,I,F)}{\Lambda_{MC}}$ curves corresponding to the respective irradiation conditions and pitch. The MC with $\Lambda_{MC} = 117.5\ \mu m$ and 5 s exposure time

showed resonance at $\lambda_{MC} = 1.495 \pm 0.001$ μm (green circle in figure 6.14), which was used to fix the offset of $\delta\beta(\lambda)+\frac{\Delta\phi(\lambda,I,F)}{\Lambda_{MC}}$ (solid blue curve in figure 6.14) by matching $\delta\beta(\lambda_{MC})+\frac{\Delta\phi(\lambda_{MC},I,F)}{\Lambda_{MC}} = \frac{2\pi}{\Lambda_{MC}} = \delta\beta_{MC}(\lambda_{MC})$ (equation 6.2), thereby also fixing the offset of the $\delta\beta(\lambda)$ curve (dashed blue curve in figure 6.14). For the other MC fabricated with pitch $\Lambda_{MC} = 116.5$ μm and 10 s exposure time, the measured resonance wavelength (violet cross in figure 6.14) matched the wavelength where predicted $\delta\beta(\lambda)+\frac{\Delta\phi(\lambda,I,F)}{\Lambda_{MC}}$ (solid red curve in figure 6.14) equals $\frac{2\pi}{\Lambda_{MC}}$ within 2 nm, which gives a relative error $< 2 \times 10^{-3}$.

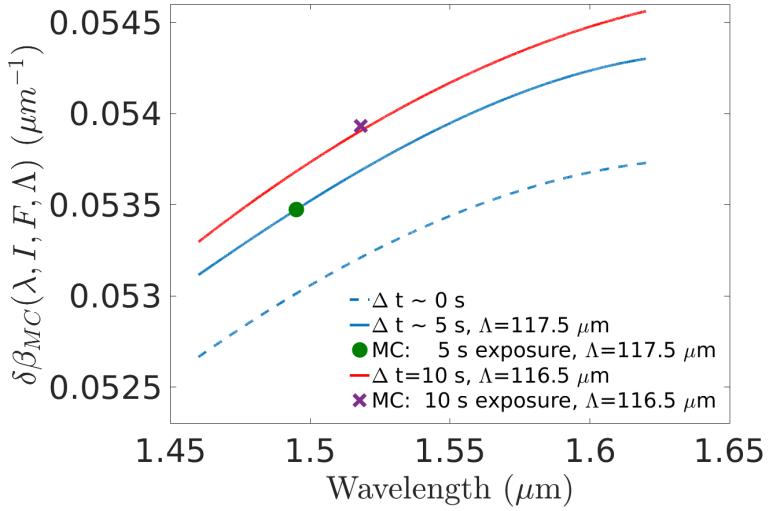

Figure 6.14 – For the case of large duty cycle, the experimental comparison of fabricated MCs for two irradiation conditions with the predicted intermodal dispersion from equation 6.2. Exposure conditions are detailed in table 6.1

In figure 6.14, the possible mismatch for the predicted value for the 10 s exposure of marks (solid red curve) is most likely due to overestimation of $\Delta\phi(\lambda)$ for the 10 s exposure condition, caused by overlap of the large marks (95 μm size) during TMI measurements with pitch 105 μm for measuring $\Delta\phi(\lambda)$. Possibly due to the same overestimation, the offset value of $\delta\beta(\lambda)$ (dashed blue line) has been estimated to a low value, as compared to other estimates presented in table 6.2

6.3.3 Model verification using small duty cycle

Experiments were performed with a small value of the duty cycle of approximately 0.22, using marks with estimated diameter of about 25 μm, fabricated using the femtosecond setup described in section 6.2.1. The spot size was measured using a phase-contrast microscope from the MICROBS laboratory in EPFL. The peak intensity was approximately 9.1×10^{13} Wcm^{-2}. For such a mark size and irradiation condition, MCs were made using exposure time of 5 s per mark. Figure 6.15 shows the spectra of two such MCs with different pitch.

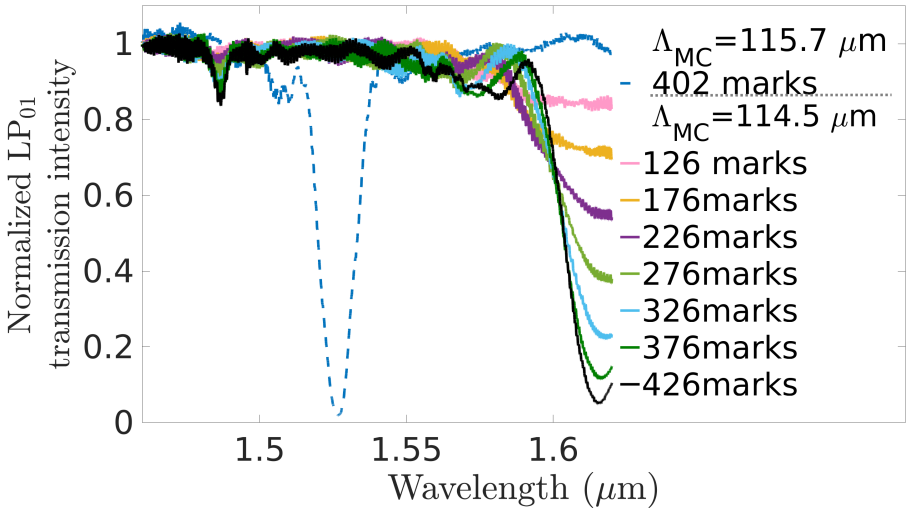

Figure 6.15 – Spectra of two MCs with same exposure conditions and mark size of 25 μm, but different pitch (Exposure details in table 6.1)

The corresponding estimate of average phase added per mark is shown in figure 6.16, obtained by applying equation 6.4 on the unwrapped phase of the TMI recorded while writing 200 marks with pitch 105 μm. The unwrapped phase was fitted with a fourth order polynomial in wavelength.

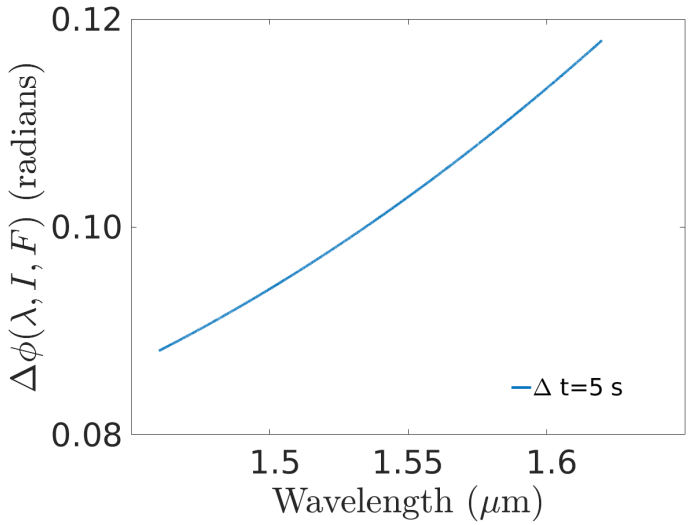

Figure 6.16 – For small duty cycle, estimates of extra phase added per mark from 200 marks, using equation 6.4, for total exposure times 5 s (blue curve). Exposure conditions are detailed in table 6.1

The symbols in figure 6.17 show the intermodal dispersion experienced by two MCs fabricated with different pitch but same irradiation condition corresponding to the

estimated $\Delta\phi(\lambda, I, F)$, at their corresponding resonance wavelengths. The pitch $\Lambda_{MC} = 115.7\ \mu m$ showed resonance at $\lambda_{MC} = 1.527\ \mu$m (green circle in figure 6.17), which was used to fix the offset of $\delta\beta(\lambda)+\frac{\Delta\phi(\lambda,I,F)}{\Lambda_{MC}}$ (solid blue curve in 6.17) by matching $\delta\beta(\lambda_{MC})+\frac{\Delta\phi(\lambda_{MC},I,F)}{\Lambda_{MC}} = \frac{2\pi}{\Lambda_{MC}} = \delta\beta_{MC}(\lambda_{MC})$ (equation 6.2), thereby also fixing the offset of the $\delta\beta(\lambda)$ curve (dashed blue curve in 6.17). The second pitch $\Lambda_{MC} = 114.5\ \mu m$ was chosen since the corresponding resonance wavelength was close to the GVE wavelength and thereby is expected to be highly sensitive to any changes, including changes in the pitch or the offset of $\delta\beta(\lambda)$. From the estimate of $\frac{d\lambda_{MC}}{d\Lambda_{MC}}$ in figure 4.8, near 1.6 μm wavelength, the resonance will shift by 10 nm for a change of 0.1 μm of the pitch. Also from equation 4.7, the resonance wavelength would shift by at least 20 nm for a change of 1 % in the offset of $\delta\beta_{MC}(\lambda)$. Therefore for model verification of equation 6.2, for nearby resonance and GVE wavelengths offer highly stringent conditions.

Caution needs to be followed in determining resonance wavelength close to GVE wavelength from the minima of the MC peak. When these two wavelengths are close, the spectral peaks on two sides of the GVE wavelength overlap, thus decreasing the sharpness of the resonance peak. Therefore sufficient mode coupling needs to be achieved for reliable determination of the resonance wavelength. After reliable determination of the resonance wavelength for $\Lambda_{MC} = 114.5\ \mu m$ from MC peaks with sufficient depth, the experimentally determined value (violet cross in figure 6.17) matches the corresponding prediction using equation 6.2 within 3 nm, which gives a relative error $< 2 \times 10^{-3}$.

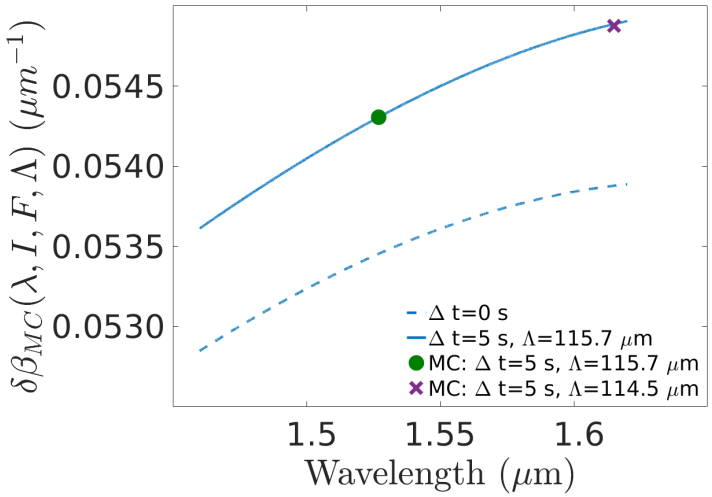

Figure 6.17 – For small duty cycle, the experimental comparison of fabricated MCs with same irradiation conditions but for two different pitches, with the predicted intermodal dispersion (Equation 6.2). The predicted resonance wavelength is only off by 3 nm even while being close to the GVE wavelength. Exposure conditions are detailed in table 6.1

6.3.4 MC fabrication using medium duty cycle

A better control over duty cycle was necessary for both increasing the coupling constant and consequently decreasing the length of the MC, as well as for increasing the maximum extinction ratio. To achieve such control, a commercial laser exposure setup (OPTEC LSV3, described in section 6.2.2) consisting of on online camera and a set of selectable apertures was used for better control of the duty cycle. The online camera also provided both the capability of actively compensating misalignment of the translation stage, and use of high focal spot intensity, whereas high focal spot intensity for the femtosecond laser possibly caused self-focusing which could not be characterized due to lack of imaging resolution in the femtosecond setup (section 6.2.2). Precise control of the mark size and alignment generated MCs with high extinction ratio and repeatable resonance wavelength.

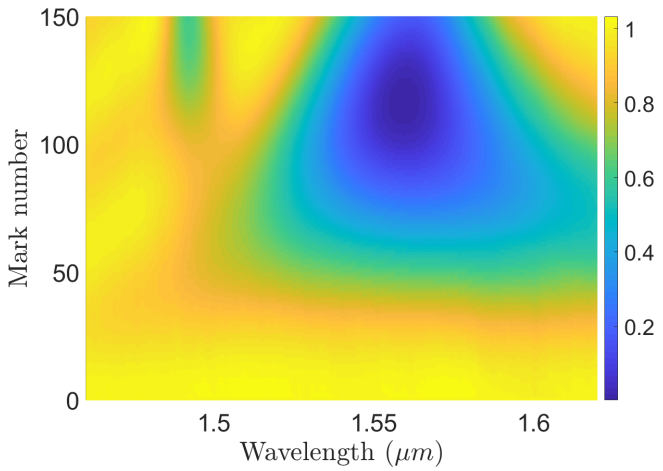

Figure 6.18 – Evolution of measured LP_{01} transmission spectrum while writing resonant marks with 0.51 duty cycle for the LP_{01}-LP_{02} mode pair. The normalized transmission intensity is represented by color. The resonance wavelength was stable within ± 1 nm, implying stability of the alignment and laser parameters. A core-cladding mode resonance [6] was visible at $\lambda \approx 1.49$ μm, which was carefully separated from the LP_{01}-LP_{02} resonance peak by choosing the appropriate combination of pitch, intensity and fluence, through iterations

Figure 6.18 shows the evolution of an MC written with pitch $\Lambda_{MC} = 116$ μm and measured spot size of 59 ± 0.5 μm (measured using the fluorescence recorded under the microscope during exposure), corresponding to duty cycle of 0.51. The laser power and frequency was 150 mW and 200 Hz respectively, and exposure time per mark was 15 s, corresponding to an average intensity of 5486 ± 5 Wcm^{-2} (See table 3.3). Care had to be taken to choose the intensity and fluence for a given pitch, in order to avoid overlap of the core-cladding resonance (dip at $\lambda \approx 1.49\mu$m) with the LP_{01}-LP_{02} MC resonance peak (dip at $\lambda = 1.56$ μm). Although cladding mode simulations or experimentation using changes

in external refractive index could further verify that the dip at $\lambda \approx 1.49$ μm is coming from core-cladding mode resonance, it was evident from the method of elimination. For the used pitch, it was possible to convert only between LP_{01} to LP_{02} core modes in the measured wavelength range. Further, since the LP_{01}-LP_{02} GVE wavelength was outside the measured range, only one LP_{01}-LP_{02} conversion dip was physically possible in this range. Therefore one of the two observed spectral dips (both with resonance wavelengths stable within ±1 nm) must correspond to core-cladding resonance. Due to the vicinity of the LP_{01}-LP_{02} GVE wavelength, the LP_{01}-LP_{02} mode conversion peak was expected to be wide, which established that the dip with larger spectral bandwidth corresponds to LP_{01}-LP_{02} mode conversion, and therefore the other spectral dip corresponded to core-cladding conversion between LP_{01} and an unidentified cladding mode.

To verify repeatability of resonance wavelength and obtaining high extinction ratio, the blue curve in figure 6.19 shows the strongest MC conversion spectrum from figure 6.18, along with the strongest MC conversion spectrum of another exposure with the same conditions (red curve). The grating in figure 6.18 achieved a depth of -28.13 dB at resonance wavelength λ_{MC}=1.56 μm for 117 marks. The second MC a depth of -39.45 dB at λ_{MC}=1.559 μm for 107 marks. Thus λ_{MC} is stable within ±0.1 % between the two gratings, while the coupling coefficient $\kappa(\lambda_{MC})$ varied $\frac{117-107}{117} = 8.5$ % from the first MC to the second. Accordingly $\delta\beta_{MC}(\lambda)$ was within ±0.1 % between the two exposures. Thus $\delta\beta_{MC}(\lambda)$ was resilient while $\kappa(\lambda_{MC})$ was seen to be highly sensitive to misalignment.

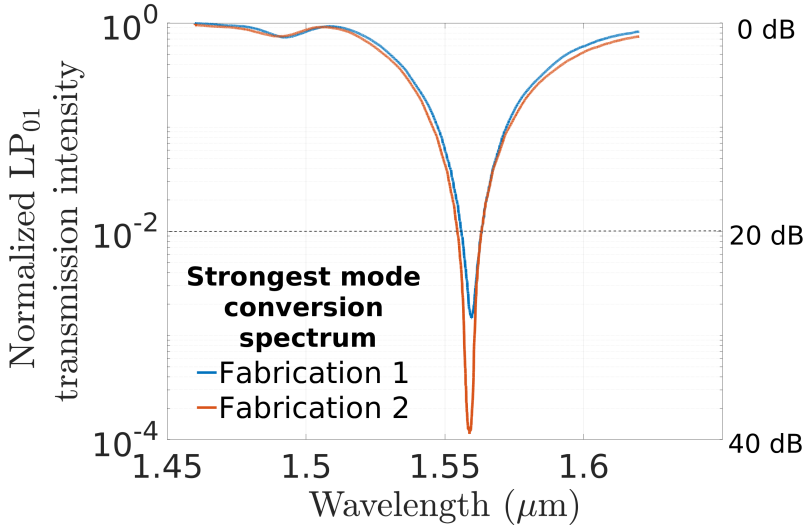

Figure 6.19 – Comparison of measured strongest conversion spectra of two MCs fabricated using the Optec Excimer setup, with same irradiation condition and pitch. Fabrication 1 (blue curve) corresponds to the spectra in figure 6.18. The 20 dB bandwidths are 7 nm and 8 nm for fabrication 1 and 2 respectively. Exposure conditions are detailed in table 6.1

Thus it is experimentally verified that using precise control of duty cycle, strong mode

conversion can be achieved. Similar to the marks written with femtosecond laser, for this irradiation condition average phase added per mark was estimated by applying equation 6.4 on the unwrapped phase of TMI recorded during writing 100 marks with pitch 100 μm, which is shown in 6.20. The fitting polynomial was of degree 4 in wavelength.

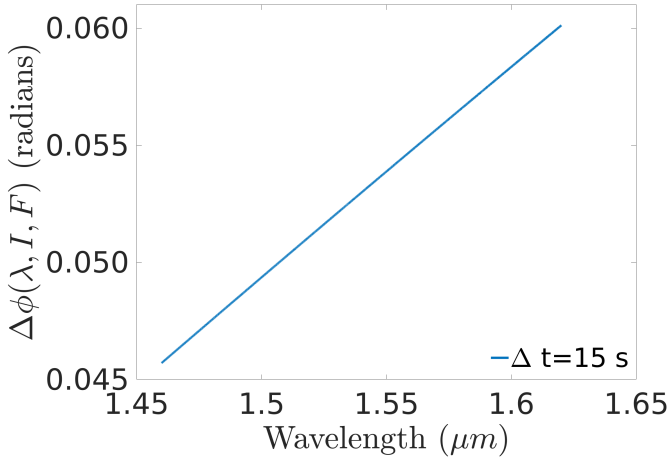

Figure 6.20 – Average phase added per mark between LP_{01} and LP_{02} during mark writing with the Optec Excimer laser, as extracted from experimental data. Exposure conditions are detailed in table 6.1

An MC fabricated using the irradiation condition with estimated $\Delta\phi(\lambda, I, F)$, and pitch $\Lambda_{MC} = 116.0$ μm, showed resonance at wavelength $\lambda_{MC} = 1.560 \pm 0.001$ μm (green circle in figure 6.21). Fixing the offset of $\delta\beta(\lambda) + \frac{\Delta\phi(\lambda,I,F)}{\Lambda_{MC}}$ (solid blue curve in figure 6.21) by matching $\delta\beta(\lambda_{MC}) + \frac{\Delta\phi(\lambda_{MC},I,F)}{\Lambda_{MC}} = \frac{2\pi}{\Lambda_{MC}} = \delta\beta_{MC}(\lambda_{MC})$ (equation 6.2) also fixed the offset of the $\delta\beta(\lambda)$ curve (dashed blue curve in figure 6.21). Although verification of the model was not done with these irradiation conditions for another pitch, the estimated offset of the $\delta\beta(\lambda)$ was used for verifying equation 6.2 by comparing it with the offset estimates from other duty cycles (Table 6.2).

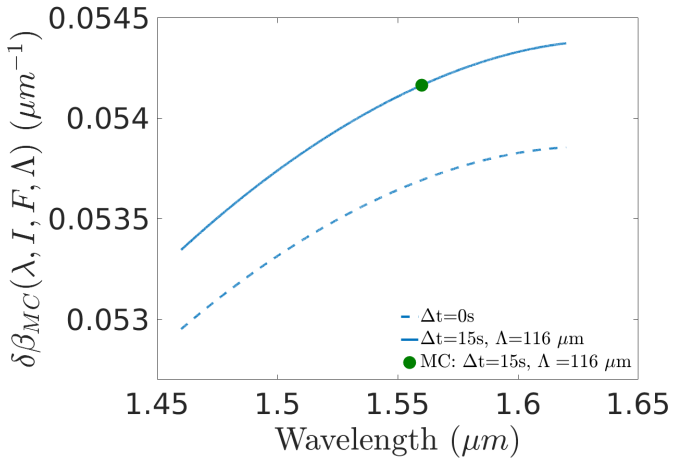

Figure 6.21 – Applying equation 6.2 to the estimated $\Delta\phi(\lambda, I, F)$, shape of $\delta\beta(\lambda)$ from chapter 4, and measured $\delta\beta_{MC}(1.56\ \mu m)$ from an MC made with 0.51 duty cycle (table 6.1), the value of $\delta\beta(1.56\ \mu m)$ was estimated, thereby estimating $\delta\beta(\lambda)$ along with offset. The interpolated value $\delta\beta(\lambda = 1.5422\ \mu m)$ is compared with the estimates from other methods in table 6.2

6.3.5 Summary of fabricated MCs

Table 6.1 summarizes the 5 mode converters reported in this chapter together with the corresponding fabrication parameters and measurement results. I_{peak} refers to peak intensity of the laser. Fluence is the product of average intensity and exposure time. Two MCs were fabricated with different fabrication parameters for both the large and small duty cycles. For each of these duty cycles, one MC was used to estimate the offset of $\delta\beta(\lambda)$ in equation 6.4, whereas the resonance wavelength for the other MC was predicted using the estimated $\Delta\phi(\lambda, I, F)$ for the irradiation condition of the MC together with equation 6.4. For both large and small duty cycles, the predicted resonance wavelengths were within relative error $< 2 \times 10^{-3}$ of the measured valued.

Fig.	Laser	Pitch Λ_{MC}	$\Delta\phi\times$ 100	$\delta\beta_{MC} = \frac{2\pi}{\Lambda_{MC}}$	Mark size	Duty cycle	I_{peak}	Fluence	Measured λ_{MC}	Predicted λ_{MC}	Relative error
		(μm)	(rad)	(μm^{-1})	(μm^2)	≈	(Wcm^{-2})	(Jcm^{-2})	(μm)	(μm)	(%)
6.14	Fs	117.5	5.44	0.05347	95 × 1800	0.81	3.3×10^{11}	1.5×10^2	1.495		
6.14	Fs	116.5	8.07	0.05393	95 × 1800	0.81	3.3×10^{11}	3.0×10^2	1.518	1.521	2×10^{-3}
6.17	Fs	115.7	9.86	0.05431	25×25	0.22	9.1×10^{13}	4.1×10^4	1.527		
6.17	Fs	114.5	11.7	0.05487	25×25	0.22	9.1×10^{13}	4.1×10^4	1.615	1.612	2×10^{-3}
6.21	Optec ArF	116.0	5.48	0.05417	59×59	0.51	9.1×10^9	8.2×10^4	1.560		

Table 6.1 – List of fabricated MCs with corresponding parameters. $\Delta\phi$ represents the value of $\Delta\phi(\lambda, I, F)$ at the resonance wavelength. Table 3.3 lists the properties of the lasers

6.3.6 Summary of different estimates of $\delta\beta(\lambda)$ at a fixed wavelength

Other than accurate prediction of the MC resonance wavelengths, another verification of equation 6.2 can be done by comparing different estimates of $\delta\beta(\lambda)$ at some chosen λ for different duty cycles. Under the assumptions that (a) the pristine fiber has consistent transverse index profile over the whole length of the fiber, and (b) the marks are not overlapping, the estimates should be close in value. Table 6.2 presents estimates of $\delta\beta(1.5422\ \mu\text{m})$ for large (≈ 0.81), small (≈ 0.20), and medium (≈ 0.51) duty cycle using equation 6.2, as well as the estimate from FBG resonance wavelengths reported in section 4.4 under the rough assumption that the effective indices of LP_{01} and LP_{02} are constant in the interval $\lambda = 1.5422 \pm 0.007\ \mu$m.

Fig.	Method	Laser	Pitch	Mark size	Duty cycle	I_{peak}	Fluence	$\delta\beta(\overline{\lambda})$	Relative error
			(μm)	(μm×μm)	≈	(Wcm^{-2})	(Jcm^{-2})	(μm^{-1})	(%)
6.14	MC+TMI	Fs	117.5	95×1800	0.81	3.3×10^{11}	1.5×10^{2}	0.05339	0.32
6.17	MC+TMI	Fs	115.7	25 × 25	0.22	9.1×10^{13}	4.1×10^{4}	0.05356	0
6.21	MC+TMI	Optec ArF	116.0	59 × 59	0.51	9.1×10^{9}	8.2×10^{4}	0.05360	0.07
4.2	FBG	Coherent ArF	0.530	–	–	10×10^{6}	900	0.0531	0.8

Table 6.2 – Comparison of $\delta\beta(\lambda)$ estimates for the pristine fiber at $\overline{\lambda} = 1.5422$ μm using different measurement conditions and methods. The estimate for duty cycle ≈ 0.22 (highlighted in orange) was chosen as the best candidate, since it predicted resonance wavelength accurately even in close vicinity of the GVE wavelength (Figure 6.17). I_{peak} refers to peak intensity of the laser. Fluence is the product of average intensity and exposure time. Table 3.3 lists the properties of the lasers

Duty cycle of 0.51 and 0.22 were expected to give similar estimates, since the overlapping of marks was definitely avoided in these cases during the corresponding TMI experiments to measure $\Delta\phi(\lambda, I, F)$. Indeed the estimates differed only by a small ratio of 0.07 %, whereas the estimate for large duty cycle of 0.81 was off by 0.32 %. The likely cause for such a large error in this case was that the marks were overlapping while TMI fringe shift was measured with a pitch of 105 μm, leading to systematic overshooting for the determination of $\Delta\phi(\lambda, I, F)$. The estimate from FBG resonance wavelengths was off by 0.8 %, which is justified since this particular estimate is made under the rough approximation that the intermodal effective index is constant in the interval $\lambda = 1.5422 \pm 0.007$ μm and therefore not expected to be very precise.

6.4 Conclusions

This novel method establishes a way to predict the resonance wavelength of MCs under any fixed irradiation condition with high accuracy. It provides two precise measurements:

- Offset of the intermodal dispersion curve of the pristine fiber
- Intermodal dispersion curve experienced by an irradiated MC

These two parameters define the differential phase gathered by the two corresponding modes as they co-propagate through the pristine fiber and the MC, respectively. As shown in chapter 7, the knowledge of these phases allows fabrication of broadband MCs by concatenation of MC segments with controlled gaps. The increase of bandwidth is achieved by the interplay of the MC coupling constant, MC phase and the fiber phase.

7 Broadband mode converters

7.1 Introduction

Controllable injection and exchange of power between modes, at desired locations of the fiber and over a broad wavelength range, are of high research and technical interest. The applications vary from space-division-multiplexing [128], dispersion control [29], vortex generation [62] to femtosecond laser operation [129; 130]. In the context of telecommunications and lasers, broadband generally implies covering the amplifier bandwidth for the communication or laser system, e.g. the C-bandwidth (1535 nm-1560 nm) of the EDFA amplifiers [26; 27]. For MDM applications, large bandwidth at an extinction ratio of 20 dB is desired [31].

Multiple technical solutions for broadband selective excitation of modes in an FMF are already available, e.g. by using (a) free-space phase plates [131; 132], (b) photonic lanterns [133; 134], (c) multi-mode interference [135], (d) mode-selective coupler [136; 137; 138; 139] etc.

In contrast, the reported methods of broadband high-extinction MC fabrication using laser irradiation inside a fiber is limited. For example, 63 nm bandwidth was achieved at an extinction ratio of 20 dB by superposition of two resonance peaks on both sides of the GVE wavelength [31]. Although the performance is excellent, versatility is lacking because the GVE wavelengths are inherent parameters of the fiber and can be hundreds of nm apart from the wavelengths of interest. As for controlled mode excitation, multi-mode interference effect has been successfully used, for example by introducing a precisely offset multi-mode fiber between two cleaved ends of a two-mode fiber [140]. The multimode fiber effectively worked as a phase segment for the FMF and converted 38 % power from LP_{01}-LP_{11} over 100 nm bandwidth, with 30 dB extinction ratio. Beyond the complexity of the setup and the limited scope of only using two-mode fiber, such a device also acts as a mode excitation apparatus, and not as a mode converter in the strict sense inside the few-mode fiber. Recently a lot of research projects have been performed in the search

of general methods to fabricate broadband mode converters [36; 40]. In the search of more general and simple methods for broadband high-extinction mode conversion inside the few-mode fiber, this thesis evaluated two other grating-based methods:

- **Partial-core irradiation:** Increasing the coupling between desired modes by irradiating partial core, or by strong uniform irradiation.
- **Phase-shifted gratings:** Simultaneously deepening the side bands of the MC resonance together with the central band, by introducing controlled phase shifts in the grating.

The physical limitations and technical issues of both the methods are discussed in detail in this chapter. Moreover, experimental verification of the phase-shifted broadband MCs is presented.

7.2 Partial-core irradiation

7.2.1 Motivation

It is well known from free-space optics that end-to-end coupling of higher-order LP modes from LP_{01} mode is possible by introducing phase plates which match the phase of the higher-order mode [131; 132; 140]. The free-space phase plates for increasing the coupling to different higher-order modes are illustrated in figure 7.1.

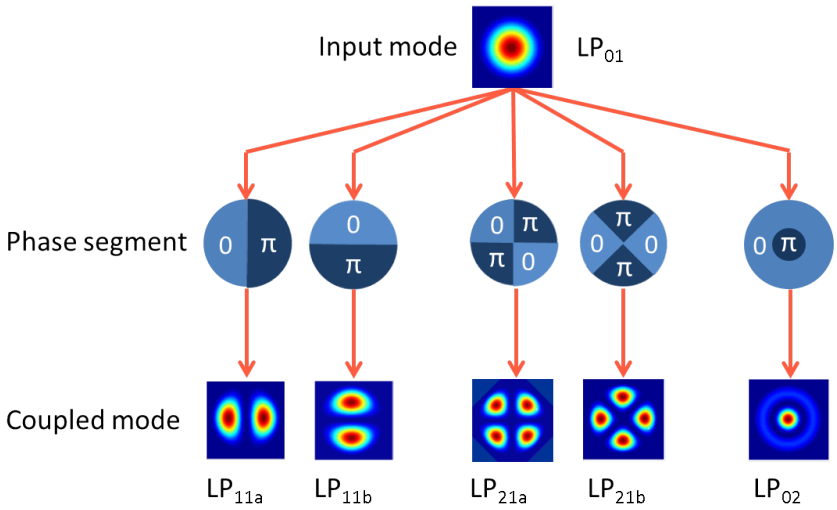

Figure 7.1 – Free-space phase plates for increasing the coupling from LP_{01} to higher order $LP_{m,l}$ modes in a four-mode fiber

Similar idea was evaluated for in-fiber situation via simulations for partial core irradiation. In figure 7.2, deep blue part of the core represents irradiated part of the core, which

gained an extra effective index of Δn_e. The length L of such a segment should be such that $\Delta n_e \; L = \lambda/2$, or equivalently $\Delta\beta(\lambda) \; L = \pi$ at the desired conversion wavelength λ [140]. Equivalently, the partially irradiated core in figure 7.2 of length L would have mode conversion at a central wavelength which satisfies $\Delta n_e \; L = \lambda/2$. However linear modeling of two channels establishes that for strong conversion from a single segment, the coupling ratio between the two different channels and the unperturbed fiber at both ends of the segment has to be close to 1:1, thereby introducing additional fabrication requirements.

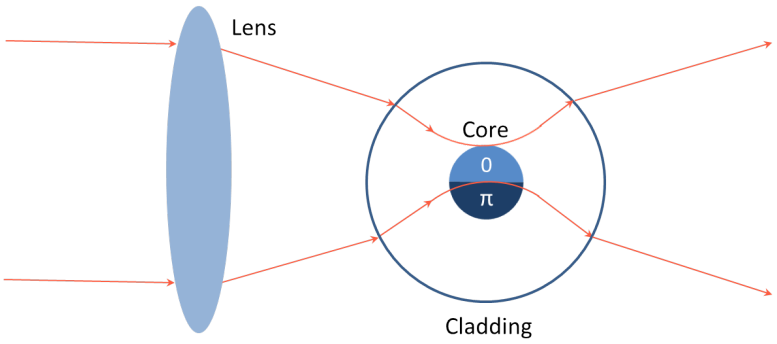

Figure 7.2 – Schematic for writing $0-\pi$ phase segment inside a few-mode fiber using laser irradiation

7.2.2 Simulation method

The index change due to laser exposure is simulated by changing the GeO_2 concentration in the considered segment of the core. Figure 7.3 shows the refractive index difference between the core and cladding, for different values of GeO_2 concentration of the core. The ratio of GeO_2 concentration between the upper and lower halves of the cores is designated as doping ratio. Doping ratio of up to 1.5 is considered. Doping ratio corresponding to higher refractive index changes are hard to achieve with laser irradiation, without inducing losses in the fiber.

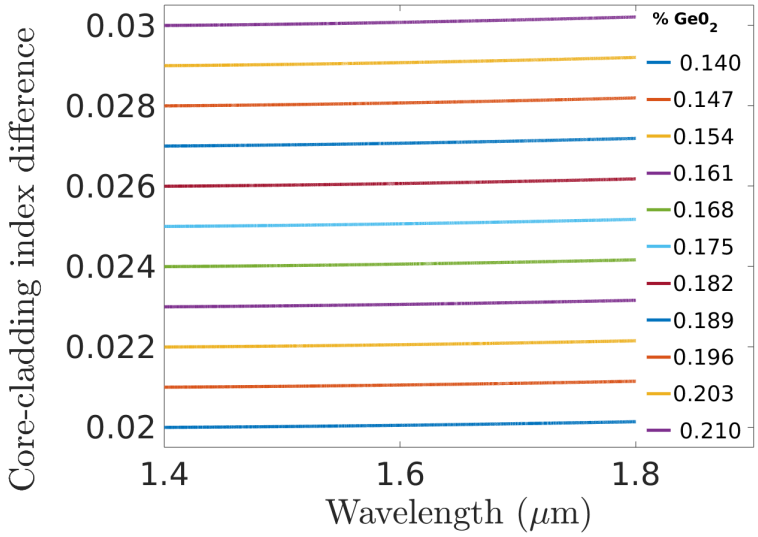

Figure 7.3 – Core-cladding refractive index difference for different GeO_2 doping represented by lines of different colors. These calculations were done using Sellmeier coefficients for SiO_2 and GeO_2 (table 3.1) and equation 3.1

For feasible simulations with available software, the MC is approximated by discrete marks of constant index profile along the fiber axis [46]. The intermodal phase per pitch experienced by an MC with pitch Λ_{MC} and duty cycle f is given by [1]

$$\Lambda_{MC}\delta\beta_{MC}(\lambda) = (1-f)\Lambda_{MC}\delta\beta(\lambda) + f\ \Lambda_{MC}\Big(\delta\beta(\lambda) + \Delta\delta\beta(\lambda)\Big)$$

$$\implies \delta\beta_{MC}(\lambda) = \delta\beta(\lambda) + f\ \Delta\delta\beta(\lambda) \tag{7.1}$$

where $\delta\beta(\lambda)$ is the intermodal dispersion curve of the pristine fiber, $\Delta\delta\beta(\lambda)$ is the extra intermodal dispersion introduced by irradiation in the mark region, and $\delta\beta_{MC}(\lambda)$ in the average intermodal dispersion per period length (equation 2.36). The best conversion is achieved at duty cycle f=0.5 [70]. If such a parameter value is maintained, the MC will experience an intermodal dispersion curve $\delta\beta_{MC}(\lambda) \approx \delta\beta(\lambda) + \frac{\Delta\delta\beta(\lambda)}{2}$. In that case approximately twice the index change, corresponding to $2|\delta\beta_{MC}(\lambda) - \delta\beta(\lambda)|$ is necessary to get the desired intermodal dispersion curve (Figure 7.6).

If the resonance wavelength is kept fixed and away from the GVE wavelength, the bandwidth of an MC increases as (a) the intermodal dispersion curve becomes flatter and (b) the coupling ratio introduced by the mark becomes larger (which is equivalent to writing shorter mode converters) [35]. The meaning of "flatter" is to have small values

[1] Equation 6.3 can incorporate complex mark profiles, and is more general than equation 7.1. The latter is a particular case of equation 6.3, if the refractive index perturbation in a mark is exactly uniform along the fiber axis. Since available software could only solve modes of 2-D structures, such a simplification was necessary.

for both the first and second derivative on the intermodal dispersion with respect to wavelength.

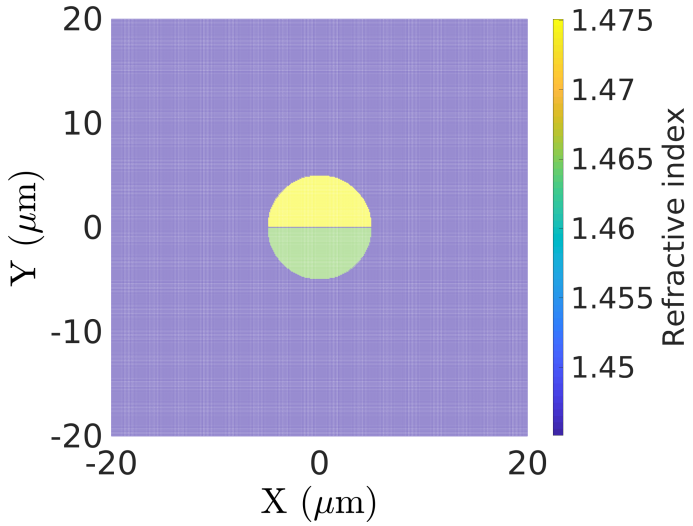

Figure 7.4 – Simplified model for simulation of in-fiber phase segment, consisting of two semi-circular regions (D1 and D2) in the cross-section of the core with different refractive indices. The colorbar represents refractive indices at 1.55 μm wavelength

For the simulation, a simple model of exactly half of the step-index core having a different uniform refractive index was used, which is illustrated in figure 7.4. The GeO_2 concentration is changed for the upper semi-circular half in figure 7.4, while it is kept fixed in the lower half of the core, thereby changing the GeO_2 doping ratio. Naturally, the doping ratio equals 1 when the core is uniform, corresponding to a standard step-index fiber.

PDETool, the graphical-user-interface in Matlab for numerically solving partial differential equations, was used to solve the finite element approximation of the Helmholtz eigenvalue problem with different coefficients in the two halves of the core corresponding to the different refractive indices. After creating a model for the partial differential equation, the following conditions were chosen in order to ensure reliable mode-solving: (a) the mesh length was set sufficiently small (0.1 μm), (b)the tolerances for determining convergence of the numerical algorithm was set to be sufficiently small (model.SolverOptions.AbsoluteTolerance=1.0e-32; model.SolverOptions.RelativeTolerance=1.0e-32; model.SolverOptions.ResidualTolerance=1.0e-32;), and (c) the simulation domain was taken to be large compared to the core size, so that the tails of the modes go below the arithmetic precision of Matlab. For example, the radius of the simulated circular domain was 62.5 μm. These parameters were determined by comparing the simulated eigenvalues $\beta_x(\lambda)$ of a step-index profile with the exact dispersion equations of the LP modes.

7.2.3 Simulation results

The simulation range was from 1 to 1.5 for the GeO_2 doping ratio between the upper and lower halves of the core in figure 7.4, in 5 equal steps of index change. The mode profiles for 1.5 GeO_2 doping ratio between the two halves of the core are shown in figure 7.5.

The location of the GVE wavelength is more important for the bandwidth of the MC than the absolute value of intermodal dispersion. Thus for simulating the modes of the semicircular segments, the GeO_2 doping of the lower half in 7.4 was set to be 13.7 %, such that the simulated LP_{01}-LP_{02} GVE wavelength for the pristine fiber matched the measured value. For this GeO_2 concentration for a step-index fiber (Doping ratio of 1) of radius 5.0 μm, the LP_{01}-LP_{02} GVE wavelength was simulated to be 1.636 μm.

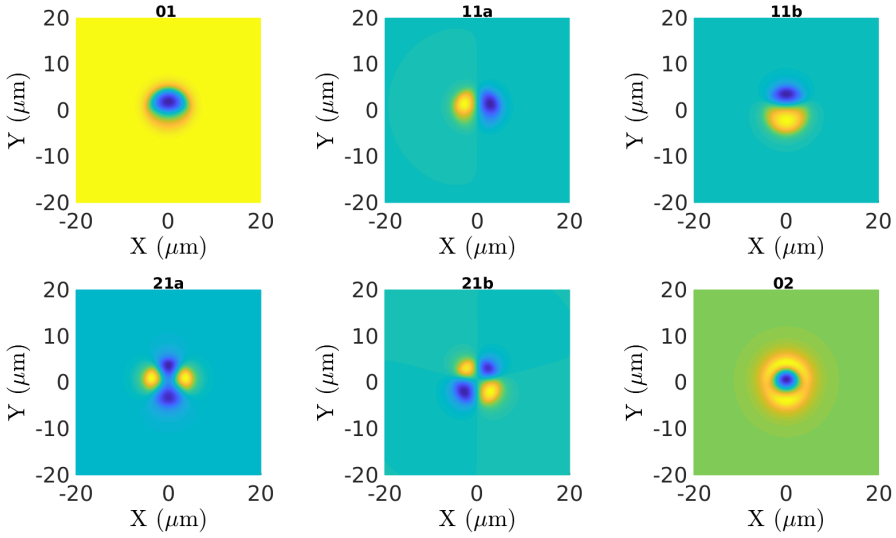

Figure 7.5 – Simulated LP mode profiles for a 1.5 GeO_2 doping ratio between the two halves of the core. The GeO_2 concentration was 13.7 % in the lower half of the cross-section of the fiber core (D2 in figure 7.4). These simulations were performed using finite element method, with the help of PDETool package in Matlab

The mode pairs $LP_{01} - LP_{11a}$, $LP_{01} - LP_{21b}$, $LP_{11a} - LP_{21a}$, $LP_{11b} - LP_{21b}$, $LP_{11a} - LP_{02}$ and $LP_{21b} - LP_{02}$ have zero overlap and thus cannot have mode conversion between the modes in each of these pairs. For different mode pairs which can have mode conversion, the intermodal dispersion in the exposed region are shown in individual panels of figures 7.6, for different GeO_2 doping ratio between the two halves of the core.

Only the $LP_{01} - LP_{11b}$ (figure 7.6) intermodal dispersion curves seems to be flat, albeit for a very high index change of 0.01 in half of the core, corresponding to 1.5 GeO_2 doping ratio between the two halves of the core. This is quite hard to achieve with only laser irradiation in germano-silicate fibers, without introducing loss.

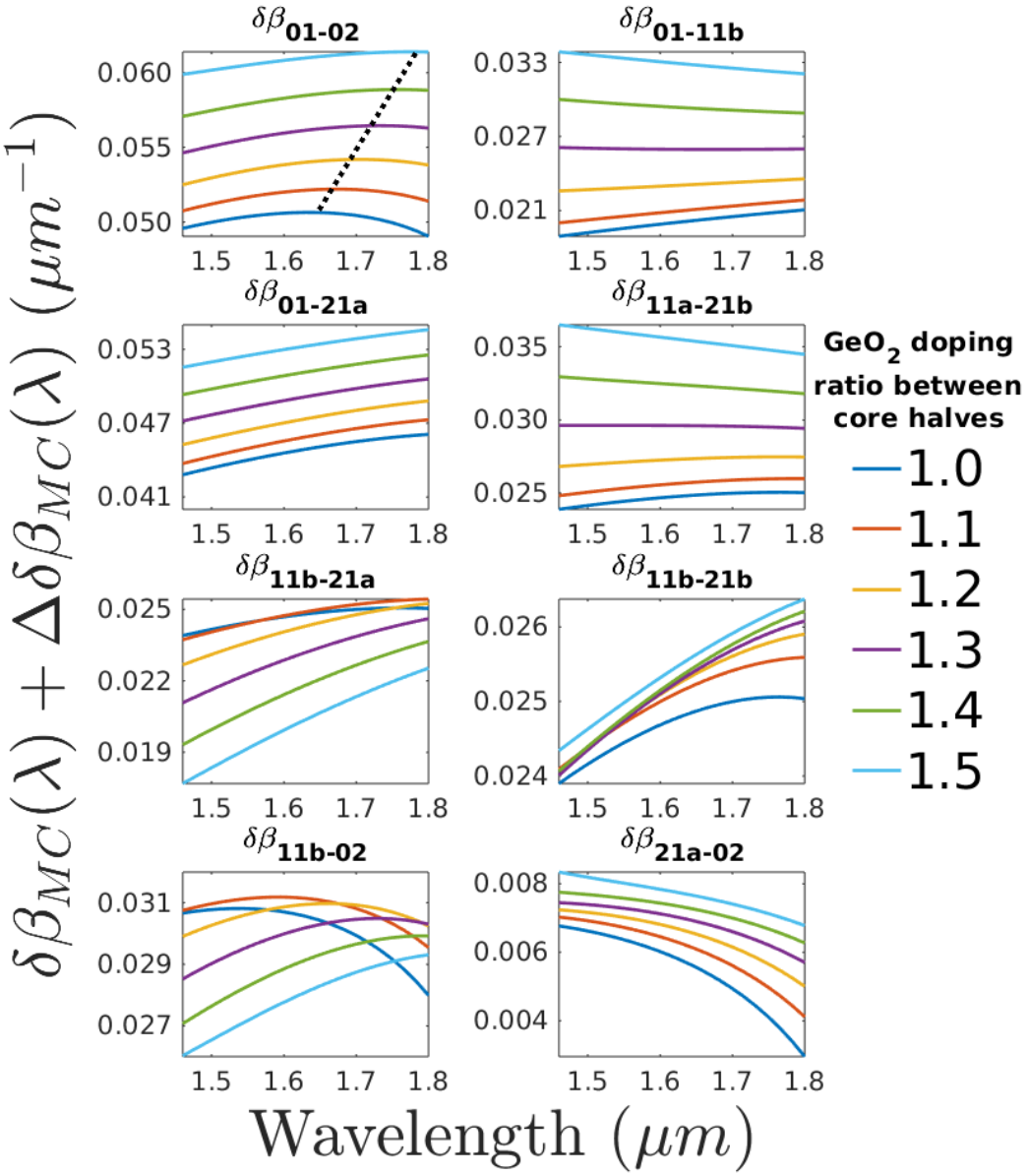

Figure 7.6 – Simulated intermodal dispersion for different mode pairs of homogeneous semicircular phase segment waveguides, plotted as a function of GeO_2 doping ratio between the two halves of the core. The dotted black line in the top left panel represents the shift of GVE wavelength with varying GeO_2 doping ratio

Figure 7.7 shows the intermodal dispersion for different mode pairs for 1.5 GeO_2 doping ratio between the two halves of the core, which is achievable using UV irradiation of a hydrogen-loaded fiber [141; 142]. At 1.5 GeO_2 doping ratio between the two halves of the core, 0.5 duty cycle and $\Lambda_{MC} = \frac{2\pi}{0.02645}$ μm = 237.5 μm can give broadband mode conversion due to flatness of the $LP_{01} - LP_{11b}$ intermodal dispersion curve experienced

by the MC. At the same conditions, there seems to be two intersections of intermodal dispersion curves : one at λ<1.46 μm {$LP_{01} - LP_{11b}$ and $LP_{11b} - LP_{02}$}, and another at λ>1.75 μm {$LP_{01} - LP_{11b}$ and $LP_{11b} - LP_{21b}$} (However $LP_{11b} - LP_{21b}$ conversion cannot occur due to symmetry and therefore can be ignored for the consideration). Although in the simulated case the intersection wavelengths are far way from the C-band to cause problems, for smaller changes in index the intersection can be close to the C-band (Figure 7.6), resulting in simultaneous power conversion for both the mode pairs. Such a situation will result in a complex case of mode mixing. The presence of GVE wavelengths in the simulated range also offer potential for broadening the MC spectrum by overlapping the spectral peaks on both sides of the GVE wavelength [31]. As illustrated in figure 7.7, the mode pairs $LP_{01} - LP_{02}$, $LP_{11a} - LP_{21b}$ and $LP_{11b} - LP_{02}$ have GVE wavelengths at 1.676 μm, 1.507 μm and 1.669 μm respectively. The only quantity still left unverified for the mode conversion is the loss from such a device, which will be analyzed next by simulating the mode conversion spectra.

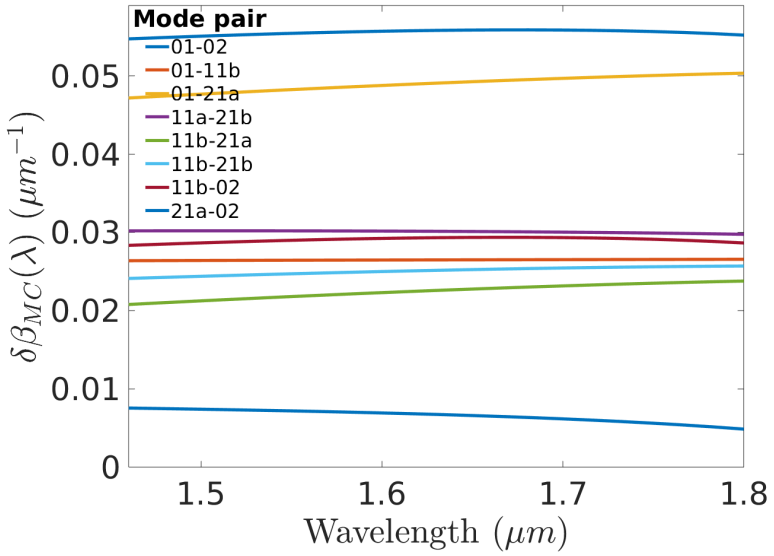

Figure 7.7 – Simulated $\delta\beta_{MC}(\lambda) = \delta\beta_{MC}(\lambda) + f\Delta\delta\beta_{MC}(\lambda)$, for different mode pairs for a duty cycle $f = 0.5$, and 1.5 GeO_2 doping ratio between the two halves of the core

The coupling at the boundaries of the discrete segments was calculated using the overlap integrals of the modes of the irradiated and unirradiated segments, both individually normalized with respect to their energy. Figure 7.8 shows the overlap integrals of LP_{01} of the unperturbed fiber with {$LP_{01'}$,LP_{11b^*},LP_{21a^*},LP_{02^*}} modes of the irradiated segment. Assuming the bandwidth to be proportional to the bandwidth of the first zeros $\lambda_{\pm1}$ of the LP_{01}-LP_{01^*} transmission, it is possible to estimate the ratio of increase in bandwidth with the GeO_2 doping ratio between the two halves. Under a first order approximation of $\kappa(\lambda_{MC}) = \kappa(\lambda_{\pm1})$, the bandwidth of the first zeros is given by $\Delta\lambda = \lambda_{+1} - \lambda_{-1} = \frac{2\sqrt{3}\lambda_{MC}\kappa(\lambda_{MC})}{\pi}$ [35]. This requires correlating an index change due to irradiation with $\kappa(\lambda_{MC})$, which

is a function of the overlap integrals at the boundaries of the irradiated segments. The simulated functionality of the overlap integrals with index change is shown is figure 7.8.

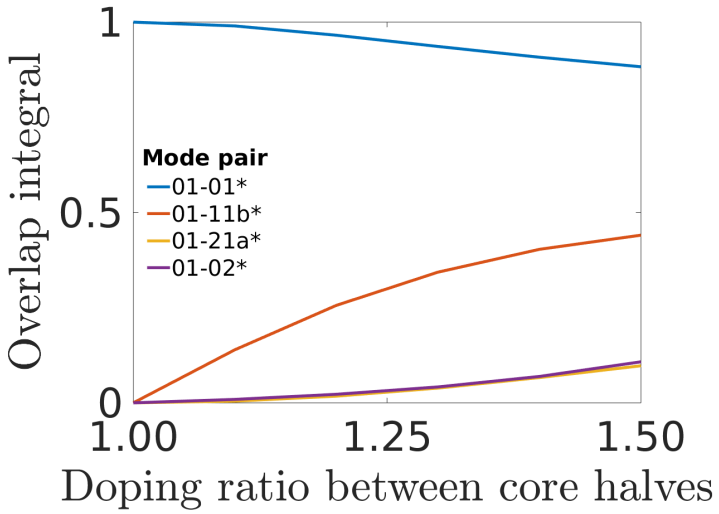

Figure 7.8 – Simulated overlap integrals of LP_{01} of pristine fiber to $LP_{m,l}$ modes of the irradiated segment (denoted by *) as function of GeO_2 doping ratio between the two halves of the core

However, this analysis was not carried forward since the segment based model introduced too much loss due to poor mode overlap at the boundaries of the irradiated segments (Figure 7.9). Is was ascertained that the loss is not arising from the discrete segment model, since the loss at a segment boundary using Fresnel equations give $(\frac{1.47-1.46}{1.47+1.46})^2 < 10^{-4}$. Smooth index profile along the transverse and fiber axis might introduce lower loss [143], which could not be simulated due to Matlab *PDETool* giving spurious results for such profiles.

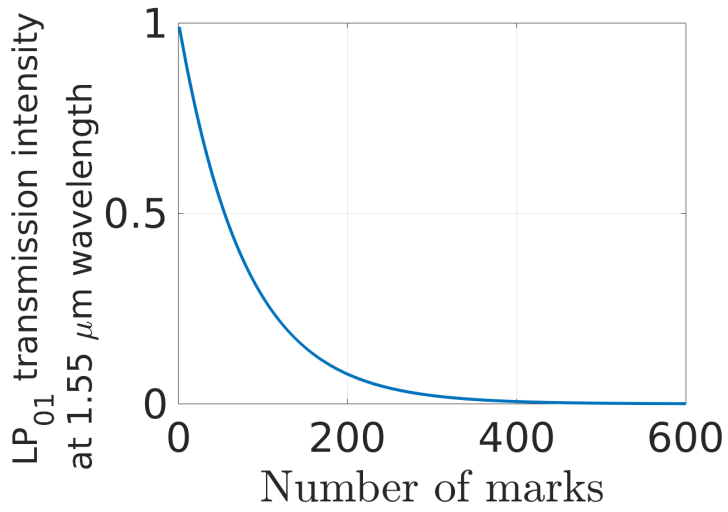

Figure 7.9 – Simulated transmission of LP_{01} at 1.55 μm wavelength during writing of marks with 0.5 duty cycle, pitch $\Lambda_{MC} = \frac{2\pi}{0.02645}$ μm, corresponding to the irradiation conditions of figure 7.7. Similar high loss is simulated in the whole wavelength range of 1.46 μm-1.62 μm

Due to the anticipated loss, a new method of MC segments with phase shifts was developed.

7.3 Phase-shifted MC

Broadening the bandwidth of MC gratings using phase shifts was first proposed in 2005 [35]. The analysis was based on the assumption that the coupling constant $\kappa(\lambda)$ was wavelength independent, as well as arithmetic progression was used for the number of periods in every segment. By following exactly this recipe, (a) 120 nm broadband mode converters were made at an extinction ratio of 20 dB in polymer two-mode waveguide [144], and (b) 116 nm wide broad MC in two-mode fiber at an extinction ratio of 15 dB using CO_2 laser irradiation [145]. However, there is no report of broadband phase-shifted MC at 20 dB extinction ratio in few-mode fibers. This chapter presents a general recipe and experimental verification for fabricating high-extinction broadband MCs in few-mode fibers, made using local marks with some kind of controlled perturbation e.g. exposure with UV laser spot.

A "segment" starts off with a mark, followed by consecutive periodic marks separated by length Λ_{MC} until a deliberately implemented breakage of the periodicity. The length of a segment containing N number of marks is defined as $N\Lambda_{MC}$. The distance between two marks, one at the end of one segment and another at the beginning of the consecutive segment, is different than Λ_{MC}. Instead of either skipping some length after every segment [35] or having a mixture of skipping and adding extra gaps after different segments [144],

it makes more sense from practical perspective to introduce extra gap after every segment in a few-mode fiber [145]. This is because skipping lengths can cause overlap of the marks written in a few-mode fiber, thus changing the phase between segments to an unexpected value. This work dealt with two methods, appropriate for different conditions-

- In the general case when $\kappa(\lambda)$ is not large, using three segments containing N_1,N_2 and N_3 complete periods, with gaps of length $\frac{\pi}{\delta\beta_{MC}(\lambda_{MC})}$ introduced between the segments [35; 144].

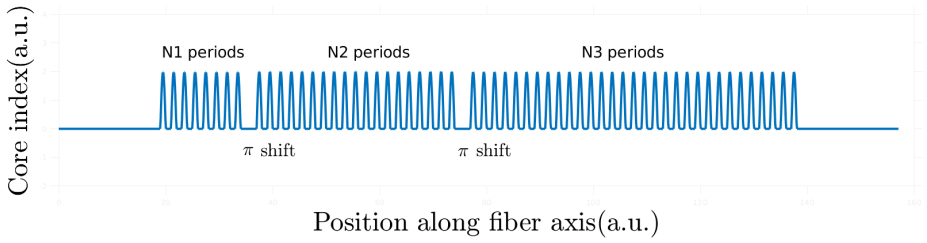

Figure 7.10 – Schematic of phase shifted gratings with three segments

- In the particular case when $\kappa(\lambda)$ is large, using the novel idea of only two segments containing N_1 and N_2 complete periods, with a gap of length $\frac{\pi}{\delta\beta_{MC}(\lambda_{MC})}$ introduced between the two segments.

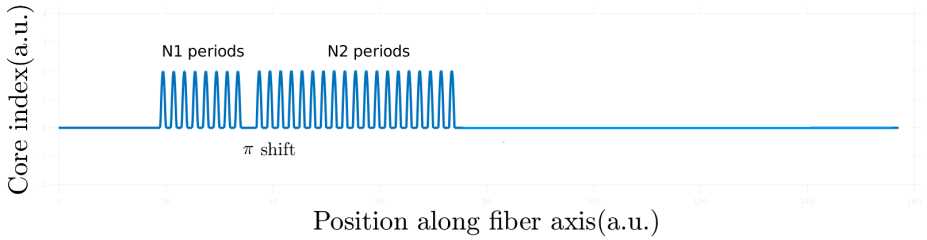

Figure 7.11 – Schematic of phase shifted gratings with two segments

For both the cases, the MC period and gap for the resonance wavelength λ_{MC} was determined from the method described in chapter 6, using complementary TMI measurements.

7.3.1 Modelling of phase-shifted MC

In the general case of N segments with the j^{th} segment contains N_j number of MC periods, along with fixed extra gap of Λ_s introduced after each segment, the lossless

conversion of power between the two modes is given by $|\frac{E_1(\lambda,\Lambda)}{E_2(\lambda,\Lambda)}|^2$, where

$$\begin{bmatrix} E_1(\lambda,\Lambda) \\ E_2(\lambda,\Lambda) \end{bmatrix} = \left[\Pi_{j=0}^{N} \begin{bmatrix} e^{i\frac{\delta\beta(\lambda)\Lambda_s}{2}} & 0 \\ 0 & e^{-i\frac{\delta\beta(\lambda)\Lambda_s}{2}} \end{bmatrix} M^{N_j}\right] \begin{bmatrix} E_1(\lambda,0) \\ E_2(\lambda,0) \end{bmatrix} \tag{7.2}$$

where N_j is the number of marks for j^{th} segment, and M is the conversion matrix for the complex mode amplitudes for a single MC period (Described in chapter 2.1.6).

Although often $\kappa(\lambda)$ is assumed to be constant, as in references [35; 144; 145], in reality it is a function of wavelength. This has to be considered when the MC bandwidth is large. The bandwidth of phase-shifted MCs can be especially large when $\delta\beta_{MC}(\lambda)$ is very flat, for example near the GVE wavelength. This is the case for the mode combination LP_{01}-LP_{02} presented in this chapter, which necessitated estimation of $\kappa(\lambda)$.

For stable irradiation and alignment conditions, estimation of $\kappa(\lambda)$ using two segments can be understood analytically

$$\begin{bmatrix} E_1(\lambda,\Lambda_{MC}(N_1+N_2)+\Lambda_s) \\ E_2(\lambda,\Lambda_{MC}(N_1+N_2)+\Lambda_s) \end{bmatrix} = M(\lambda,N_2) \begin{bmatrix} e^{i\frac{\delta\beta(\lambda)\Lambda_s}{2}} & 0 \\ 0 & e^{-i\frac{\delta\beta(\lambda)\Lambda_s}{2}} \end{bmatrix} M(\lambda,N_1) \begin{bmatrix} E_1(\lambda,0) \\ E_2(\lambda,0) \end{bmatrix} \tag{7.3}$$

Following matrix multiplication rules and representing $M(\lambda,N) = \begin{bmatrix} M_{11}(\lambda,N) & M_{12}(\lambda,N) \\ M_{21}(\lambda,N) & M_{22}(\lambda,N) \end{bmatrix}$ gives the LP_{01} transmission through the single phase shifted mode converter to be

$$|\frac{E_1(\lambda,\Lambda_{MC}(N_1+N_2)+\Lambda_s)}{E_1(\lambda,0)}| = |M_{11}(\lambda,N_2)M_{11}(\lambda,N_1) + e^{i\delta\beta(\lambda)\Lambda_s}M_{12}(\lambda,N_2)M_{22}(\lambda,N_1)| \tag{7.4}$$

Thus presence of two strong dips in the transmission at wavelengths $\lambda_{-1} < \lambda_{MC} < \lambda_{+1}$, corresponding to $|\frac{E_1(\lambda_{\pm1},\Lambda_{MC}(N_1+N_2)+\Lambda_s)}{E_1(\lambda_{\pm1},0)}| \approx 0$, give the relation:

$$\frac{M_{11}(\lambda_{\pm1},N_2)M_{11}(\lambda_{\pm1},N_1)}{M_{12}(\lambda_{\pm1},N_2)M_{22}(\lambda_{\pm1},N_1)} = +e^{i\left(\pi+\delta\beta(\lambda_{\pm1})\Lambda_s\right)} \tag{7.5}$$

Since the only undetermined quantity at this point in $M(\lambda,N)$ is $\kappa(\lambda)$, trying different values of $\kappa(\lambda_{\pm1})$ in the vicinity of $\kappa(\lambda_{MC})$ can be used to satisfy equation 7.5. For weak

conversion peaks at $\lambda_{\pm 1}$, quadratic functionality of $\kappa(\lambda)$ can be used with fixed $\kappa(\lambda_{MC})$ to match the LP_{01} transmission spectrum for some N_1 and N_2.

The practical utility of estimating $\kappa(\lambda)$ in this way is the engineering consideration that it is only possible to write marks and not delete them effectively. Thus the following experimental algorithm is useful to determine all the parameters of mode conversion by writing number of marks less than $N_1 + N_2$, provided that the irradiation and alignment conditions are precisely maintained throughout the experiment:

- Using TMI, determine $\Delta\phi(\lambda, I, F)$ for a particular mark writing condition. Also determine $\delta\beta(\lambda)$ *with unknown offset* using phase unwrapping of TMI or *with offset* by some other method like long acousto-optic gratings of small index perturbations [54].
- Write a single segment till the peak just gets overcoupled. This gives estimates of the quantities λ_{MC}, $\delta\beta_{MC}(\lambda_{MC})$, $\kappa(\lambda_{MC})$ and the maximum achievable mode conversion ratio. Using equation 6.4, $\delta\beta(\lambda)$ and $\delta\beta_{MC}(\lambda)$ are determined completely.
- By introducing an extra a gap of length $\frac{\pi}{\delta\beta_{MC}(\lambda_{MC})}$ in the direction of mark writing after the first segment, another segment is written till the appearance of distinct sidebands with minima at $\lambda_{\pm 1}$, where $\lambda_{-1} < \lambda_{MC} < \lambda_{+1}$. Note that $\lambda_{\pm 1}$ shifts with the mark writing. Fitting the spectra of two evolving dips using equation 7.4 and a polynomial model of $\kappa(\lambda)$ with fixed $\kappa(\lambda_{MC})$ obtained in the previous step, provides estimate of $\kappa(\lambda)$ for the interval $(\kappa(\lambda_{-1}),\kappa(\lambda_{+1}))$
- Use the estimates of $\delta\beta(\lambda)$, $\delta\beta_{MC}(\lambda)$ and $\kappa(\lambda)$ to compute N_1, N_2 and N_3 required for broadband mode conversion with the desired extinction ratio (for example 99 %).
- Given these estimates, and the presence of the already written segments, write appropriate number of extra marks required.

This algorithm was experimentally explored for LP_{01} and LP_{02} in the FMF.

7.3.2 Experimental verification for phase-shifted grating with three segments

The fabrication of the phase-shifted MCs was done using the LSV3 ArF Excimer laser setup from Optec together with the aerotech translation stage, as described in section 6.2.2. The irradiation condition described in section 6.3.4 was used for writing the marks.

Using the described method in the bullet points of section 7.3.1, bandwidth of 20 nm at 20 dB conversion ratio could be achieved repeatably in two resonance peaks of the

MC on both sides of the central wavelength of 1.56 μm. However, up to 8 % power was left in a residual bump around 1.56 μm. A spectrum at the broadest conversion at 1.525 μm is shown in figure 7.15, which is from 337 marks written in a phase-shifted MC with pitch Λ_{MC}=116 μm. The phase gap was 58.6 μm after the 49^{th} and the 118^{th} mark.

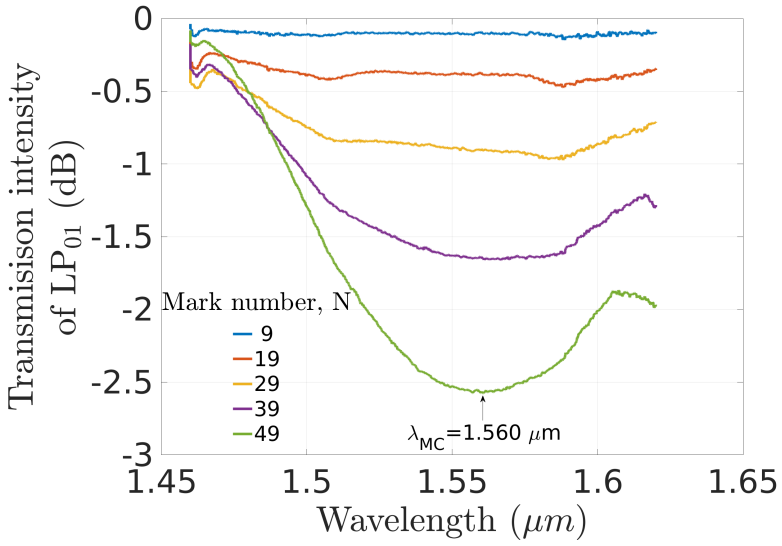

Figure 7.12 – Evolution of LP_{01} transmission intensity spectrum during writing of periodic marks at the first segment

The number of periods N_1 is experimentally determined such that the extinction ratio is around 50 % deep (figure 7.12). This provided an estimate $\lambda_{MC} = 1.56$ μm for the resonance wavelength.

After introducing a gap of 58.6 μm, writing further periodic marks decreased the extinction ratio at the beginning, followed by the appearance of two conversion peaks on both sides of $\lambda_{MC} = 1.56$ μm. Writing further marks deepened the two peaks, at the same time moving them closer.

To estimate $\kappa(1.56\ \mu\text{m})$, the extinction ratio at $\lambda_{MC} = 1.56$ μm was plotted as a function of number of written marks N (Figure 7.13). Fitting $cos^2(\kappa(\lambda_{MC})N\Lambda_{MC})$ gives estimate $\kappa(1.56\ \mu\text{m}) = 132\ \text{m}^{-1}$.

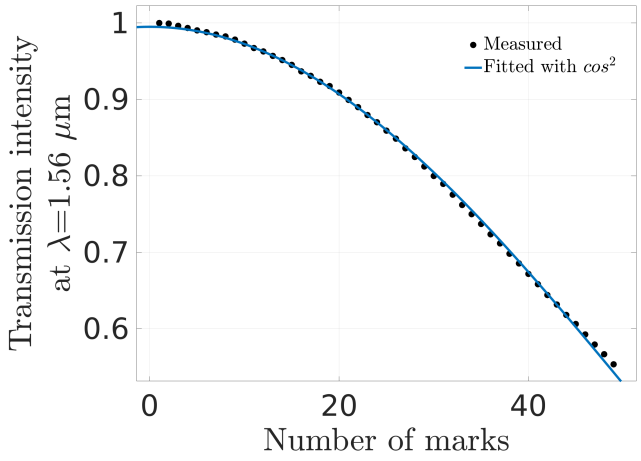

Figure 7.13 – Evolution of LP_{01} transmission intensity at 1.56 μm during writing of periodic marks at the first segment

The number of periods N_2 was determined such that the dip for $\lambda < \lambda_{MC} = 1.56$ μm has maximum 25 dB extinction-ratio. The extinction ratio of 25 dB was selected since the same writing conditions repeatedly produced stronger than 28 dB gratings at $\lambda_{MC} = 1.56$ μm (Figure 6.19) for single segments. Writing of the second segment was stopped once the extinction ratio of 25 dB was achieved, since writing further marks brings the two dips closer and causes loss of bandwidth at the end of three segments. However, the central wavelength where extinction ratio was minimum, shifted approximately 12 nm to 1.548 μm. In figure 7.14, the pitch in the simulation had to be shifted to $\Lambda_{MC} = 116.3$ μm to accommodate this. Taking a linear functionality of $\kappa(\lambda)$, with $\kappa(1.46\ \mu\text{m}) = \frac{\pi}{85}\ \mu\text{m}^{-1}$ and $\kappa(1.62\ \mu\text{m}) = \frac{\pi}{120}\ \mu\text{m}^{-1}$ fitted both the measured MC spectrum at the end of the second segment, as well as $\kappa(1.56\ \mu\text{m}) = \frac{\pi}{104}\ \mu\text{m}^{-1}$.

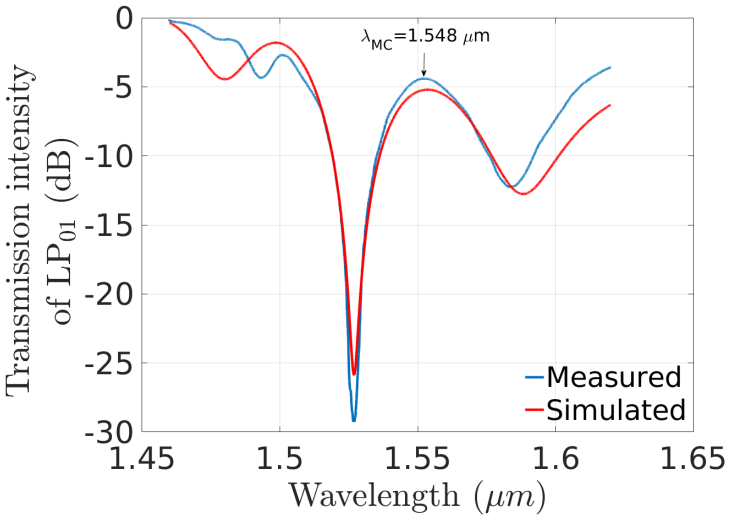

Figure 7.14 – Measured normalized LP_{01} transmission intensity spectrum after writing 118 marks, with a gap of 58.6 μm after 49 marks (first segment)

Writing further periodic marks in the third segment decreased the extinction ratio of the two peaks again at the beginning. Continuing further, mark writing started producing multiple conversion peaks which increased in conversion strength. At some point some of the peaks started decreasing in conversion strength. Writing was continued till conversion strength of the overall spectrum went beyond 20 dB. At 337 marks, the broadest conversion was observed, which is shown as a blue line in figure 7.15. The expected bandwidth of >35 nm was however not achieved, due to the presence of a residual bump in the middle of the spectrum.

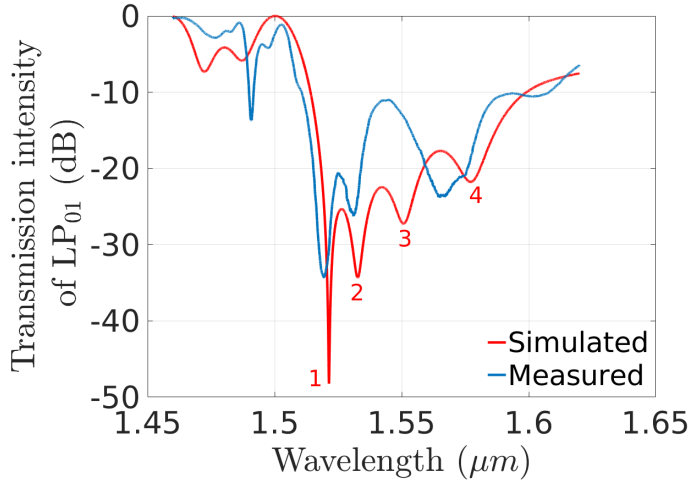

Figure 7.15 – Measured normalized LP_{01} transmission spectrum after writing 337 marks, with gaps of 58.6 μm introduced after 49 and 118 marks in the previous segments

In order to understand how misalignment might cause such a loss of extinction ratio,

a simulation was made with the same number of segments and phase shift as in the experiment. Using simulation parameters of $\Lambda_{MC} = 116.3$ μm, linear functionality of $\kappa(\lambda)$, $\delta\beta_{MC}(\lambda)$ and a multiplicative factor of 1.01 for $\kappa(\lambda)$ in the third segment produces four conversion peaks which match two peaks at the shorter wavelength (peaks 1 and 2 in figure 7.15). However, the two peaks at longer wavelengths (peaks 3 and 4 in figure 7.15) collapsed prematurely before peaks 1 and 2 deepened. This caused insufficient extinction ratio at peaks 3 and 4. The problem was identified to be the nonlinear path traversed by the translation stage when it is asked for a linear displacement along the fiber axis. The misalignment was fully characterized by correcting the misalignment at every 5 mm displacement using the translation stage controller. The value of the correction was noted down, which is plotted in figure 7.16.

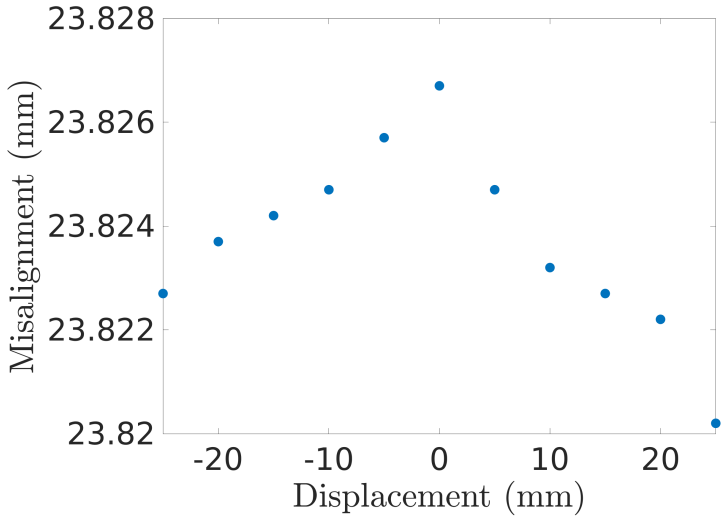

Figure 7.16 – Misalignment of translation stage during displacement

If the alignment was maintained, such that the peaks 3 and 4 in figure 7.15 would not collapse prematurely, then simulation shows that the spectrum with broadest bandwidth at 20 dB extinction ratio would be at $N1 = 49$, $N2 = 116$, $N3 = 178$. The corresponding spectrum should ideally have looked like the simulation shown in figure 7.17, with a theoretically achievable bandwidth of 62.5 nm at 20 dB extinction ratio.

The misalignment was compensated by making the translation stage follow two linear curves, and thereby the bandwidth could be improved upto an extinction ratio of 15.5 dB. Figure 7.18 shows a LP_{01} transmission spectrum for three segments of pitch $\Lambda_{MC} = 116$ μm shifted by half the intermodal beat length at 1.56 μm. The number of marks are $N1 = 42, N2 = 127, N3 = 192$, which showed stronger than 15.5 dB (extinction ratio >97 %) conversion between 1542 nm to 1579 nm. The simulation which best matched the measured spectrum in shape had a modified pitch of $\Lambda_{MC} = 115.6$ μm. In addition to the different pitch used for the simulation, the measurement also does not exactly match with the simulation for the third segment. These indicate presence of residual misalignment and instability of irradiation condition (for example due to residues

of coating), which can be improved with better alignment and chemical cleaning of the stripped part of the fiber (e.g. with dichloromethane).

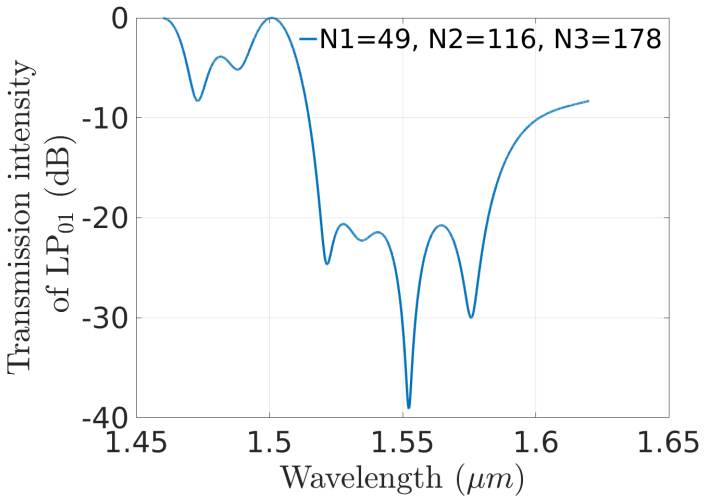

Figure 7.17 – Simulated spectrum of broadband MC, in absence of translation stage misalignment

The high sensitivity of the phase shifted MC irradiation can be understood by the relatively large effect on the parameters $\kappa(\lambda)$ and the effective $\delta\beta(\lambda)$ of the full MC, which themselves have small values. The multiple resonance peaks in the phase shifted MC can be approximately described by multiple phase matching of the effective intermodal dispersion curve. Since the effective curve is quite flat, the peak wavelengths shift strongly due to small changes in the irradiation. In addition, any defect in the irradiation can have strong effect on the phase shifted MC spectrum, for example due to presence of unremoved coating during irradiation.

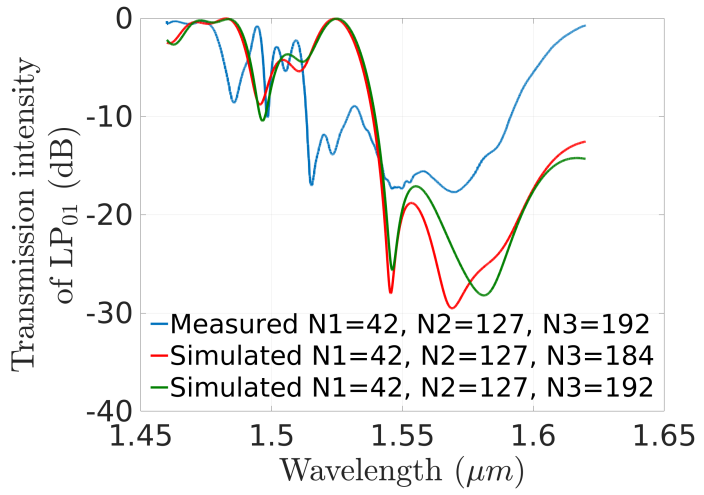

Figure 7.18 – Measured spectrum of broadband MC, fabricated with compensation of translation stage misalignment

7.4 Broadband mode conversion with only two segments

Extensive simulations with different mode pairs further hinted that even without estimation of $\Delta\phi(\lambda)$ added by written marks, there exists a direct experimental algorithm to fabricate high-extinction broadband mode converters. The algorithm consists of the following steps-

1. A segment is written such that it reaches extinction ratio just below 50 %, as guessed from the growth rate of the resonance dip.

2. A gap is introduced corresponding to a phase shift of π at λ_{MC}.

3. Writing of marks with same pitch as the first segment is continued, which will give rise to two conversion dips on both sides of λ_{MC}, after initially reverting in conversion strength. After writing sufficient number of marks in the second segment, the two conversion dips will start to increase in conversion strength while their individual minima wavelengths will start to move closer to each other. Writing should be continued till optimum combination of bandwidth and extinction ratio is reached. The stopping condition can be defined as the number of marks in the second segment after which the spectral bandwidth or extinction ratio at one or both dips start to decrease.

The only pre-existing knowledge needed for this method should be of the intermodal dispersion of the pristine fiber $\delta\beta(\lambda)$, such that a phase gap of π can be introduced between the two segments at the resonance wavelength.

This is the only existing method in literature, that exhibits broadband high-extinction mode conversion in few-mode fibers using only two segments. The generality of this method suggests an underlying mathematical proof for a flexible range of intermodal dispersion and coupling constant. Such a proof was beyond the timeline of this thesis.

7.4.1 Experimental verification for phase-shifted grating with two segments

With careful control of duty cycle and laser power, $k(\lambda)$ was increased in the exposure setup. Thereafter, this algorithm was verified experimentally.

Instead of directly following the presented algorithm, at first an overcoupled segment was written in order to quantify the maximum conversion strength achievable at the resonance wavelength. As shown in figure 7.19, the conversion spectra increased in strength up to 20 dB for 76 marks, after which it started to revert in strength through overcoupling. The mark writing was stopped at 77 marks at this point.

After introducing an extra gap of 65 μm along the fiber axis in the direction of mark-writing of the first segment, 38 more marks were written in the same direction. Afterwards, writing of marks was continued for the first segment in the other direction. At first a decrease in conversion strength was observed. This was followed by the appearance, growth, and strength reversal with 130 additional marks for $\lambda > \lambda_{MC}$. After writing 125 marks, another dip could be seen appearing for $\lambda < \lambda_{MC}$, and kept increasing in strength with further writing. From 140 marks onwards, as shown in figure 7.20, both the dips kept increasing in strength up to 153 marks. The wavelengths of maximum conversion kept moving towards each other between 140 and 153 marks. When the 154th mark was written, the conversion dip for $\lambda < \lambda_{MC}$ started reverting. Mark writing was stopped at this point.

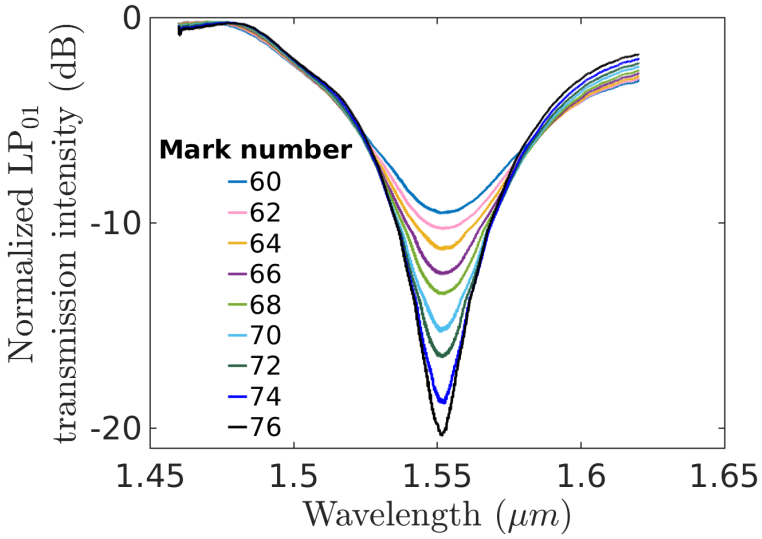

Figure 7.19 – Measured evolution of the normalized LP_{01} transmission spectra with writing of marks without any phase shift, for segment 2 which contains standard periodic marks. The maximum achievable extinction ratio was 20 dB at 76 marks, after which the depth of the spectrum started to revert with writing of more marks due to overcoupling of the grating.

From the measured data, the direct experimental algorithm to fabricate broadband high-extinction MC using only two segments with a phase shift was conditionally verified, by achieving 41 nm bandwidth at 16 dB conversion strength. The conditionality comes from the fact that with one segment only 20 dB maximum conversion strength could be achieved at 76 marks. If a stronger maximum conversion strength can be achieved, the conversion strength of the two dips for the two combined segments will scale proportionally. Therefore it is predicted that using similar value of $\kappa(\lambda_{MC})$ for the FMF, and for a 25 dB maximum conversion strength with a single segment, 41 nm bandwidth at 20 dB conversion strength can be achieved using two segments.

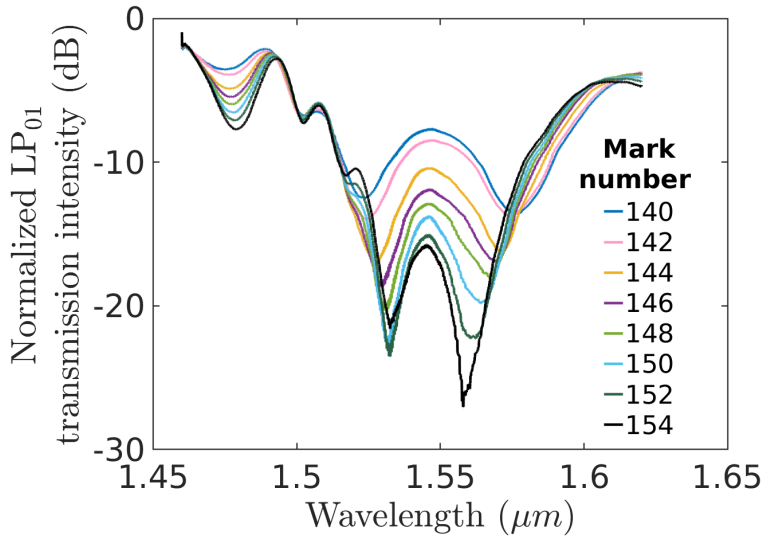

Figure 7.20 – Measured evolution of the normalized LP_{01} transmission spectra after adding segment 1, containing 37 extra marks separated with a phase shift of π at 1.55 μm, *before* segment 2. Further marks were written on the other side of segment 2 without any extra phase gap, and the spectra were recorded

7.5 Conclusions

Two new possible methods of fabricating broadband phase segments were evaluated using simulations and experiments. The method of partial core irradiation was simulated using uniform segment model, where a semicircular region of the core in the irradiated segment had a different refractive index. Strong index change showed large increase in normalized overlap integrals for orthogonal mode pairs of the pristine fiber. For some mode pairs the intermodal dispersion curve also became flat. However high loss is introduced for strong irradiation conditions, due to poor overlap of the mode fields. More precise simulations using continuous index change patterns along z over the irradiated segment could not be implemented and deserves attention.

The method of phase shifted gratings can potentially provide low loss MCs of bandwidth larger than 35 nm at 20 dB extinction ratio. Phase shifted gratings made with 3 segments of pitch 116 μm and gap of length 58.6 μm were fabricated. Without compensation of misalignment (maximum 6 μm) of the translation stage, two peaks of 20 nm bandwidth at 20 dB extinction ratio could be achieved, with a 11 dB bump left between these peaks. On introducing compensation of the misalignment of the translation stage, 37 nm bandwidth was achieved at 15.5 dB extinction ratio. The location and strength of the multiple overlapping conversion peaks of phase-shifted MC with three segments are highly sensitive to changes in alignment and irradiation conditions. There is room for experimentally achieving larger than 35 nm at 20 dB extinction ratio, by stabilizing these

parameters over different marks.

For sufficiently large value of $\kappa(\lambda)$ an experimental algorithm to fabricate broadband high-extinction MC is presented which does not even require estimation of $\Delta\phi(\lambda)$. The method was experimentally verified to achieve a bandwidth of 41 nm at 16 dB conversion strength.

8 Summary and conclusions

Effects associated with two-mode interference were found to be useful for multiple sensing modalities and parameter estimates. It was determined that the temperature sensitivity $\frac{\partial\delta\beta(\lambda)}{\partial T}$ and the strain sensitivity of $\frac{\partial\delta\beta(\lambda)}{\partial\epsilon}$ were highly variable in the wavelength range of 1.46 μm-1.62 μm, both varying by factors more than 2.5 over this range in their relative values. TMI shifts were used for parameter estimation in two different types of irradiation conditions, namely (a) estimation of $\frac{\partial\delta\beta(\lambda)}{\partial F}$, where F is fluence, during scanning exposure of the fiber with a laser spot moving with constant velocity, and (b) estimation of extra phase introduced between two interacting modes in an irradiated region. Method (a) is based on a cumulative effect, and thus allows for measurement of very small changes in $\delta\beta(\lambda)$, by scanning over longer lengths of the FMF. By scanning over a 51 mm long FMF, 0.6 % relative change in $\delta\beta(\lambda)$ could be determined. Method (b) is the only direct experimental tool to predict the intermodal dispersion experienced by two modes when they are resonantly interacting inside an MC. It also provides precise estimate for the offset of the intermodal dispersion curve of the FMF (<0.1 % error).

GVE wavelength associated to TMI had 3 times larger linear thermal response compared to an FBG resonance at similar wavelengths. The strain response was of similar magnitude to an FBG but of opposite sign. Together these present the capability of temperature and strain differentiation. Relative errors of 1.4 % and 1.1 % are obtained for sensing temperature and strain individually. Under uniform scanning irradiation of the whole fiber, GVE wavelength could also provide high-precision estimates for the change in the core refractive index. The sensitivity of this method is more than 40 times larger compared to sensing of core index change during irradiation using an FBG. Also the GVE shift captures very small index changes right from the beginning of an irradiation albeit for longer exposure times, whereas an FBG needs to acquire sufficient index perturbation before the reflection peaks become discernible. The sensitivity of the GVE wavelength to temperature, strain and laser exposure are only dependent on the material parameters and not on the modes involved, as long as the fiber profile does not change significantly during the change of these parameters.

Multiple reflection peaks from two modes in a FMF containing an FBG were used for approximate prediction of the offset of intermodal dispersion. The estimates turned out to be correct within 0.8 %. The estimated intermodal dispersion curves and phase change due to each mark were verified by matching the predicted resonance wavelength of multiple mode converters with different pitch but same irradiation conditions.

Estimates of $\delta\beta(\lambda)$ and $\delta\beta_{MC}(\lambda)$ provides knowledge about the phase relation of the corresponding modes travelling through the pristine fiber and the MC segment. Using this the resonance wavelength could be maintained within precision of ±1 nm. Making an MC with a single phase-shift allowed for estimation of the MC coupling constant as a function of wavelength over 40 nm. Using these estimates, fabrication of MCs with two phase shifts gave 20 nm bandwidth at 20 dB conversion ratio for a MC made without compensating for translation stage misalignment. After compensating for translation stage misalignment, 37 nm bandwidth was achieved at 15.5 dB extinction ratio.

Another experimental was developed for direct fabrication of broadband high-extinction MCs using only two segments with a phase shift and the estimate of $\delta\beta_{MC}(\lambda)$, which does not even require the knowledge of $\delta\beta_{MC}(\lambda)$. Using this method 41 nm bandwidth was achieved at 16 dB conversion ratio at 1.56 μm wavelength.

In conclusion, multiple methods were developed based on two-mode interference and associated GVE wavelength. A new relation between TMI and mode conversion was found, which can be used to separate the intermodal dispersion terms in the mathematical description of an MC. This allowed for independent determination of MC coupling as a function of wavelength. Putting all the estimates together provides a recipe for fabricating broadband MCs at high extinction ratio. However, the recipe is highly sensitive to any errors in misalignment or irradiation conditions, and need strict engineering precision to be achieved experimentally. The direct experimental algorithm using only two segments is even more general and robust. If the coupling constant is large, the method with two segments might suffice for a variety of scenarios needing broadband high-extinction mode conversion.

The general method to estimate intermodal dispersion experienced by an MC will reduce the experimental burden of iteratively finding the pitch for a desired resonance wavelength. From the perspective of applications, broadband high-extinction mode converters can be used for dispersion management in laser cavities.

9 Acknowledgement

SNF project 200020_169415: Fiber gratings and mode converters in few-mode fibers for telecom and sensing applications, SNF project 200020_144000: Fiber gratings in few-mode and multi-core fibers for telecom and sensor applications, and SNF project 206021_144962: UV Femtosecond laser system for nano-crystallization, waveguide fabrication, and structuring, are acknowledged for supporting this doctoral research. The detailed corrections from the jury memebers have been of utmost help in finalizing the thesis document.

Due to the candidate being the only employee of the laboratory, the project could not have been completed without the generous help of many members on the EPFL community. Special thanks to Krishnamoorthy Pullyvan for help with automatizing the various machinery and for IT, Ronald Gianotti for the omnipresent help with electronics and machine interfacing. Prof. Rishikesh Kulkakrni and Prof. Fabio Donati were constant inspirations in the journey to find the connection between mode conversion and two-mode interference. Dr. Svyatoslav Kharitanov has been the perennial sounding board for every scientific idea during the PhD, and Dr. Toralf Scharf arranged generous access to direly needed equipment. The experiments in the CMI facility of EPFL were only possible thanks to Joffrey Pernollet, who graciously arranged heavily discounted access to the OPTEC LSV3 setup at the critical final hour, and even organized adjoining custom machinery to the setup. The stress of handling the one-man show was ameliorated by the social embrace from the members of the LBP and MICROBS groups in EPFL, especially Dr. Marie Didier, Dr. Igor Nahálka, Nathan Dupertuis, Marie Bischoff (LBP), Erik Mailand and Raquel Pereira (MICROBS).

As with everything else, the backbone of journey has been my wife Dr. Aparajita Singha, spanning the organization of ideas, experimental design and implementation, and assisting in thesis corrections, to mention a few.

10 Glossary of terms

10.1 List of symbols and operators

λ	Free-space wavelength
T	Temperature
ϵ	Strain
ω	Angular frequency
ϵ_0	Permittivity of free space
$k_0(\lambda)$	Vacuum wavevector
$n(x,y)$	Refractive index profile in x,y
$k(x,y)$	Wavevector in x,y
$\mathbb{N}$	Natural numbers
$\mathbb{Z}$	Integers
$\mathbb{R}$	Real numbers
$\mathbb{C}$	Complex numbers
$\mathbb{R}^k$, for some $k \in \mathbb{N}$	The ordered tuple $(a_1,...,a_k)$, with $a_1,...,a_k \in \mathbb{R}$
$W^{1,2}(\mathbb{R}^2)$	Space of square-integrable functions with *weak derivative* in the sense of distributions
$\beta_n(\lambda) > 0$	Propagation constant of the n^{th} mode
$a+ib$	Root of $x^2 - 2ax + (a^2+b^2) = 0$ for $a,b \in \mathbb{R}$
$\overline{a+ib} = a-ib$	Complex conjugate operator, for $a,b \in \mathbb{R}$
$\lvert a+ib\rvert = \sqrt{a^2+b^2}$	modulus operator, for $a,b \in \mathbb{R}$
$e^{ix} = cos(x) + i\ sin(x)$	Euler's formula
$\hat{x}$	Unit vector in x direction
$\vec{A}$	$\vec{A}(x,y,z) = A_x(x,y,z)\hat{x} + A_y(x,y,z)\hat{y} + A_z(x,y,z)\hat{z}$ $A_x(x,y,z), A_y(x,y,z), A_z(x,y,z) \in \mathbb{C}$

$\vec{A}.\vec{B} = A_x B_x + A_y B_y + A_z B_z$	Dot product
$\nabla.\vec{A} = \frac{\partial A_x}{\partial x} + \frac{\partial A_y}{\partial y} + \frac{\partial A_z}{\partial z}$	Divergence operator, which acts on a vector to produce a real number
$\nabla \times \vec{A} = \left(\frac{\partial A_z}{\partial y} - \frac{\partial A_y}{\partial z}\right) + \left(\frac{\partial A_x}{\partial z} - \frac{\partial A_z}{\partial x}\right) + \left(\frac{\partial A_y}{\partial x} - \frac{\partial A_x}{\partial y}\right)$	Curl operator, which acts on a vector to produce another vector. Divergence and curl satisfy $\nabla.(\nabla \times \vec{A}) = 0$, for all $\vec{A} \in \mathbb{R}^n,\ n \in \mathbb{N}$
$\Delta = \frac{\partial^2}{\partial x^2} + \frac{\partial^2}{\partial y^2} + \frac{\partial^2}{\partial z^2}$	Laplace operator

10.2 List of abbreviations

FMF	Few-mode fiber
SMF	Single-mode fiber
LP	Linear polarization
TMI	Two-mode interference
GVE	Group-velocity equalization
FBG	Fiber Bragg grating
LPG	Long-period grating
MC	Mode converter grating
EDFA	Erbium-doped fiber amplifier
TDM	Time-division multiplexing
WDM	Wavelength-division multiplexing
PDM	Polarization-division multiplexing
MDM	Mode-division multiplexing
TE	Transverse electric
TM	Transverse magnetic
CMI	Center of MicroNanoTechnology
ArF	Argon Fluoride molecule
UV	Ultra-violet
OSA	Optical spectrum analyzer
2H	Second harmonic
4H	Fourth harmonic
N.A.	Not available
a.u.	Arbitrary units
Pitch	Period length of a peridic perturbation along the fiber axis

A Appendix

A.1 Material constants

The linear slopes of relative change in relevant parameters with temperature, which are used in chapter 5, are consolidated in table A.1. Thermo-optic coefficient refers to relative change of refractive index with temperature at 1.64 μm wavelength. Thermal expansion coefficient refers to relative change of fiber length with temperature.

	Thermal expansion coefficient	Thermo-optic coefficient
	($°C^{-1}$)	($°C^{-1}$)
Fused silica	0.6×10^{-6} [106]	5.86×10^{-6} [108]
14 % GeO_2-doped silica	1.7×10^{-6} [60]	6.24×10^{-6} [108]

Table A.1 – Material constants for fused silica and 14 % GeO_2-doped silica

Table D.2 qnd figure D.3 in the PhD thesis [108] reports the sum of the thermo-optic and thermal expansion coefficients (Equation A.1), from which the thermo-optic coefficient was extracted. The extracted thermo-optic coefficient from [108] for fused silica matches the systematic study [107] at 300 K temperature.

Equation A.1 presents the linear fitting result of the data in table D.2 of the PhD thesis [108], up to 22 % GeO_2 concentration.

$$\frac{1}{L}\frac{\partial L}{\partial T} + \frac{1}{n_e}\frac{\partial n_e}{\partial T} = (2.698 \times 10^{-6}) \times d_{Ge} + 6.462 \times 10^{-6} \tag{A.1}$$

Bibliography

[1] Hill, K. O., Malo, B., Bilodeau, F., Johnson, D. C. & Albert, J. Bragg gratings fabricated in monomode photosensitive optical fiber by UV exposure through a phase mask. *Applied Physics Letters* **62**, 1035 (1993).

[2] Hill, K. O. *et al.* Efficient mode conversion in telecommunication fibre using externally written gratings. *Electronics Letters* **26**, 1270 – 1272 (1990).

[3] Yoshino, T., Kurosawa, K., Itoh, K. & Ose, T. Fiber-optic Fabry-Perot interferometer and its sensor applications. *IEEE Journal of Quantum Electronics* **18**, 1612 – 1621 (1982).

[4] Dixon, R. W. Photoelastic Properties of Selected Materials and Their Relevance for Applications to Acoustic Light Modulators and Scanners. *Journal of Applied Physics* **38**, 5149 (1967).

[5] Primak, W. & Post, D. Photoelastic Constants of Vitreous Silica and Its Elastic Coefficient of Refractive Index. *Journal of Applied Physics* **30**, 779 (1959).

[6] Vasil'ev, S. A., Dianov, E. M., Kurkov, A. S., Medvedkov, O. I. & Protopopov, V. N. Photoinduced in-fibre refractive-index gratings for core — cladding mode coupling. *Quantum Electronics* **27** (1997).

[7] Malitson, I. H. Interspecimen Comparison of the Refractive Index of Fused Silica. *Journal of the Optical Society of America* **55**, 1205–1209 (1965).

[8] Fleming, J. W. Dispersion in GeO_2–SiO_2 glasses. *Applied Optics* **23**, 4486–4493 (1984).

[9] The Nobel Prize in Physics 2009, NobelPrize.org, accessed on 19 march 2019.

[10] Kao, K. C. & Hockham, G. A. Dielectric-fibre surface waveguides for optical frequencies. *IEE Proceedings J - Optoelectronics* **133**, 1151 – 1158 (1986).

[11] Knight, J. C., Birks, T. A., Russell, P. S. J. & Atkin, D. M. All-silica single-mode optical fiber with photonic crystal cladding. *Optics Letters* **21**, 1547–1549 (1996).

[12] Durnin, J., Miceli, J. J. & Eberly, J. H. Diffraction-free beams. *Physical Review Letters* **58**, 1499 (1987).

[13] Durnin, J. Exact solutions for nondiffracting beams. I. The scalar theory. *Journal of the Optical Society of America A* **4**, 651–654 (1987).

[14] Kahn, J. & Ho, K.-P. Spectral efficiency limits and modulation/detection techniques for DWDM systems. *IEEE Journal of Selected Topics in Quantum Electronics* **10** (2004).

[15] Richardson, D. J. Filling the Light Pipe. *Science* **330**, 327–328 (2010).

[16] Tkach, R. W. Scaling optical communications for the next decade and beyond. *Bell Labs Technical Journal* **14**, 3–9 (2010).

[17] Berdagué, S. & Facq, P. Mode division multiplexing in optical fibers. *Applied Optics* **21**, 1950–1955 (1982).

[18] Sillard, P., Bigot-Astruc, M., Boivin, D., Maerten, H. & Provost, L. Few-Mode Fiber for Uncoupled Mode-Division Multiplexing Transmissions. In *37th European Conference and Exposition on Optical Communications (2011), paper Tu.5.LeCervin.7* (Optical Society of America, 2011).

[19] Hanzawa, N. *et al.* Demonstration of mode-division multiplexing transmission over 10 km two-mode fiber with mode coupler. In *2011 Optical Fiber Communication Conference and Exposition/ National Fiber Optic Engineers Conference 2011, OSA technical digest (CD), paper OWA4* (Optical Society of America, 2011).

[20] Randel, S. *et al.* 6×56-Gb/s mode-division multiplexed transmission over 33-km few-mode fiber enabled by 6×6 MIMO equalization. *Optics Express* **19**, 16697–16707 (2011).

[21] Richardson, D. J., Fini, J. M. & Nelson, L. E. Space-division multiplexing in optical fibres. *Nature Photonics* **7**, 354–362 (2013).

[22] Chang, S. H. *et al.* Mode division multiplexed optical transmission enabled by all–fiber mode multiplexer. *Optics Express* **22**, 14229–14236 (2014).

[23] Winzer, P. J. Making spatial multiplexing a reality. *Nature Photonics* **8**, 345–348 (2014).

[24] Stuart, H. R. Dispersive Multiplexing in Multimode Optical Fiber. *Science* **289**, 281–283 (2000).

[25] Winzer, P. J. & Foschini, G. J. MIMO capacities and outage probabilities in spatially multiplexed optical transport systems. *Optics Express* **19**, 16680–16696 (2011).

[26] Mears, R., Reekie, L., Jauncey, I. & Payne, D. Low-noise erbium-doped fibre amplifier operating at 1.54 m. *Electronics Letters* **23**, 1026–1028 (1987).

[27] Nakazawa, M., Kimura, Y. & Suzuki, K. Efficient $Er^{3+}-$ doped optical fiber amplifier pumped by a 1.48 μm InGaAsP laser diode. *Applied Physics Letters* **54**, 295 (1989).

[28] Poole, C., Wiesenfeld, J., DiGiovanni, D. & Vengsarkar, A. Optical fiber-based dispersion compensation using higher order modes near cutoff. *Journal of Lightwave Technology* **12**, 1746 – 1758 (1994).

[29] Ky, N. H., Limberger, H. G., Salathé, R. P. & Cochet, F. Efficient broadband in-tracore grating LP_{01}–LP_{02} mode converters for chromatic-dispersion compensation. *Optics Letters* **23**, 445–447 (1998).

[30] Bhatia, V. & Vengsarkar, A. M. Optical fiber long-period grating sensors. *Optics Letters* **21**, 692–694 (1996).

[31] Ramachandran, S., Wang, Z. & Yan, M. Bandwidth control of long-period grating-based mode converters in few-mode fibers. *Optics Letters* **27**, 698–700 (2002).

[32] Östling, D. & Engan, H. E. Broadband spatial mode conversion by chirped fiber bending. *Optics Letters* **21** (1996).

[33] MacDougall, T. W., Pilevar, S., Haggans, C. W. & Jackson, M. A. Generalized expression for the growth of long period gratings. *IEEE Photonics Technology Letters* **10**, 1449 – 1451 (1998).

[34] Partridge, M., James, S. W., Barrington, J. & Tatam, R. P. Overwrite fabrication and tuning of long period gratings. *Optics Express* **24**, 22345–22356 (2016).

[35] Chan, F. Y. M. & Chiang, K. S. Analysis of apodized phase-shifted long-period fiber gratings. *Optics Communications* **244**, 233–243 (2005).

[36] Savolainen, J. M., Kristensen, P., Grüner-Nielsen, L. & Balling, P. Broadband Mode Converters by Femtosecond-Laser-Light Refractive-Index Tailoring. *IEEE Photonics Technology Letters* **26**, 1454 – 1457 (2014).

[37] Dong, J. & Chiang, K. S. Temperature-Insensitive Mode Converters With CO2-Laser Written Long-Period Fiber Gratings. *IEEE Photonics Technology Letters* **27**, 1006 – 1009 (2015).

[38] Zheng, Y., Li, Y., Li, W. & Wu, J. All Fiber Broadband Mode Converter Based on Semicircular-Distribution Long Period Fiber Gratings. In *Conference on Lasers and Electro-Optics (2016), paper JTu5A.108* (Optical Society of America, 2016).

[39] Zhao, Y., Liu, Y., Zhang, C., Wen, J. & Wang, T. Mode Conversion of Four-Mode Fiber with CO2-Laser Written Long-Period Fiber Gratings. In *Frontiers in Optics 2016 (2016), paper JW4A.34* (Optical Society of America, 2016).

[40] Israelsen, S. M. & Rottwitt, K. Broadband higher order mode conversion using chirped microbend long period gratings. *Optics Express* **24**, 23969–23976 (2016).

[41] Xue, Y.-r. *et al.* All-fiber mode converter based on superimposed long period fiber gratings. *Optoelectronic Letters* **14**, 81–83 (2018).

[42] Zienkiewicz, O. C. *The finite element method in engineering science* (McGraw-Hill, New York, 1971).

[43] Koshiba, M. *Optical Waveguide Theory by the Finite Element Method*. Advances in Opto-Electronics (Springer Netherlands, 1992).

[44] Okamoto, K. Chapter 3 - Optical fibers. In *Fundamentals of Optical Waveguides (Second Edition)*, 57–158 (Academic Press, Burlington, 2006).

[45] Gloge, D. Weakly Guiding Fibers. *Applied Optics* **10**, 2252–2258 (1971).

[46] Feced, R., Zervas, M. N. & Muriel, M. A. An efficient inverse scattering algorithm for the design of nonuniform fiber Bragg gratings. *IEEE Journal of Quantum Electronics* **35**, 1105 – 1115 (1999).

[47] Kartchevski, E., Nosich, A. & Hanson, G. Mathematical Analysis of the Generalized Natural Modes of an Inhomogeneous Optical Fiber. *SIAM Journal on Applied Mathematics* **65**, 2033–2048 (2005).

[48] Bamberger, A. & Bonnet, A. Mathematical Analysis of the Guided Modes of an Optical Fiber. *SIAM Journal of Mathematical Analysis* **21**, 1487–1510 (1990).

[49] Stratton, J. A. *Electromagnetic Theory* (McGraw-Hill, New York, 1941).

[50] Snitzer, E. Cylindrical Dielectric Waveguide Modes. *Journal of the Optical Society of America* **51**, 491–498 (1961).

[51] Kawakami, S. & Nishida, S. Characteristics of a doubly clad optical fiber with a low-index inner cladding. *IEEE Journal of Quantum Electronics* **10**, 879 – 887 (1974).

[52] Brezis, H. *Functional Analysis, Sobolev Spaces and Partial Differential Equations* (Springer, New York, 2010).

[53] Okamoto, K. Chapter 6 - Finite element method. In *Fundamentals of Optical Waveguides (Second Edition)*, 261–328 (Academic Press, Burlington, 2006).

[54] Alcusa-Sáez, E., Díez, A. & Andrés, M. V. Accurate mode characterization of two-mode optical fibers by in-fiber acousto-optics. *Optics Express* **24**, 4899–4905 (2016).

[55] Wang, L. & Erdogan, T. Layer peeling algorithm for reconstruction of long-period fibre gratings. *Electronics Letters* **37**, 154 – 156 (2001).

[56] Erdogan, T. Fiber grating spectra. *Journal of Lightwave Technology* **15**, 1277 – 1294 (1997).

[57] Liu, Y., Williams, J. A. R., Zhang, L. & Bennion, I. Phase shifted and cascaded long-period fiber gratings. *Optics Communications* **164**, 27–31 (1999).

[58] Yablon, A. D. Multi-Wavelength Optical Fiber Refractive Index Profiling by Spatially Resolved Fourier Transform Spectroscopy. *Journal of Lightwave Technology* **28**, 360–364 (2010).

[59] Yablon, A. D. *et al.* Refractive index perturbations in optical fibers resulting from frozen-in viscoelasticity. *Applied Physics Letters* **84**, 19–21 (2004).

[60] Huang, Y. Y., Sarkar, A. & Schultz, P. C. Relationship between composition, density and refractive index for germania silica glasses. *Journal of Non-Crystalline Solids* **27**, 29–37 (1978).

[61] Zhao, Y. *et al.* All-fiber mode converter based on long-period fiber gratings written in few-mode fiber. *Optics Letters* **42**, 4708–4711 (2017).

[62] Wu, H. *et al.* All-fiber second-order optical vortex generation based on strong modulated long-period grating in a four-mode fiber. *Optics Letters* **42**, 5210–5213 (2017).

[63] Hill, K. O., Fujii, Y., Johnson, D. C. & Kawasaki, B. S. Photosensitivity in optical fiber waveguides: Application to reflection filter fabrication. *Applied Physics Letters* **32**, 647 (1978).

[64] Meltz, G., Morey, W. W. & Glenn, W. H. Formation of Bragg gratings in optical fibers by a transverse holographic method. *Optics Letters* **14**, 823–825 (1989).

[65] Kashyap, R. *Fiber Bragg Gratings (Second Edition)* (Academic Press, Boston, 2010).

[66] Yariv, A. Coupled-mode theory for guided-wave optics. *IEEE Journal of Quantum Electronics* **9**, 919 – 933 (1973).

[67] Colaço, C., Caldas, P., Villar, I. D., Chibante, R. & Rego, G. Arc-Induced Long-Period Fiber Gratings in the Dispersion Turning Points. *Journal of Lightwave Technology* **34**, 4584–4590 (2016).

[68] Wu, C. *et al.* Strong LP_{01} and LP_{11} Mutual Coupling Conversion in a Two-Mode Fiber Bragg Grating. *IEEE Photonics Journal* **4**, 1080 – 1086 (2012).

[69] Hindle, F. *et al.* Inscription of long-period gratings in pure silica and Germanosilicate fiber cores by femtosecond laser irradiation. *IEEE Photonics Technology Letters* **16**, 1861 – 1863 (2004).

[70] Wiesmann, D., David, C., Germann, R., Emi, D. & Bona, G. L. Apodized surface-corrugated gratings with varying duty cycles. *IEEE Photonics Technology Letters* **12**, 639 – 641 (2000).

[71] Marcuse, D. Curvature loss formula for optical fibers. *Journal of the Optical Society of America* **66**, 216–220 (1976).

[72] Koplow, J. P., Kliner, D. A. V. & Goldberg, L. Single-mode operation of a coiled multimode fiber amplifier. *Optics Letters* **25**, 442–444 (2000).

[73] Schulze, C. *et al.* Mode resolved bend loss in few-mode optical fibers. *Optics Express* **21**, 3170–3181 (2013).

[74] Bhatia, V. Applications of long-period gratings to single and multi-parameter sensing. *Optics Express* **4**, 457–466 (1999).

[75] Kumar, M., Kumar, A. & Tripathi, S. M. A comparison of temperature sensing characteristics of SMS structures using step and graded index multimode fibers. *Optics Communications* **312**, 222–226 (2014).

[76] Lu, C. *et al.* Studies on Temperature and Strain Sensitivities of a Few-Mode Critical Wavelength Fiber Optic Sensor. *IEEE Sensors Journal* **19**, 1794 – 1801 (2019).

[77] Archambault, J. *et al.* Fibre core profile characterization by measuring group velocity equalization wavelengths. *IEEE Photonics Technology Letters* **3**, 351 – 353 (1991).

[78] Menashe, D., Tur, M. & Danziger, Y. Interferometric technique for measuring dispersion of high order modes in optical fibres. *Electronics Letters* **37**, 1439 – 1440 (2001).

[79] Basu, S. & Limberger, H. G. Temperature and Strain Sensitivity of Two-Mode Interference and Waveguide Dispersion. In *43th European Conference on Optical Communication (ECOC 2017), paper Tu.1.A.3.* (2017).

[80] Fatemi, F. K. & Beadie, G. Spatially-resolved Rayleigh scattering for analysis of vector mode propagation in few-mode fibers. *Optics Express* **23**, 3831–3840 (2015).

[81] Song, D. R., Park, H. S., Kim, B. Y. & Song, K. Y. Acoustooptic Generation and Characterization of the Higher Order Modes in a Four-Mode Fiber for Mode-Division Multiplexed Transmission. *Journal of Lightwave Technology* **32**, 4534 – 4538 (2014).

[82] Savolainen, J.-M., Grüner-Nielsen, L., Kristensen, P. & Balling, P. Measurement of effective refractive-index differences in a few-mode fiber by axial fiber stretching. *Optics Express* **20**, 18646–18651 (2012).

[83] Marcuee, D. Loss analysis of single-mode fiber splices. *Bell System Technical Journal* **56**, 703–718 (1977).

[84] Tripathi, S. M., Kumar, A., Marin, E. & Meunier, J. P. Critical Wavelength in the Transmission Spectrum of SMS Fiber Structure Employing GeO_2-Doped Multimode Fiber. *IEEE Photonics Technology Letters* **22**, 799 – 801 (2010).

[85] Garcia, F. C., Fokine, M., Margulis, W. & Kashyap, R. Mach-Zehnder interferometer using single standard telecommunication optical fibre. *Electronics Letters* **37**, 1440 – 1442 (2001).

[86] Garcia, F. C., Kashyap, R., Fokine, M. & Margulis, W. Highly stable Mach-Zehnder Interferometer using a single standard telecommunication optical fiber. In *Conference on Lasers and Electro-Optics, paper CThI7* (Optical Society of America, 2000).

[87] Nicholson, J. W., Yablon, A. D., Ramachandran, S. & Ghalmi, S. Spatially and spectrally resolved imaging of modal content in large-mode-area fibers. *Optics Express* **16**, 7233–7243 (2008).

[88] Ali, M. M. *et al.* Characterization of Mode Coupling in Few-Mode FBG With Selective Mode Excitation. *IEEE Photonics Technology Letters* **27**, 1713 – 1716 (2015).

[89] Li, S., Li, M.-J. & Vodhanel, R. S. All-optical Brillouin dynamic grating generation in few-mode optical fiber. *Optics Letters* **37**, 4660–4662 (2012).

[90] Song, K. Y. & Kim, Y. H. Characterization of stimulated Brillouin scattering in a few-mode fiber. *Optics Letters* **38**, 4841–4844 (2013).

[91] Yokota, M. *et al.* Distributional measurement of effective refractive index differences of multimode fibers by Brillouin spectrum decomposition. In *Proc. SPIE 10323, 25th International Conference on Optical Fiber Sensors Conference*, 1032382 (2017).

[92] Lu, C., Dong, X. & Su, J. Detection of Refractive Index Change From the Critical Wavelength of an Etched Few Mode Fiber. *Journal of Lightwave Technology* **35**, 2593–2597 (2017).

[93] Zhou, J., He, B. & Gu, X. Transmission Spectrum Characteristics for a Single-Mode-Multimode-Single-Mode Fiber Filter. *IEEE Photonics Technology Letters* **26**, 2185 – 2188 (2014).

[94] Lu, C., Su, J., Dong, X., Sun, T. & Grattan, K. T. V. Simultaneous Measurement of Strain and Temperature With a Few-Mode Fiber-Based Sensor. *Journal of Lightwave Technology* **36**, 2796 – 2802 (2018).

[95] Gong, Y., Zhao, T., Rao, Y. & Wu, Y. All-Fiber Curvature Sensor Based on Multimode Interference. *IEEE Photonics Technology Letters* **23**, 679 – 681 (2011).

[96] Su, J., Dong, X. & Lu, C. Characteristics of Few Mode Fiber Under Bending. *IEEE Journal of Selected Topics in Quantum Electronics* **22** (2016).

[97] Garcia, F. C. & Kashyap, R. High-Sensitivity Non-Birefringent Mach-Zehnder Interferometer for Sensing UV Induced Refractive Index Change Using an Unique Short Bi-Moded Optical Fibre. In *Bragg Gratings, Photosensitivity, and Poling in Glass Waveguides (1999), paper AC5* (Optical Society of America, 1999).

[98] Jin, W., Michie, W. C., Thursby, G., Konstantaki, M. & Culshaw, B. Geometric representation of errors in measurements of strain and temperature. *Optical Engineering* **36**, 2272–2278 (1997).

[99] Xu, Y. *et al.* Discrimination of temperature and axial strain using dispersion effects of high-order-mode fibers. In *SENSORS, 2013 IEEE*, 1–4 (Baltimore, MD, 2013).

[100] Huang, T., Fu, S., Liu, S., Tang, M. & Liu, D. Discrimination between temperature and strain using fiber Bragg grating inscribed in few-mode silica-germanate fiber. In *2014 Opto-Electronics and Communication Conference and Australian Conference on Optical Fibre Technology OECC/ACOFT*, 1058–1060 (Melbourne, VIC, 2014).

[101] Patrick, H. J., Williams, G. M., Kersey, A. D., Pedrazzani, J. R. & Vengsarkar, A. M. Hybrid fiber Bragg grating/long period fiber grating sensor for strain/temperature discrimination. *IEEE Photonics Technology Letters* **8**, 1223 – 1225 (1996).

[102] Zhou, D.-P., Wei, L., Liu, W.-K., Liu, Y. & Lit, J. W. Y. Simultaneous measurement for strain and temperature using fiber Bragg gratings and multimode fibers. *Applied Optics* **47**, 1668–1672 (2008).

[103] Wang, L. *et al.* Simultaneous strain and temperature measurement by cascading few-mode fiber and single-mode fiber long-period fiber gratings. *Applied Optics* **53**, 7045–7049 (2014).

[104] Tripathi, S. M. *et al.* Strain and Temperature Sensing Characteristics of Single-Mode–Multimode–Single-Mode Structures. *Journal of Lightwave Technology* **27**, 2348–2356 (2009).

[105] Xuewen Shu, Lin Zhang & Bennion, I. Sensitivity characteristics of long-period fiber gratings. *Journal of Lightwave Technology* **20**, 255 – 266 (2002).

[106] Hahn, T. A. & Kirby, R. K. Thermal Expansion of Fused Silica from 80 to 1000 K - Standard Reference Material 739. *AIP Conference Proceedings* **3**, 13 (1972).

[107] Leviton, D. B. & Frey, B. J. Temperature-dependent absolute refractive index measurements of synthetic fused silica. In *Proc. SPIE 6273, Optomechanical Technologies for Astronomy*, 62732K (2006).

[108] Tissot, Y. Design and realization of fiber integrated grating taps for performance monitoring applications. *EPFL Thesis* **3882** (2007).

[109] Basu, S. & Limberger, H. G. Temperature dependence of grating resonances and two-mode interference in few-mode fiber. In *Advanced Photonics 2018 (BGPP, IPR, NP, NOMA, Sensors, Networks, SPPCom, SOF) (2018), paper BTh3A.3* (Optical Society of America, 2018).

[110] Morey, W. W., Meltz, G. & Glenn, W. H. Fiber Optic Bragg Grating Sensors. In *Proc. SPIE 1169, Fiber Optic and Laser Sensors VII* (1990).

[111] Malo, B. *et al.* Ultraviolet light photosensitivity in Ge-doped silica fibers: wavelength dependence of the light-induced index change. *Optics Letters* **15**, 953–955 (1990).

[112] Su, J., Dong, X. & Lu, C. Property of Bent Few-Mode Fiber and Its Application in Displacement Sensor. *IEEE Photonics Technology Letters* **28**, 1387 – 1390 (2016).

[113] Butter, C. D. & Hocker, G. B. Fiber optics strain gauge. *Applied Optics* **17**, 2867–2869 (1978).

[114] Hocker, G. B. Fiber-optic sensing of pressure and temperature. *Applied Optics* **18**, 1445–1448 (1979).

[115] Pissadakis, S. & Konstantaki, M. Photosensitivity of germanosilicate fibers using 213nm, picosecond Nd:YAG radiation. *Optics Express* **13**, 2605–2610 (2005).

[116] Schenker, R. E. & Oldham, W. G. Ultraviolet-induced densification in fused silica. *Journal of Applied Physics* **82**, 1065–1071 (1997).

[117] Lee, B. Review of the present status of optical fiber sensors. *Optical Fiber Technology* **9**, 57–79 (2003).

[118] Cavaleiro, P. M., Araujo, F. M., Ferreira, L. A., Santos, J. L. & Farahi, F. Simultaneous measurement of strain and temperature using Bragg gratings written in germanosilicate and boron-codoped germanosilicate fibers. *IEEE Photonics Technology Letters* **11**, 1635 – 1637 (1999).

[119] James, S. W., Dockney, M. L. & Tatam, R. P. Simultaneous independent temperature and strain measurement using in-fibre Bragg grating sensors. *Electronics Letters* **32**, 194 – 196 (1996).

[120] Song, M., Lee, S. B., Choi, S. S. & Lee, B. Simultaneous Measurement of Temperature and Strain Using Two Fiber Bragg Gratings Embedded in a Glass Tube. *Optical Fiber Technology* **3**, 194–196 (1997).

[121] Frazao, O. *et al.* Sampled fibre Bragg grating sensors for simultaneous strain and temperature measurement. *Electronics Letters* **38**, 693 – 695 (2002).

[122] Cao, Z. *et al.* Compact Fiber Sensor With High Spatial Resolution for Simultaneous Strain and Temperature Measurement. *IEEE Sensors Journal* **13**, 1447 – 1451 (2013).

[123] Zhang, X., Peng, W., Shao, L.-Y., Pan, W. & Yan, L. Strain and temperature discrimination by using temperature-independent FPI and FBG. *Sensors and Actuators A: Physical* **272**, 134–138 (2018).

[124] Jin, W., Michie, W. C., Thursby, G., Konstantaki, M. & Culshaw, B. Simultaneous measurement of strain and temperature: error analysis. *Optical Engineering* **36**, 598 – 609 (1997).

[125] Fibich, G. & Gaeta, A. L. Critical power for self-focusing in bulk media and in hollow waveguides. *Optics Letters* **25**, 335–337 (2000).

[126] Garcia, H., Johnson, A. M., Oguama, F. A. & Trivedi, S. New approach to the measurement of the nonlinear refractive index of short ($<$ 25 m) lengths of silica and erbium-doped fibers. *Optics Letters* **28**, 1796–1798 (2003).

[127] Okamoto, K. Chapter 4 - Coupled mode theory. In *Fundamentals of Optical Waveguides (Second Edition)*, 159–207 (Academic Press, Burlington, 2006).

[128] Giles, I. *et al.* Fiber LPG Mode Converters and Mode Selection Technique for Multimode SDM. *IEEE Photonics Technology Letters* **24**, 1922 – 1925 (2012).

[129] Wang, T. *et al.* Generation of Femtosecond Optical Vortex Beams in All-Fiber Mode-Locked Fiber Laser Using Mode Selective Coupler. *Journal of Lightwave Technology* **35**, 2161–2166 (2017).

[130] Wang, F. *et al.* Method of Generating Femtosecond Cylindrical Vector Beams Using Broadband Mode Converter. *IEEE Photonics Technology Letters* **29**, 747 – 750 (2017).

[131] Thornburg, W. Q., Corrado, B. J. & Zhu, X. D. Selective launching of higher-order modes into an optical fiber with an optical phase shifter. *Optics Letters* **19**, 454–456 (1994).

[132] Igarashi, K., Souma, D., Tsuritani, T. & Morita, I. Performance evaluation of selective mode conversion based on phase plates for a 10-mode fiber. *Optics Express* **22**, 20881–20893 (2014).

[133] Lai, K., Leon-Saval, S. G., Witkowska, A., Wadsworth, W. J. & Birks, T. A. Wavelength-independent all-fiber mode converters. *Optics Letters* **32**, 328–330 (2007).

[134] Velázquez-Benítez, A. M. *et al.* Six Spatial Modes Photonic Lanterns. In *Optical Fiber Communication Conference (2015), paper W3B.3* (Optical Society of America, 2015).

[135] Tsekrekos, C. P. & Syvridis, D. All-Fiber Broadband LP_{02} Mode Converter for Future Wavelength and Mode Division Multiplexing Systems. *IEEE Photonics Technology Letters* **24**, 1638 – 1641 (2012).

[136] Song, K. Y., Hwang, I. K., Yun, S. H. & Kim, B. Y. High performance fused-type mode-selective coupler using elliptical core two-mode fiber at 1550 nm. *IEEE Photonics Technology Letters* **14**, 501 – 503 (2002).

[137] Song, K. Y. & Kim, B. Y. Broad-band LP02 mode excitation using a fused-type mode-selective coupler. *IEEE Photonics Technology Letters* **15**, 1734 – 1736 (2003).

[138] Riesen, N. & Love, J. D. Ultra-Broadband Tapered Mode-Selective Couplers for Few-Mode Optical Fiber Networks. *IEEE Photonics Technology Letters* **25**, 2501 – 2504 (2013).

[139] Gross, S., Riesen, N., Love, J. D. & Withford, M. J. Three-dimensional ultra-broadband integrated tapered mode multiplexers. *Laser & Photonics Reviews* **8**, L81–L85 (2014).

[140] Jung, Y., Alam, S. U. & Richardson, D. J. Compact higher-order mode converter based on all-fiber phase plate segment. In *41th European Conference on Optical Communication (ECOC 2015), paper Mo.4.1.4* (2015).

[141] Lemaire, P., Atkins, R., Mizrahi, V. & Reed, W. High pressure H_2 loading as a technique for achieving ultrahigh UV photosensitivity and thermal sensitivity in GeO_2 doped optical fibres. *Electronics Letters* **29**, 1191 – 1193 (1993).

[142] White, A. E. & Grubb, S. G. Chapter 7 - Optical Fiber Components and Devices. In *Optical Fiber Telecommunications IIIB (Third Edition), Ivan P. Kaminow, Thomas L. Koch eds.*, 267–318 (Academic Press, Boston, 1997).

[143] Violakis, G., Aggarwal, N. & Limberger, H. G. Fabrication of mode field converter in H2-loaded SMF-28e using CW-Ar+ laser. In *Optical Fiber Communication Conference/National Fiber Optic Engineers Conference 2011, paper OWS4* (Optical Society of America, 2011).

[144] Wang, W., Wu, J., Chen, K., Jin, W. & Chiang, K. S. Ultra-broadband mode converters based on length-apodized long-period waveguide gratings. *Optics Express* **25**, 14341–14350 (2017).

[145] Zhao, Y., Liu, Y., Jiang, C., Mou, C. & Wang, T. Ultra-broadband mode converter based on an apodized long-period grating in two-mode fiber. In *CLEO Pacific Rim Conference 2018, paper Th1E.3* (Optical Society of America, 2018).

Soham Basu

PhD researcher at EPFL, Lausanne
Email: sohambasu6817@gmail.com
Linkedin Google scholar

Working style

Drive: Energized by continuous learning and solving complex problems.
Goals: In the long term, mastering ubiquitous fundamental techniques to be able to address a large variety of problems. In short term, work on challenging complex projects.
Best environment: Clear goals with the freedom in approaching the problems.
Communication style: Patient, clear and elaborate, approachable and freely approaching.
Strengths: Drive and determination for finding underlying patterns, resource awareness, comfortable in getting to depth of theoretical work, simulation as well as precision experiments.
Weaknesses: Affinity for choosing very hard research problems.

Career and education history

Oct 2019 – Present	**Intern on Isogeometric analysis, MNS, EPFL**
Feb 2015 – April 2019	**Doctoral researcher in fiber optics, HL-group, EPFL**
Jun 2012 – Jul 2013	**Masters in Applied Physics, Technical University Delft**
Oct 2011 – May 2012	**Masters in Applied Photonics, Imperial College London**
Jul 2007 – Jul 2011	**Bachelors in Engineering Physics, IIT Bombay, India**

Research contributions

Optics:
Solving the long-standing problem of fabricating low-loss, broadband, high extinction ratio mode converters in few-mode fibers at any desired wavelength. The challenge involved finding a new mathematical connection between two sub-fields of few-mode fiber technology and building a high-precision experimental setup for prototyping the deterministic solution.

Mathematics:

- Development of a stable Isogeometric finite element method for coupling overlapping meshes. For any conformation between two meshes, both the approximation error and the condition number of the stiffness matrix are bounded for linear problems.
- The first elementary correction to a subtle loophole in Carl Friedrich Gauss 's first (incomplete) proof of Fundamental Theorem of Algebra.
- First elementary real analysis based proof of the Fundamental Theorem of Algebra.

Scientific publications

2018	Temperature dependence of grating resonances and two-mode interference in few-mode fiber **Advanced Photonics (2018), Optical Society of America, paper BTh3A.3.** S. Basu, H. G. Limberger
2017	Temperature and Strain Sensitivity of Two-Mode Interference and Waveguide Dispersion **European Conference on Optical Communication (ECOC), 2017, pp. 1-3** S. Basu, H. G. Limberger.
2017	On Gauss's First Proof of the Fundamental Theorem of Algebra **American Mathematical Monthly 124, No. 8** S. Basu, D. J. Velleman

Contributed Talks in conferences

2018	Temperature dependence of grating resonances and two-mode interference in few-mode fiber **Bragg Gratings, Photosensitivity and Poling in Glass Waveguides and Materials (BGPP), Zurich**
2017	Temperature and Strain Sensitivity of Two-Mode Interference and Waveguide Dispersion **European Conference on Optical Communication (ECOC), Gothenburg**

Academic achievements

2018	**BGPP student award**, Waiver of conference fees
2011–2013	**Erasmus Mundus Scholarship in Optics and Photonics, OpSciTech** One of the 8 scholarship recipients worldwide For dual masters degree in Imperial College London and TU Delft

Organizational experience

2017–2019	Student representative of the Doctoral School of Photonics, EPFL I was in the committees of my department and the EPFL doctoral school. I also counselled fellow PhDs and ushered them to the officials, in case of research issues
2018	Invigilator of Intersectoral Excellence Committee meeting, EPFL I verified that the allotment of EPFLinnovators PhD scholarships was unbiased, fair and justified, by assessing the official reports and attending the final decision meeting.
2018	Co-organizer of COST Winterschool 2018, EPFL I verified the content of student contributions, and organizing the poster session
2011–2012	Student representative of the Department of Optics, Imperial College London

Teaching experience

2018	Supervision of masters sememster project, EPFL Supervising a masters student in experiments, data analysis and report writing.
2016-2018	Supervision in Optics laboratories II, EPFL Design and implementation of experiment on fiber optic coupling.
2016-2018	Teaching assistant for course on Optical Fibers and Fiber Devices, EPFL Supervision of simulations in Matlab and hands-on experiments.

Software Skills

Scientific computing:	Finite element method, Matlab, Comsol, Zeemax
Graphics and 3D design:	Adobe Illustrator, Solidworks
Writing and presentation:	Latex, MS Office

Language skills

English	Language of education from childhood. Studied for a year in London. TOEFL 2010 score 116/120: Reading: 30, Listening: 30, Speaking: 27, Writing: 29 GRE 2010 score 1430/1600: Verbal reasoning: 630, Analytical reasoning: 800
Hindi:	Fluency gained during undergraduate education in Mumbai
Bengali:	Mother tongue
French:	A2 level

Personal interests and Activities

Mathematics:	Mathematical discussions with varied colleagues in photonics about their projects and with mathematician colleagues
Music:	Learning Indian classical music from 2016, on vocal and Indian flute. Organized weekly informal sessions in EPFL for learning from expert singers
Sailing:	One year training of katamaran with EPFL colleagues in 2017. Laser (dinghy) training in 2018
Skiing:	Organized regular ski trips with colleagues from different labs in EPFL, and during the COST 2018 winter school

Personal Data

Address:	Chavannes-près-Renens, Switzerland
Born:	25 December 1988, in Alipuraduar, India
Family status:	Married